# 3D Spheroid Models For *in vitro* Evaluation of Nanoparticles for Cancer Therapy

Aleksandra Tchoryk

BSc Pharm (HONS)

Thesis submitted to the University of Nottingham for the degree of Doctor of Philosophy

September 2017

# Abstract:

Many different nanoparticle delivery systems have been reported as potential cancer therapeutics, however, the tumour penetration and uptake characteristics have been determined for very few systems. Animal models are effective for assessing tumour localisation of nanosystems, but difficult to use for studying penetration beyond the vasculature. In this work, defined HCT 116 colorectal cancer spheroids were used to study the effect of nanoparticle size and surface modifications on their penetration and uptake. Incubation of spheroids with Hoechst 33342 resulted in a dye gradient which facilitated discrimination between the populations of cells in the core and at the periphery of spheroids by flow cytometry based on the degree of Hoechst staining. This model was used to compare doxorubicin and Doxil, a range of model polystyrene nanoparticles in different sizes (30 nm, 50 nm, 100 nm) and with different surface chemistry (50 nm unmodified, carboxylated, aminated) and polyethylene glycol modified NPs prepared from a promising new functionalized biodegradable polymer (poly(glycerol-adipate), PGA). Unmodified polystyrene nanoparticles (30 nm/50 nm) were able to penetrate to the core of HCT 116 spheroids more efficiently than larger polystyrene nanoparticles (100 nm). Penetration was also dependent on surface charge. PGA NPs of 100 nm showed similar penetration into spheroids as 50 nm polystyrene nanoparticles, and PEG surface modification significantly improved penetration into the spheroid core. The new spheroid model with Hoechst staining is shown to be a useful model for assessing NPs penetration

and demonstrates the importance of controlling physical properties when designing nanomedicine.

# List of publications

## Papers

1. **Tchoryk, A**., Taresco, V., Argent, R., Ashford, M., Gellert, P., Stolnik, S., Grabowska, A., Garnett, M. (2017) Penetration and uptake of Nanoparticles in 3D tumour spheroids. (In the draft for submission to ACS Nano July 2018).

2. Conte, C., Mastrotto, F., Taresco, V., **Tchoryk, A.,** Quaglia, F., Stolnik, S., Alexander, C. (2018) Enhanced uptake in 2D- and 3D- lung cancer cell models of redox responsive PEGylated nanoparticles with sensitivity to reducing extra- and intracellular environments. Journal of Controlled Release, Volume 277, Pages 126-141.

3. Foralosso, R., Moir, L., Mastrotto, F., Sasso, L., **Tchoryk, A**., Abouselo, A., Grabowska, A., Ashford, M.B., Aylott, J., Gellert, P.R., Spain, S.G., Alexander, C. (2017) Control of aggregation temperatures in mixed and blended cytocompatible thermoresponsive block co-polymer nanoparticles. Soft Matter. ISSN 1744-683X (In Press).

## Oral Presentations

1. AstraZeneca Pharmaceutical Development PhD Day, AstraZeneca, Macclesfield, UK, 2017
2. School of Pharmacy, Final Year School Seminar, University of Nottingham, Nottingham, UK, 2017
3. CDT Colloquia: University of Nottingham, January 2017/ UCL, London, May 2016/ UCL, London, May 2015

## Poster presentations

1. The 44th Annual Meeting & Exposition of the Controlled Release Society, Boston, U.S.A., 2017;
2. AstraZeneca Pharmaceutical Development PhD Day, AstraZeneca, Macclesfield, UK, 2017;
3. Tumour Microenvironment - Basic Science to Novel Therapies, BACR conference, UK, 2017;
4. Making it Personal: Cancer Precision Medicine, Amsterdam, Netherlands, 2017
5. Midlands Innovation Flow Cytometry Meeting, University of Nottingham, Nottingham, UK, 2017;
6. Goodbye flat biology: Models, mechanisms and microenvironment, EACR conference, Berlin, Germany, 2016;
7. Postgraduate poster presentation, University of Nottingham, Nottingham, UK, 2016
8. UKICRS conference, University of Nottingham, Nottingham, UK, 2015;
9. AstraZeneca Pharmaceutical Development PhD Day, AstraZeneca, Macclesfield, UK, 2015;
10. Bionanotechnology and Nanomedicine Event, Nottingham, UK , 2015;

October 2015

## Acknowledgments

This work could not have been completed without the invaluable support of following people, whom I would like to thank:

Deepest thanks and gratitude to my supervisors Dr Martin Garnett, Dr Anna Grabowska, Dr Snow Stolnik (School of Pharmacy, School of Medicine, University of Nottingham) for guidance, inspiration and help throughout my PhD.

Thanks to my industrial supervisors Dr Marianne Ashford and Dr Paul Gellert (AstraZeneca, Macclesfield) for ideas, feedback and encouragement along the way.

Richard Argent (School of Pharmacy, Nottingham) for teaching me the technique of tissue culture and support during the research.

Pam Collier (Cancer Biology Unit, QMC, Nottingham) for training, support and for always being there to listen and give advice.

Phil Clarks for providing training in immunohistochemistry for sharing technical expertise and great chats.

David Onion and Nicola Croxall (Flow Cytometry Unit) for training in Flow Cytometry, expertise and support whenever it was required.

Delyan Ivanov for training in 3D cell culture and for sharing an enthusiasm for research and expertise throughout my PhD.

Vincenzo Taresco and Sadie Swainson for PGA series polymers for this work.

The team at Advanced Microscopy Unit for their technical assistance: Ian Ward, Denise Mclean, Seema Rajani.

Grainger-Boultby and Paul Cooling for technical support (Boots Building)

Beverly Bramley, Carol Turrill, Julia Crouch and Amy Nairn, for organizing numerous of meetings, conferences and ordering stuff.

Claudia Matz (CDT in Targeted and Advanced Therapeutics, Centre Manager) apart from the organizational support, for genuine care and friendly advice.

All my fellow PhD student with whom I shared the office and lab space (Teresa, Henry, Aziz, James, Aisha, Abdulah, Talib, Santi, Amar for great chats and laughs during long days and nights in the lab.

I wish to extend my thanks and appreciation to my internal assessor for expert advice and opinion on the project.

Finally thanks to CDT in Targeted Therapeutics and formulation science, AstraZeneca and EPSRC (EP/I01375X/1) for funding this research.

# Table of Contents

# Table of Figures

# List of Tables

# Abbreviations

| | |
|---|---|
| EPR | Enhanced Permeability and Retention Effect |
| 5-FU | 5-Fluorouracil |
| DOX | Doxorubicin |
| ECM | Extracellular Matrix |
| EGF | Epidermal Growth Factor |
| FACS | Fluorescence-Activated Cell Sorting |
| FBS | Foetal Bovine Serum |
| FDA | Food And Drug Administration |
| FGFs | Fibroblast Growth Factors |
| GAGs | Glycosaminoglycans |
| H&E | Haematoxylin and Eosin |
| HA | Hyaluronic acid |
| HAS | Hyaluronan Synthases |
| HSPG | Heparan Sulfate Proteoglycans |
| HTS | High Throughput |
| IFP | Interstitial Fluid Pressure |
| LSCM | Laser Scanning Confocal Microscope |
| MFI | Mean Fluorescence Intensity |
| MPS | Mononuclear Phagocytic System |
| MTS | Medium Throughput |
| NPs | Nanoparticles |
| O.C.T | Optimal Cutting Temperature Compound |
| PBS | Phosphate-Buffered Saline |
| PDI | Polydispersity Index |
| PDAC | Pancreatic Ductal Adenocarcinoma |
| PEG | Hydrophilic Polyethylene Glycol |
| PFA | Paraformaldehyde |
| PGA | Poly (Glycerol-Adipate) |
| PI | Propidium Iodide |
| PIMO | Pimonidazole Hypochloride |
| PLA | Polylactic Acid |
| PLGA | Poly(Lactic-Co-Glycolic Acid) |
| RBITC | Rhodamine B Isothiocyanate |
| RES | Reticuloendothelial System |
| Tg | Glass Temperature Transition |
| TPZ | Tirapazamine |
| ULA | Ultra Low Attachment |
| VEGF | Vascular Endothelial Growth Factor |

# Chapter 1 : Introduction

## 1.1 Cancer Therapy

Chemotherapy and radiotherapy are the most widely used nonsurgical treatments. Radiotherapy can be controlled spatially, however, the use of chemotherapy is compromised due to cytotoxic effects on normal cells as they have limited specificity to cancer cells. Most of the older anti-cancer treatments rely on the higher proliferation rate of cancer cells which make them more susceptible compared to normal cells. [1] However, the cytotoxic drugs also kill healthy rapidly dividing cells found in bone marrow, hair follicles or epithelial cells of GI tract leading to unpleasant and life-threatening side effects.[2] The toxic effect towards the healthy tissue thus limits the dose that can be given to a patient. Further, they often have poor solubility, and short plasma half-life and their delivery to solid tumours is problematic which leads to low anticancer efficacy.[3]

### 1.1.1 Concept of nanomedicine for cancer treatment

Much research has been undertaken in order to improve the selectivity of anticancer agents towards tumour cells to prevent side effects and exert a

higher cytotoxic effect. Outstanding progress has been made in the development of cancer nanotechnology.

Nanodrug delivery systems are formulations within a size range between (10–1000nm).[4] Typically they contain two components, a carrier, and a pharmaceutically active ingredient.[5,6] The carrier can be produced from various materials giving the systems very different physicochemical properties. The carriers are usually selected for the ability to incorporate a drug or other useful properties. Nanosystems offer great advantages over a conventional cancer treatment as they can provide a higher drug loading, longer circulation time and more targeted drug delivery into a tumour.[7,8] Unlike the healthy tissue, tumours have dilated and poorly differentiated blood vessels with leaky physiology and larger fenestrations. These abnormal changes lead to higher vascular permeability and decreased rate of clearance than in normal vessels caused by the lack of a functional lymphatic system in a tumour. Formulation scientists take advantage of this phenomenon, called the enhanced permeability and retention (EPR) effect to deliver nanoformulation selectively to the tumour site. Macromolecular formulation of size over 10 nm can enter a tumour via abnormal large pores in the leaky tumour vessels, however they are too large to extravasate a normal vessel. Furthermore, due to the absence of functional lymphatics, the nanoformulations can stay in a tumour for a long time. The EPR effect thus allows for more targeted delivery of anticancer nanoparticles into a tumour, and it reduces toxicity to healthy tissue.[9, 7]

Furthermore, nanocarriers can target a solid tumour actively by having a specific targeting ligand incorporated in their system. [9–12]

Other advantages of nanodrug delivery systems include their ability to increase the solubility of poorly soluble drugs in plasma, increase drug-circulation times, and provide controlled drug-release. Because of these characteristics, nanodrug delivery systems are expected to deliver a greater dose to a tumour which is typically limited by toxic side effects to normal tissues in the case of conventional drugs. [13, 14]

### 1.1.2 Properties of Nanoparticles (NPs)

Ideally, the nanosystems should prolong the *in vivo* circulation time of formulated drug, reduce the undesirable adverse effects caused by an anticancer drug given alone as well as improve therapeutic response. In order for those systems to provide such an effect, their physicochemical features need to be considered.

The size of nanosystems is one of the most important features which can be adjusted to control drug loading as well as drug release. A successful nanodelivery system should have a high drug-loading capacity.[15–17] Larger particles allow for more drug to be encapsulated than the smaller ones. However, smaller particles were shown to overcome biological barriers more easily and be taken up more readily by the cells than large nanoparticles.[16–19]

In order to take advantage of the EPR effect, the nanosystems have to be ideally within the size range below 150 nm as studies showed larger nanoparticles could not effectively pass through the gaps in leaky blood

vessels.[20] The size of the nanoparticle can also influence other *in vivo* behaviours such as stability, distribution, and cytotoxicity. Studies showed that nanoparticles with a diameter less than 50 nm or larger than 150 nm are more likely to be captured by the phagocytic cells and the reticuloendothelial system (RES) *in vivo*. [21–23,24,]

Other important properties of nanoparticles are surface characteristics such as hydrophobicity and charge. The degree of hydrophilicity/ hydrophobicity of the nanosystems is adjusted based on the properties of the drug.[17]

The surface charge of nanoparticles as a measure by zeta potential can influence stability in suspension. The positive surface charge of nanoparticles is thought to enhance targeting of tumour vessels and thereby exhibit higher permeability when compared with their anionic or neutral counterparts.[25,26] However, it can also have deleterious effects on biodistribution. Coating of nanoparticle surface with hydrophilic polyethylene glycol (PEG) provides steric stabilisation to the system and helps to prevent opsonization by complement and other serum components. [18,27,28]

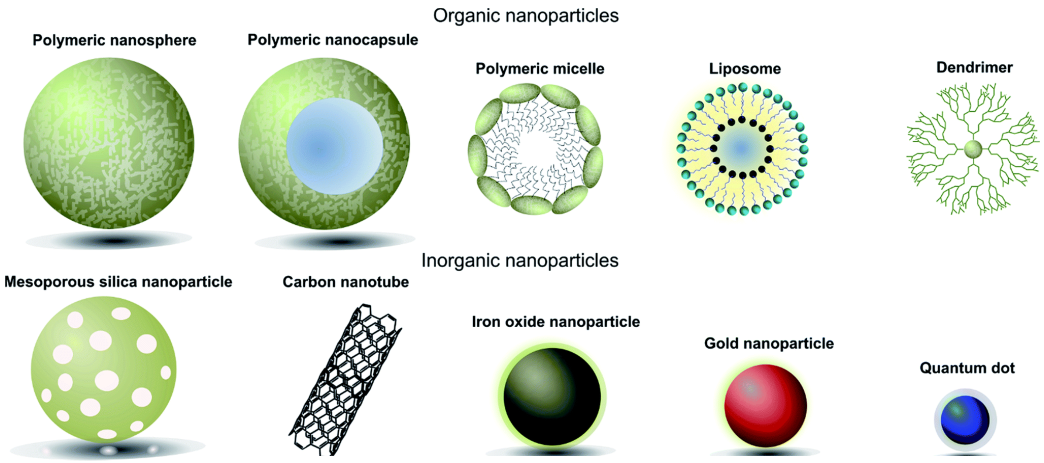


*Figure 1 Schematic representation of different types of nanoparticles proposed for use in biomedical applications.*[29]

Various nanodrug delivery systems have been generated such as nanoparticles, micelles, liposomes, dendrimers and more (Figure 1). These carriers vary widely in their physicochemical properties and are capable of incorporating various polar and nonpolar drugs, either within the core or by forming a drug carrier conjugate system. [14,18,30,31]

Natural and synthetic polymeric nanoparticles received considerable interest due to their high stability and ease of surface modification. These systems were showed to improve bioavailability, sustain release of drugs and solubilize drugs for systemic delivery. They often contain the active drug in a core separated from the environment by a polymeric shell. Their characteristics can be chosen to enhance drug loading and delivery. They are often able to provide constant release rate which is an attractive feature for drug delivery applications.[9] PLGA and PLA polymer nanoparticles have been shown effective for sustained drug delivery and intracellular targeting.[16,17,32,33]

Another example are PGA based nanoparticles which gained interest due to advantages such as high drug loading and sustained release of the encapsulated therapeutic agent over a long period of time. Moreover, they have easily tuneable hydrophobic/hydrophilic properties which make this polymer very attractive for drug delivery application. [34]

Liposomes have also shown great promise for delivering therapeutic agents. Doxil® is one of an example of a PEGylated liposomal formulation of doxorubicin (Dox) which has been FDA approved. An increasing number of promising systems appear in the clinical trials. Liposomes are composed of amphiphilic molecules that self-assemble into a spherical structure with the

polar and the nonpolar environment thus allowing encapsulating both polar and nonpolar drugs. Liposomes can be unilamellar, containing one lipid bilayer or multilamellar containing multiple lipid bilayers. Their structure and composition resemble cell membranes. Such nanosystems can provide prolonged release kinetics and long persistence at the target site.[35,36]

Other systems such as macromolecule–drug conjugates have also been explored as drug carriers.[37,38] Poly-(L)-Glutamic Acid-Paclitaxel system showed to enhance the solubility of hydrophobic paclitaxel and provided enhanced efficacy, reduced toxicity and improved distribution to a tumour. [37,38]

Biodegradable polymeric micelles with a size of 10–200 nm have also shown therapeutic potential. The copolymers consisting of two or more polymer chains with different hydrophobicity spontaneously assemble into a core-shell micellar structure in an aqueous environment. This micellar structure provides drug delivery nanocarriers with high loading capacity (5–25% weight) for poorly soluble drugs. [39–41]

Another class of nanosystems are Dendrimers. They are globular, highly branched, and synthetic polymers which provide unique characteristics.[42, 43] Their structure enables them to carry various drugs through covalent conjugation, electrostatic interactions, hydrophobic interaction, hydrogen bonding, or chemical linkage. Recently, researchers developed a poly-amidoamine-based G5 dendrimer with primary amines on their surface and a diameter of about 5 nm. The system contained methotrexate drug and folate targeting molecule and was found to be about 10 times more effective than

methotrexate alone in slowing tumour growth. [44] An anticancer drug Paclitaxel, also shown promise when attached to the exterior of the dendrimer. [9]

Various nanodrug delivery systems have been investigated as possible carriers of anticancer drugs. [3] These systems show great potential in overcoming many problems in delivering chemotherapeutic drugs to a tumour. [18]

Over 20 nanoparticle therapeutics have been approved by the FDA for clinical use.[38] Nanoparticle formulations for the treatment of solid tumours such as Doxil and Abraxane, however, were shown to demonstrate disappointing treatment benefits in many cases. [45, 46] Therefore, a better understanding of the biological barriers that prevent successful delivery of nanoparticles into tumours is needed in order to realize the full potential of nanodrug delivery systems.

## 1.2 Barriers to successful nanosystems delivery

In order for efficient delivery of nanoparticles to tumours, they must overcome several barriers. After injection into the bloodstream, they encounter heterogeneous blood supply, transport across the microvascular wall, transport through a tumour interstitial space and transport across the cell membrane.

During their journey in the blood, they are subjected to the process of nonspecific binding of proteins and other components found in blood such as albumin, fibrinogen etc. process known as protein corona. They can also

undergo degradation and agglomeration which can reduce their plasma half-life.[26]

### 1.2.1 Transport through the microvascular wall

To reach the tumour target cells nanosystems must first cross the capillary wall. These vessels in a tumour have abnormal physiology with large gaps which cause them to become leaky. This leakiness makes permeability of these vessels significantly higher in a tumour than in normal tissues. These gaps allow for extravasation of nanoparticles and other macromolecules into tumour tissue. However, permeability is dependent on the physicochemical properties of nanoparticles. It has been noticed that with the increase in the size of particles the vascular permeability decreases. It has been suggested that for successful extravasation through the vessels NPs should stay below 150 nm. [8, 9]

### 1.2.2 Interstitial Fluid Pressure (IFP)

Once the nanoparticles escape the vasculature, it encounters another hurdle to extravasation, interstitial hypertension. This is a result of the high permeability of tumour vessels and the lack of functional lymphatic vessels in a tumour which results in a build-up of hydrostatic pressure.[26] Due to the abnormal tumour vasculature, the blood supply within tumours is generally low, and in effect, the transport of macromolecules through the vessels and the interstitial

space is mainly by diffusion and not convection.[47–49] The pressure gradient may hinder fluid flow into a tumour from blood capillaries.[47] Further, there is a risk that interstitial fluid pressure inside a tumour will exceed the fluid pressure inside the vessels and result in the therapeutics being excluded from a tumour. The abnormal tumour vasculature together with the interstitial tumour matrix is thought to lead to a heterogeneous distribution of therapeutics in tumours. These therapeutics concentrate close to the vessels and cause only local effects.

### 1.2.3 Tumour physiology

The limited ability of drug molecules and nanosystems to accumulate in tumours is believed to be largely affected by the complex physiology of the tissue. Tumours are abnormal masses of tissue. Many of the most common tumours such as stomach, pancreas, liver, colon, lung or breast are carcinomas, tumours that originate from epithelial cells of skin or tissues. Carcinomas have complex pathophysiology. Tumours consist of epithelial cancer cells and supportive stroma. Stroma is mainly made of fibroblasts, endothelial cells, immune cells and the extracellular matrix (ECM) (Figure 2).

The majority of solid tumours develop hypoxic regions as well as necrosis in their structure. [50] As an effect of hypoxia, hypoxia-inducible factor (HIF1α) is up-regulated which then promote the production of growth factors such as

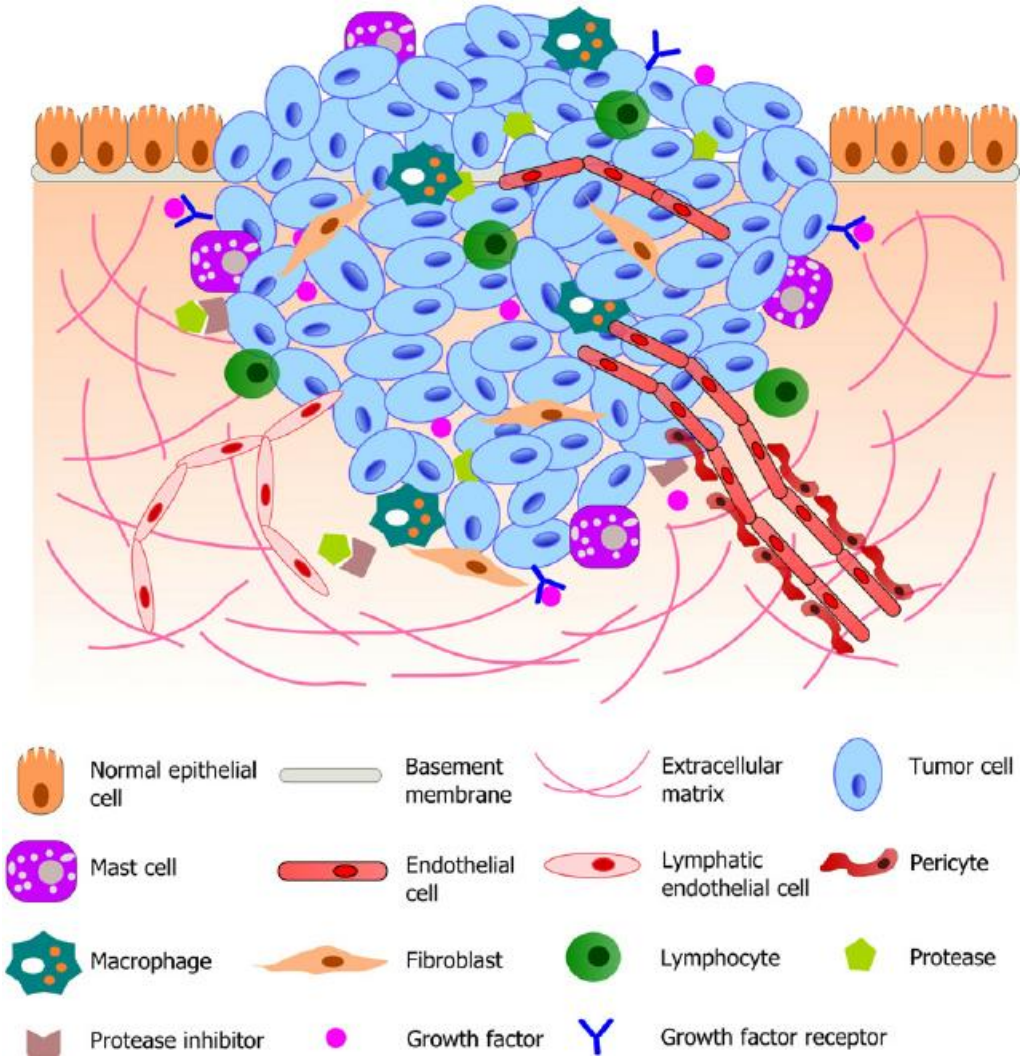


*Figure 2 Schematic of a typical tumour microenvironment. Cancer cells reside in a complex microenvironment containing various supporting cells, extracellular matrix (ECM) and a suite of signalling molecules. Taken from* [187]

vascular endothelial growth factor (VEGF) that leads to the formation of new vessels. [51]

In tumours, cells can be located 15 to 20 cell diameters from the nearest blood vessel in comparison to normal tissue. [52] As cancer grows, parts of the tumour mass located further to the blood vessels are exposed to a limited oxygen concentration leading to the formation of cell proliferation gradients with hypoxic, quiescent cells in the core of a tumour and dividing cells at the rim. [2] The lactic acid caused by anaerobic glycolysis in hypoxia causes the microenvironment to become acidic. [53–55] The acid conditions, found in many types of a tumour, together with a deficiency of nutrients contribute to cell death and necrosis within solid tumours. Many cells, however, are known to survive under these conditions and are thought to contribute to resistance to cytotoxic drugs and radiotherapy as well as induce metastatic behaviour. [2,46,50] Further, the formation of quiescent cells in the core limits the efficacy of drugs that target rapidly dividing cells. [50]

Further, tumour compromise of dense stroma which components are responsible for the production of ECM.[56] The complexity of tumour tissue, arrangements of cells may also affect the transport of particles. Further, it may affect large particles to a greater extent exposing them to wider intercellular paths. The viscous tortuosity due to cells and ECM fibres has also been suggested to increase the hindrance to nanoparticles. [49]

### 1.2.4 Tumour Extracellular matrix

In order for the treatment to be effective nano-therapies must first penetrate through the interstitial matrix before reaching all of the cancer cells in lethal concentration.

The tumour interstitial matrix is a meshwork composed mainly of collagen, glycosaminoglycans (GAGs) such as hyaluronan (HA), proteoglycans and glycoproteins that combined are believed to form a diffusion barrier for the therapies to penetrate. [57–61]

#### *1.2.4.1 Collagen*

Collagen is synthesized predominantly by fibroblasts, but some of the ECM collagen can also be produced by epithelial cells. Collagen provides considerable tensile strength to tissue. [26]

Depending upon the composition, the collagen molecules can be divided into at least 10 types; [26] Collagen type I is the most abundant, constituting nearly 90% of all the collagen in the human body. Collagen fibres carry a slightly positive charge at neutral pH. The spacing between collagen fibrils was measured to be between 20–40 nm in a compact tumour and 75–130 nm in looser tumour tissue. These narrow spaces are thought to restrict the penetration of larger particles. [25]

### *1.2.4.2 Glycosaminoglycans*

The GAGs also known as mucopolysaccharides are long unbranched polysaccharides containing a repeating disaccharide unit. GAGs are highly negatively charged molecules. Their primary location is in the ECM and on the surface of cells. They provide high viscosity to the solution in which they reside and provide structural integrity to cells and passageways between cells, allowing for cell migration. They were shown to significantly increase the viscosity of the interstitial fluid. [46, 62] They are also responsible for alignment and spacing of collagen fibrils. The majority of GAGs in the body are linked to core proteins, forming proteoglycans.[49] The GAGs extend perpendicularly from the core in a brush-like structure. Various studies have shown that the stabilized polysaccharide network enmeshed in the collagenous fibres offers considerable resistance to interstitial transport of macromolecules.[26]

The hyaluronic acid, chondroitin sulphate, heparin and heparan sulphate are some of the GAGs found in the ECM.

Heparin and heparan sulphates are composed of sulphated GlcNAc and glucuronic acid (GlcA) disaccharide units. They are components of cell surfaces and are associated with protein forming heparan sulphate proteoglycans (HSPG). HSPG binds many ligands such as fibroblast growth factors (FGFs), VEGF, and hepatocyte growth factor.

Chondroitin sulphate is the most abundant GAG polymerized into long chains and is found attached to a large family of proteoglycan core proteins referred to as lecticans.

Hyaluronans are synthesized by hyaluronan synthases (HAS) in the plasma membrane in virtually all cells in the human body. Unlike other GAGs, HA does not contain any sulphate, and it forms non-covalently bound complexes with proteoglycans in the ECM. HA have essential roles in development, tissue organization, cell proliferation, and signal transduction processes and its function is mostly dependent upon interaction with proteins present on the surface of the cell and/or secreted into the ECM. The large HA extrude into the ECM and can displace a large volume of water. The concentration of HA is elevated in many carcinomas, including bladder, prostate, breast, lung, colon and so forth. In tumour tissues, it promotes tumour growth, metastasis and angiogenesis. The hyaluronans can be remodelled or degraded by hyaluronidases; HYAL1 and HYAL2 after synthesis and its turnover can take as little as one day in some tissue. [49, 63]

The ECM is considered to be one of the causes of resistance to drug movement. [46] A few mechanisms have been proposed to take place between the ECM and the therapeutic agents such as steric interactions, which arise from the collisions with ECM fibres, electrostatic interactions due to binding to the tissue and ECM components, and consumption of drug molecules as they travel through the tissue and interact with cells.

There is, however, need to develop a better understanding of these mechanisms in order to aid the development of novel strategies capable of overcoming these issues.

### 1.2.5 Effect of ECM on NPs penetration

ECM is a highly complex structure made of various components which particles must overcome to deliver their cargo into cells and exert their action. The penetration of large complexes such as monoclonal antibodies, therapeutic proteins, or genes has been shown to be affected by the barrier of ECM. [56]

ECM is believed to control transport of macromolecules by size exclusion effect due to narrow spacing between ECM fibres. [64] The pore sizes in the ECM vary depending on the type and its location. For example, glomerular basement membrane has 3 nm pores while human cervical mucus is characterized by a 340 nm pore size. The interfibrillar spacing between collagen fibrils has been measured to be quite narrow (20–40 nm) within compact collagen bundles and was 75-130 nm within looser bundles. The ECM is thus believed to behave as a dispersive filter. [64] This is supported by several studies which showed that by degradation of the collagen matrix with bacterial collagenase treatment or relaxin in high collagen-content tumours causes a great increase in the diffusion of antibodies, such as IgG (hydrodynamic radius 4.5 nm) and herpes simplex virus (hydrodynamic radius 75 nm). [1, 56] Netti et al. (2000) found that the amount of collagen in tumours correlated inversely with the diffusion coefficient of macromolecules. [57] Pluen et al. (2001) provided further support for the role of collagen by measuring diffusion in tumours grown in subcutaneous tissue and the cranium. [49]

Limited transport of macromolecules has also been proposed due to steric hindrance posed by GAGs. [63,65] Thanks to properties such as highly flexible chain and very great molecular weight, hyaluronic acid was found to the form entangled meshwork even at a very low concentration which was shown to cause resistance for the diffusing particles. Diffusion of globular proteins in the hyaluronic gel and sulphated proteoglycans was shown to be dependent on their dimensions as well as ECM network component.[66] This observation was described by Laurent et al. in terms of a sieving mechanism. [63, 65] It was also proposed that unlike hyaluronic acid, collagen network alone has a relatively little effect on diffusion due to much thicker fibres (500-1000Å as compared with about 8 Å) which at the similar concentration of HA, form a much coarser meshwork through which both diffusion and flow can occur easily.[63,66]

Another mechanism by which ECM is thought to restrict diffusion of macromolecules is via electrostatic interactions. ECM is a strongly charged network compromised of slightly positive collagen fibres at neutral pH and highly negative charged GAGs. [46,63,67] These are believed to interact with charged nanoparticles and inhibit their transport due to electrostatic binding and formation of aggregates.[46]

This interaction has been observed in the study where a decrease in penetration of charged nanoparticles was caused by electrostatic binding to heparan sulphate. Further, several studies have investigated the effect of enzymatic digestion of highly negative GAGs and showed improved convection of macromolecules after digestion. [1,46]

There are contradicting reports in the literature showing which constituent of ECM is responsible for restricting the transport of macromolecules. It is not clear whether the collagen or GAGs play a greater role.

Some studies claim that poor diffusion is due to the presence of GAGs because of their high negative charge density and hydrophilic character while collagen provides structural function and support. [26,57] However, different studies state that only when proteoglycans are supported by stabilizing solid matrix such as collagen, they can restrict diffusion of macromolecules. [57,63,66] While other propose that both collagen and GAG/ proteoglycans matrix contributes to the limited diffusion of nanoparticles and macromolecules.[48,49,56,57,61,64] Therefore, the organisation and distribution of different components of the ECM matrix and not just their levels may also be important in limiting the diffusion through the interstitial space. The distribution of collagen and GAGs in a tumour can divide the tumour space into viscous regions, high in collagen and aqueous regions high in GAGs. The diffusivity of the particles will be very different in those two phases.[46] The functional state of the ECM also needs to be taken into consideration. The ECM is a highly dynamic structure which in a tumour undergoes a rapid remodelling process involving degradation, deposition or modification of ECM components.[68] This has potential to affect penetration of macromolecules differently with time. [1,47,63]

Only when the nanoparticles pass through all the above-mentioned barriers, they can reach their target cells. However, how readily they are taken up by those cells will also be dependent on their characteristics such as size, charge and surface properties.

## 1.3 Preclinical cancer models

The pharmaceutical drug discovery process is divided into preclinical and clinical phases. In the pre-clinical phase, small molecule drug compounds are screened in medium throughput (MTS) or in high throughput (HTS) manner for their structure, physical properties and efficacy in pre-clinical disease models before testing in animal models.[69] Typically the *in vitro* study employs 2D cell monolayers as models for anticancer drug testing. These models are over-simplified as they do not mimic tumour environment *in vivo.*

### 1.3.1 Monolayer

Monolayer culture has been typically used for evaluating chemotherapeutic drugs to test their therapeutic responses at the cellular level. However, due to the oversimplified structure of monolayer; this cell model has been found to inaccurately predict efficacy *in vivo*. This is because they do not mimic the microenvironment of solid tumours thereby ignoring the contribution of tumour environment to the drug resistance. These cells are exposed to a uniform concentration of a drug unlike in a tumour where drug concentration gradients are formed from blood vessels. The transport abilities of drugs and nanoparticles through the tissue cannot be studied via this model.[1]

### 1.3.2 Animal models

The current process for testing the effectiveness of nanosystems relies greatly on *in vivo* models. The standard *in vivo* model used in drug testing is the human tumour xenograft. The model involves inoculation of human cancer cells or small cancer fragments subcutaneously or orthotopically in immunocompromised mice. The injected cells are left to mature into a tumour for 1–8 weeks. The main advantage of this method is the capability to mimic the complex interaction of cancer tissue with surrounding stroma. However, the therapeutic effect found from xenografts in mice provides insufficient relevant information for translation into the clinic due to fundamental differences in immune function, microenvironment and cell biology between human and mouse.(Nyga et al. 2011) Studying nanosystems distribution, penetration and access to target tumour cells is difficult.[1] Furthermore, with an increasing number of nano-delivery systems being developed, it is impossible to test them all using *in vivo* studies which are unethical, complex and expensive. It has been reported that less than 10% of the potential anticancer agents progress successfully through clinical development.[71, 72] Therefore, there is a need for a representative *in vitro* model that will allow the testing of anticancer drugs and nanomedicine in the early stages of the development process.

*In vitro* models, which mimic more closely tumour microenvironment, may help to achieve that and provide a useful bridge between an oversimplified monolayer and animal models.[73] Furthermore, development of more biologically relevant *in vitro* tumour models may ultimately result in a better

translation to the clinic and a reduction in a number of the animal models required in drug discovery programmes.[74] In such *in vitro* model, it is important that characteristics of a tumour such as architectural organisation, cell-cell and cell-matrix interactions are recapitulated.[75] Further, they should be robust, quantitative and highly reproducible assays to be applicable for drug discovery in an industrial setting. [69]

### 1.3.3 3D cancer models

*In vitro* screening assays should be capable of eliminating poorly performing drug systems early in their development, this could allow for improved screening efficacy. It is therefore highly desirable to improve *in vitro* cell-assays for early drug-delivery system's development. While 2D monolayer culture lack relevant tumour features such as cell-cell and cell-ECM signalling, the 3D tumour models have been widely recognised as a more promising tool for drug delivery and efficacy testing. [72,76,77] They are 3D aggregates of cancer cells and are believed to more closely resemble the tumour microenvironment, and could potentially provide a compromise between the oversimplified 2D monolayer and the complex human tumours grown in xenogeneic hosts.[1,78–80]

Therapeutic effects of a drug and nanocarriers in tumours can be greatly affected by poor penetration and heterogeneous distribution due to natural barriers such as ECM.[83] Some studies found that certain ECM components such as collagen I are expressed at higher levels in 3D models than in 2D using breast cancer cell cultures. PDAC cells were found to express endogenous

ECM components such as collagen and fibronectin-1 when grown in 3D.[83] Others showed that culturing cells in the presence of ECM components, such as collagen I or fibronectin makes these cells more resistant to anticancer treatments.[78] Unlike 2D monolayers, the 3D models have the ability to establish these penetration barriers thereby allowing the study of penetration, distribution and binding properties of chemotherapeutic agents and nanodelivery systems in the early stages of their development process. [83,84]

Apart from the previously mentioned structural differences between 2D and 3D cell models, there are a number of biological variabilities that can influence the behaviour of cells and their signalling pathways thereby affecting the way they react to therapeutic agents.[85–90] Studies showed a definite difference in genetic and phenotypic behaviour of cells cultured in 3D, offering alternative signalling platforms that may not be available in a 2D culture which can affect their response to therapeutics.[91–93] Further, 3D cultures generally show different responses to chemo- and radiotherapy than their 2D counterparts.[14,83,94] Pickl and Ries reported differences in the levels of growth factors and overexpressed proteins in breast cancer cells between 2D and 3D cultures that resulted in a dramatically different effects of the anti-cancer drug trastuzumab on cell growth in monolayers as compared to cells in 3D.[91] A similar finding was observed in another study, where cells were treated with the same concentrations of 5-fluorouracil (5-FU) and tirapazamine (TPZ) there were differences in viability between cells cultured in 2D and 3D.[95] In the case of 5-FU, results indicated that 3D spheroids were more resistant to the treatment than cells grown in 2D. However, in the case of TPZ, the 2D cells

were more resistant to the effects of the drug due to the lack of hypoxic cells. The presence of hypoxic cells in 3D activated the drug to a higher degree allowing for greater drug response. The presence of increased levels of ECM may also alter the response to treatment on a cellular level, as it plays a significant role in controlling cell behaviour by regulating the levels of growth factors such as epidermal growth factor (EGF), FGF and other signalling molecules and receptors of the local environment. [89,96] Further, Meng et al. showed the difference in endocytic uptake of NPs in 2-D and 3-D models. [97] These and many more studies suggested that 3D spheroids are more representative of a native tumour than 2D and thus should be employed as standard models for testing anticancer drugs and nanomedicine for solid tumours to avoid overestimating or underestimating the effect of treatments prior to animal studies.[76]

The 3D cell tumour models range from simple homogenous cell models to models comprising multiple cell types. [81,82] Over the last decade, they have increased greatly in number due to advances in their culturing/ engineering techniques. Three main types of 3D culture models of cancer are tumour tissue explant, a tumour on a chip, and multicellular tumour spheroids (Table 1.)

*Table 1.* 3D cell culture models of tumour. Available from [103].

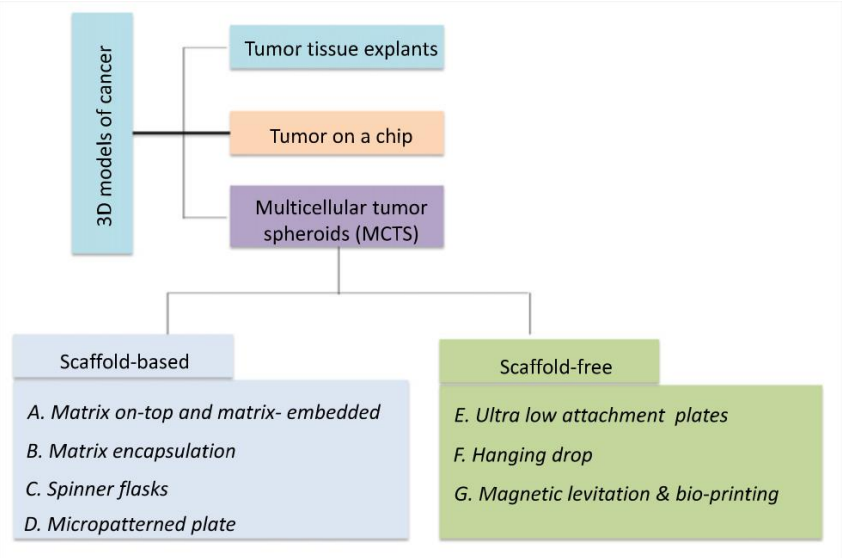


The tumour tissue explant involves culturing excised human tissue from a biopsy in tissue culture plates.[98] Growing this type of model often requires a collagen-coated surface which allows cells to adhere or embed within the gel matrix. The main advantage of this model is the ability to preserve the original tumour tissue architecture and microenvironment. However, the model lacks of reproducibility due to high heterogeneity of the biopsy tissue, provides difficulties with long-term culture and it is incompatible with common investigative techniques such as imaging and flow cytometry; this limits the application of such models. [99]

A tumour on a chip is a revolutionary micro-engineered biomimetic model that allows culturing many different cells on a microfluidic device thereby recreating the tumour microenvironment.[100,101]

The device is an array of microfluidic channels, which mimics vasculature, and microwells (250 μm–450 μm) in which tumour cells grow. The technique allows for custom microfabrication of the chip and real-time data recording. Further, it allows for the generation of complex 3D co-culture models compromised of many different cells such as endothelial cells, immune cells and circulating tumour cells thus provides new opportunities for genomic and drug screening research. [100–102] However, difficulties with tissue size control as well as issues with a collection of cells for post analysis are the limiting factors.

Multicellular tumour spheroids have a well-organised spherical symmetry of morphological and physiological features and can be generated from tumour cells alone or in combination with other cell types.[103] This is the most widely used 3D model system. Increasing evidence in the literature supports the importance of employing 3D cell spheroids for nanodrug-delivery testing.[104,105] A number of studies have shown that they have the ability to form a more realistic organisational milieu with 3D spatial arrangements, cell-cell and cell-matrix interactions, relevant pH, diffusion gradients and hypoxic core. [106,107] Including these characteristics of a tumour in a nanodrug-delivery screening assay is important as these features are thought to influence drug resistance.[50] Further, by employing 3D spheroids of human cancer cells, the possible impact of the exogenous environment on cell signalling observable in the case of xenografts can be eliminated. [83]

There are different methods for generating spheroids with or without a scaffold. In scaffold-based methods, the scaffolds support 3D organisation of

cancer as well as promote cell-cell and cell-matrix interactions. Commonly used scaffolds for growing 3D spheroids include ECM-based natural hydrogels, synthetic hydrogels, and engineered synthetic hydrogels. Other, scaffold-free methods mainly focus on promoting cell-cell contact by resisting cell–surface interactions. Methods include hanging droplets, liquid overlay and agitation-based approaches.[51,72,108]

The proposed advantages and disadvantages of different methods for generation of spheroids are summarised in Table 2.

In our study, we decided to work with 3D spheroids as a model of a tumour as they are easy to grow, reproducible and capable of mimicking the microenvironment *in vivo*. We employed the liquid overlay method which promotes the formation of spheroids by preventing cell attachment to the surface thus encouraging cell-cell interactions.[109,81] For the production of spheroids we used 96-well round bottom ultra-low attachment plates. The surface of these plates is pre-coated with a hydrophilic polymer which prevents cells attachment thereby influencing cells to interact with each other. Alternatively, the surface of the plates can be modified with other materials such as poly-hema or agarose 1.5% which also prevent cell attachment. The manual coating of the plates prior to cell seeding is a cheaper option; however, it is time-consuming and adds an extra step to the overall process.

*Table 2 Methods used for generation of 3D models and proposed advantages and disadvantages of these methods.( Adapted from [111,81, 72])*

| Method | Advantages | Disadvantages |
|---|---|---|
| Non-adherent surfaces/ Forced floating method/ Liquid overlay cultures | Relatively simple<br>No specialized equipment needed<br>Inexpensive<br>Compatible with High-throughput testing<br>Spheroids easily accessible | Not efficient<br>Tedious media exchange<br>Co-culture cellular composition difficult to define<br>Extra step required to coat the plates which is labour intensive<br>Expensive when using pre-coated plates |
| Hanging drops | Relatively Simple<br>Inexpensive if using a standard 96-well plate<br>Homogeneous spheroid size<br>No specialized equipment needed<br>Suitable for high-throughput testing | Tedious handling<br>More expensive if using specialised plates<br>Media exchange difficult<br>Long-term culture difficult due to instability<br>Low throughput<br>Not efficient<br>Time-consuming<br>Not stable<br>Not suitable for characterisation |
| Microfluidic devices and spheroids on a chip | Improved efficiency<br>Simplified handling procedures<br>Uniform spheroid size control<br>Uniform cellular composition<br>Suitable for high-throughput testing<br>The analysis may be integrated into the device | Specialised equipment required<br>Complicated set-up and device fabrication<br>Expensive<br>Material – drug compatibility issues<br>Long-term culture problematic<br>Devices not available for mass production<br>Spheroid retrieval for further analysis difficult<br>The issue with Compatibility for HTS testing |
| Scaffolds and Matrices | High-throughput production<br>Good extracellular support<br>Provide 3D support that mimics the situation *in vivo*<br>Easy to set up<br>Easy handling<br>Mass production of scaffolds possible<br>May be compatible with HTS instruments<br>Uniform spheroid size<br>The material may incorporate growth factors<br>Long-term culture possible | Samples retrieval for further analysis difficult<br>Expensive for large-scale production<br>Scaffold Biocompatibility and biodegradability issues |
| Agitation-based approaches (Spinner flasks) | Relatively cheap and Simple<br>Production of a large number of spheroids<br>Long-term culture possible<br>Spheroids easily accessible | Special equipment required<br>No control over spheroids size or composition<br>High shear force affect cells Spheroids<br>Architecture not as well preserved<br>Extra step required for HTS testing |

A gentle centrifugation step is often included in the process to enhance cell aggregation and to ensure equal cell numbers for the initiation and formation of spheroids in each well. Centrifugation is also believed to suppress cell apoptosis by encouraging paracrine signalling.[78,108] The round shape of the wells induces the spheroids to collect at the bottom and allows for easier handling during media exchange. Subsequently, after 12-24h in culture spheroids are formed. The method has been successfully employed in-house by Ivanov et al. who used it for the production of neurospheres. [110]

Despite the known advantages of using 3D models in cancer research, due to issues associated with production, maintenance and lack of standard procedures, monolayer cultures are still preferred in cell-based screening. [108]

In order to employ the 3D spheroids for routine drug testing their production should be cheap, easy and capable of generating reproducible models. Moreover, standardised protocols need to be designed and validated for the 3D platform and adapted for automated analysis and high-throughput formats. [71,111]

The schematic representing steps in the production process of spheroids using

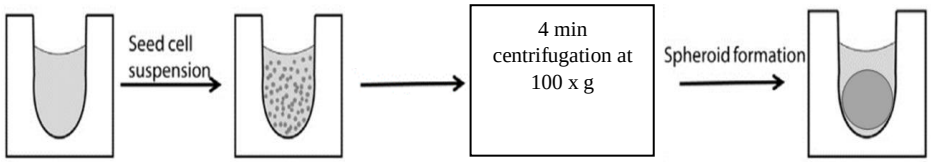


*Figure 3 Liquid overlay method using Ultra low attachment (ULA) 96-well round bottom plates. A cell suspension is seeded into the wells, the plate is centrifuged for 4 min at 100 x g and consequently spheroids are formed after 24h-72h in culture.*

liquid overlay method is shown in Figure 3.

To date, there are limited numbers of studies that employ 3D models for the evaluation of nanomedicine. [58, 112] By employing the 3D spheroid models in this study, we hope to develop a better understanding of the underlying mechanisms behind the chemoresistance and lead to the development of novel strategies capable of overcoming these issues.[112]

## 1.4 Objectives

There is great interest in using nanoparticles to deliver drugs to tumours. However, an increasing number of nanosystems are being developed which vary considerably in their physicochemical properties. There is increasing evidence indicating that the physiochemical properties of nanoparticles such as size, surface charge and surface chemistry play a crucial role in their ability to penetrate through the ECM. However, there are too few comparisons that facilitate understanding of the effect of these physicochemical properties on their penetration and uptake in representative tumour models. [60,113] Developing such understanding is crucial to aid the design of nanocarriers capable of sufficient accumulation in a tumour to optimise therapeutic performance.

It is difficult to characterize many important properties of NPs *in vivo*, and therefore attempts have been made to develop more realistic *in vitro* models. In our study, we aim to:

Identify and characterise 3D cell culture models and select an appropriate model or models for the study of penetration of NPs.

Develop methods to study the penetration abilities of nanocarriers *in vitro.*

Select well-characterised model drugs and NPs and evaluate their penetrability abilities in the 3D cell model.

Study penetration and uptake of interesting and promising nanoformulations in the 3D cell model.

Identify important key characteristics of nanoformulations affecting their diffusion through the cell model.

# Chapter 2 Chapter 2 Materials, Methods and Instrumentation

## 2.1 Materials

HCT 116, SW620, PANC-1 and BxPC3 cells were obtained from CRN NCI-60 cell bank initiative, Cancer Biology, Division of Cancer and Stem Cells, School of Medicine, University of Nottingham. Ki-67, BrdU, HRP rabbit-anti-mouse secondary antibody, and DAB were obtained from Pathology Products, Dako UK Ltd (Ely, UK). Hypoxyprobe™-1 (Pimonidazole) was purchased from Hypoxyprobe, Inc (HPI) (Burlington, USA), Dulbecco's Phosphate Buffered Saline (PBS), L-Glutamine solution (2 mM), RPMI-1640, Agarose, DPX mounting medium and Fast red solution were obtained from Sigma-Aldrich (Dorset, UK). Foetal Bovine Serum (FBS) solution was supplied by Invitrogen (Paisley, UK). Trypsin- EDTA was obtained from Gibco, Life Technologies Ltd, (Paisley, UK). Ultra low attachment (ULA) 96-well round bottom plates were obtained from Corning (Amsterdam, The Netherlands). Paraformaldehyde solution (4%) and Alcian blue were purchased from Alfa Aesar, A Johnson Matthey Company (Heysham, UK). Tissue-embedding cassettes were sourced from Simport, (Beloeil, Canada), SuperFrost glass and Poly-L-lysine coated slides were obtained from Menzel (Braunschweig, Germany). Haematoxylin and Eosin were from Raymond Lamb (Eastbourne, UK). Annexin V-FITC Apoptosis Detection Kit was purchased from

eBioscience (Hatfield, UK). Hoechst 33342 (NucBlue® Live ReadyProbes® Reagent) was sourced from Life Technologies Ltd, (Paisley, UK). Doxorubicin (Adriamycin, Pfizer, UK ) was provided by Cancer Biology Unit, Division of Cancer and Stem Cells University of Nottingham, Pegylated Liposomal Doxorubicin Hydrochloride (called Doxil throughout the text for simplicity) (CAELYX®) was purchased from Janssen, (High Wycombe, UK), Rhodamine B Isothiocyanate (RBITC) was purchased from Sigma-Aldrich (Poole, UK), Fluorescently labelled unmodified polystyrene nanoparticles of sizes 30 nm, 50 nm, 100 nm, 300 nm (UNP) and 50 nm aminated (ANP) and 50 nm carboxylated polystyrene nanoparticles were purchased from Magsphere Limited (US) and used without further modifications, poly (glycerol-adipate) polymer with and without modification was provided by Dr Vincenzo Taresco, School of Pharmacy, University of Nottingham, Sephadex G-25 in PD-10 Desalting Columns from GE Healthcare's Life Sciences solutions (Little Chalfont, UK),

## 2.2 Tissue Culture of monolayer and formation of 3D spheroids

### 2.2.1 Routine culture of cell monolayers

HCT 116 (Human colon carcinoma), SW620 (Human colon adenocarcinoma), PANC-1 (Human pancreatic carcinoma) and BxPC3 (Human pancreatic adenocarcinoma) cells were routinely checked for mycoplasma contamination. All cell lines were cultured in T75 culture flasks containing medium (15 ml).

The medium used was RPMI-1640 containing 10 % foetal bovine serum (FBS) and glutamine (2 mM, 2 ml). All media was pre-warmed before utilization in the experiments. Cells were passaged approximately every three days to maintain 80 % confluence. The steps involved washing with sterile Dulbecco's PBS before the addition of trypsin- EDTA (0.05%, 2 ml) solution to induce cell detachment at 37 ºC for approximately 3 min, the RPMI-1640 medium was added (8 ml), and the cells were harvested at 300 × g for 5 min. The cell pellet was re-suspended in the medium (10 ml) and passaged into fresh medium in a T75 flask at 1:20 dilution. In all experiments, cells were incubated in a 5 % $CO_2$ air-humidified atmosphere at 37 ºC.

### 2.2.2 Freezing and thawing cell stocks

Cells cultured to approximately 80 % confluence were washed in sterile PBS and detached using trypsin, as described above. Cells were then re-suspended in RPMI-1640 medium (5 ml) and centrifuged at 300 × g for 5 min. The supernatant was removed following centrifugation, and the remaining pellet was resuspended in freezing medium consisting of RPMI-1640 medium with FBS (90 %) and DMSO (10 %). Aliquots (1 ml) were placed in cryovials and frozen in a Mr Frosty containing propane-2-ol at -80°C for 16 h. Cryovials were transferred to liquid nitrogen (-196ºC) for long-term storage.

Cells were removed from liquid nitrogen and defrosted by incubation at 37ºC. The defrosted cell suspension was then added to RPMI-1640 medium (10 ml) and centrifuged at 300 × g for 5 min. Following this, the supernatant was

aspirated to remove the freezing medium, and the pellet was resuspended in growth medium (5 ml). This was added to a T75 flask containing medium (15 ml), and the flask of cells was incubated until conditions for passage were reached. The medium was changed every 48 h until this time. All cells were maintained for several passages (2-5) before being used in experiments, ensuring full recovery from freezing.

### 2.2.3 Generation of 3D spheroids

A high-throughput method for the culturing of spheroids was designed in-house by Ivanov et al. (2015) [110] for the production of neurospheres and was adapted to generate spheroids from colorectal and pancreatic cancer cells. Ultra low attachment (ULA) 96-well round bottom plates were employed for the method. Cells grown as a monolayer were detached using trypsin then centrifuged, and the cell number was counted using a haemocytometer. Different size spheroids were generated by diluting the single-cell suspensions in RPMI-1640 medium to different cell densities (5000, 10000, 25000, 50000 cells per ml) that were added at a constant volume (200 µl) per well in 96 well ULA plates in sextuplicate. The plates were centrifuged at 100 x g for 4 min. The medium (150 µl) was removed on days 3 and 5 and replaced with fresh medium (150 µl) using a multichannel pipette (care was taken not to remove spheroids while doing so).

## 2.3 Characterisation of 3D spheroids

### 2.3.1 Growth kinetics

Different seeding cell densities were screened ranging from 1000 to 10000 cells per well. Spheroids were imaged daily for 7 days using a Nikon Eclipse Ti microscope with a 4x objective (Nikon limited, Surrey, UK). The pictures were analysed using image J and a macro written by Ivanov [108]. The diameter and volume of spheroids were determined by measuring their cross-sectional area. Briefly, the macro converts pictures of spheroids to black and white using the Yen thresholding algorithm. It removes any artefacts from the image, separates it from debris and determines the area by measuring the maximum and minimum Feret diameter of the spheroid. The maximum Feret diameter measures the longest distance between any two points of the spheroid boundary and the minimum Feret diameter measures the minimum distance between the boundaries of the spheroid. Variation in the area determination between the algorithm and manual measurement was found to be less than 5%.[108] From the measured area (S) of the 2D projection of the spheroids the radius ($r = \sqrt{\frac{S}{\pi}}$) and the volume ($V = \frac{4}{3}\pi r^3$) of an equivalent sphere were calculated in Excel.[108]

### 2.3.2 Immunohistochemical Analysis of Spheroids

Prior to processing, spheroids were transferred from the 96 well plate into Eppendorf microcentrifuge tube using 1 ml pipette. Six spheroids of the same condition were used per each tube. Care was taken to aspirate majority of the remaining media from the tube and 1 ml paraformaldehyde solution (4%) in PBS was added to fix the spheroids. Incubation with fixative was 15 min for monolayers and 1 h for spheroids followed by two washes with PBS (150 µl / well). When not used immediately, spheroids were stored in the tubes at 4°C for later use. Prior to wax embedding, fixed spheroids were pipetted out of the Eppendorf microcentrifuge tube and transferred on top of a plastic cryo embedding cassette, and the supernatant was removed by gentle aspiration using a p1000 pipette tip. Warmed low gelling liquid agarose (2% w/v in sterile water, ~800 µl) was gently added to the cassette covering the spheroids, the spheroids were then arranged to be within close contact using thin forceps and were left to set. Once the agarose solidified the tip of a 200 µl Eppendorf microcentrifuge tube was used to cut out the spheroids in the agarose, and the piece of the agarose containing the spheroids was transferred into a biopsy tissue-embedding cassettes (containing 6 compartments) and was processed using a routine paraffin embedding technique (Leica EG1160, Keynes, UK). Four samples per biopsy cassette were processed and paraffin embedded at the same time which made the process more efficient. Sections of 4 µm thickness were cut using a microtome (Leica RM2135, Keynes, UK), placed on SuperFrost glass slides and allowed to dry for 1 h at 37°C. The tissue sections were deparaffinized by 3 changes of xylene for 5 min, washed in two baths of

methanol (100%) to remove all traces of xylene, followed by a wash with methanol (80%) and 2 washes in methanol (70%) for 2 min each and then rehydrated in water. After the staining (see below) slides were mounted using DPX mounting medium.[71]

#### *2.3.2.1 Spheroid morphology- Haematoxylin & Eosin*

The samples were stained with Haematoxylin and Eosin (H&E). The staining system contains two dyes; Eosin is negatively charged and stains basic cell components in a cell red or pink. Haematoxylin is positively charged and stains acidic components such as such DNA/RNA in the nucleus blue. After deparaffinization of the spheroid slides, as described above, slides were rinsed in distilled water for 1 min; the sections were incubated in pre-filtered Mayer's haematoxylin for 3 min and rinsed in running tap water for 1 min. The sections were then incubated with pre-filtered Eosin for 3 min and rinsed in running tap water for 1 min. The sections were dehydrated through three methanol baths (100%), 1 min each, and cleared in 2 baths of xylene, 5 min each. The slides were mounted in coverslips with DPX, air dried overnight, and spheroid sections were assessed by microscopy (Leica DMLB, Leica, Milton Keynes, UK).

#### *2.3.2.2 Spheroids Viability- PI/ annexin V assay*

The localisation of dead and apoptotic cells in the spheroids was performed using a DNA-specific fluorochrome, propidium iodide (PI), and annexin V – FITC. PI is impermeant to live cells and apoptotic cells but can bind to the nucleic acids of dead cells giving them red fluorescence. The Annexin V binds to phosphatidylserine exposed on the outer surface of the plasma membrane of only apoptotic cells. Spheroids were generated in 96 well ULA plates and resuspended in RPMI-1640 (200 µl) per well. The spheroids were stained within the wells as follows: the spheroids were washed twice with PBS, and the Annexin V-FITC labelling solution (100 µl/ well) was added. The solution was prepared by adding Annexin V-FITC (30 µl) and PI (30 µl) to the binding buffer provided in the kit (1ml). Spheroids were incubated for 1 h at room temperature. Wells were washed with PBS, and Hoechst 33342 solution was added and left to incubate at room temperature for 30 min. The localization of PI and annexin -positively stained cells within the spheroids were assessed by wide-field fluorescence microscopy (Nikon Eclipse Ti Nikon limited, Surrey, UK).

#### *2.3.2.3 Localisation of Cellular proliferation- Ki67*

The spheroids sections were stained for Ki-67 protein to evaluate the presence of proliferation gradients in the spheroids. Ki-67 is a large nuclear protein (345 or 396 kDa) expressed in G1, S, G2 and M phase of the cell cycle. Because the

protein is not present in the resting phase, G0 it can be directly related to cellular proliferation. The procedure was performed as follows: slides were deparaffinized as described in the previous sections and incubated in hydrogen peroxide for 15 minutes. Slides were rinsed in 2 baths of Methanol (100%), 1 min each, and rinsed in tap water for 1 min, then slides were microwaved in Citric Acid Buffer pH 6 at 98ºC for 30 min (for antigen retrieval) and placed immediately in running tap water. Slides were washed in PBS for 5 min, and sections were incubated in rabbit serum for 15 min in order to block available charges and prevent non-specific binding. Sections were incubated with primary antibody monoclonal MIB-1 (46 mg/L) (1:200 in PBS) for 60 min. BrdU (262 mg/L) was used as a negative control and was diluted 1:200. Sections were rinsed in 2 baths of PBS, 3 min each, followed by incubation with HRP rabbit-anti-mouse secondary antibody (1.3 g/L) at 1:300 dilution in PBS for 30 min. Slides were rinsed in two baths of PBS, 3 min each, followed by incubation with DAB for 3 min and rinsed with running tap water for 1 min. Sections were counter-stained with Haematoxylin for 3 min and rinsed with running water until no colour was observed. The sections were dehydrated through methanol baths (3 x 100%), 1 min each, then cleared by 2 changes of xylene, 5 min each. The slides were coverslipped with DPX, air dried overnight, and spheroid sections were assessed by bright field microscopy. The positive control for the experiment was liver cancer tissue.

### *2.3.2.4 Development of hypoxia- Pimonidazole assay*

Hypoxia detection was performed by using Pimonidazole hypochloride (PIMO). PIMO forms stable adducts with proteins in hypoxic cells.

Hypoxyprobe™-1 is a commercial name for the substituted 2-nitroimidazole whose chemical name is pimonidazole hydrochloride with a molecular weight of 290.8;

PIMO is reductively activated in hypoxic cells and forms stable adducts with thiol (sulfhydryl) groups in proteins, peptides and amino acids. FITC-MAb1 binds to these adducts allowing their detection by immunochemical means.

The level of PIMO binding was expected to increase as the degree of hypoxia increased. PIMO labelled all hypoxic tissue by binding proportionately to each one, resulting in darker staining where more hypoxia existed. Non-specific binding of antibodies or enzymes to cells without PIMO adducts was prevented by the blocking solution. [114]

Spheroids were incubated for 2h with PIMO at 100 μM final concentration in the media. The spheroids were then fixed and processed for frozen sections. Briefly, the spheroids were then fixed with 4% Paraformaldehyde (PFA) for 1h and after fixation were incubated in 30% sucrose in PBS overnight at 4°C. Spheroids were transferred onto a vinyl specimen mold (CryomoldH, Tissue-Tek, Sakura Finetek, CA). The remaining sucrose solution was aspirated using a micropipette, and the Tissue-TekH Optimal Cutting Temperature compound (OCT) (Sakura Finetek, Torrance, CA) was gently poured over the spheroids. Spheroids were moved towards the centre of the mold by gentle movement

using forceps. Spheroids were then submersed in an isopentane bath cooled by dry ice and cut into 6mm thick sections using a cryostat microtome. The sections were mounted on poly-L-lysine coated glass slides.[58] [115] The slides were then gently immersed in PBS (x10) to remove the remaining OCT compound. PIMO adducts were detected by incubating sections with FITC conjugated MAb1 (monoclonal antibody provided, 1/300) for 2 h at 37 °C. After PBS washes, DNA was stained using DAPI.

#### *2.3.2.5 Presence of Mucins- Alcian blue/ fast red*

Alcian Blue is a basic dye that at a pH of 2.5 is capable of staining mucosubstances such as carboxylated mucins and some weakly sulphated acid mucins within tissues. Fast Red was used as a counterstain, and it stained cytoplasm and nuclei pale pink to red colour. Staining was performed as follows: slides were deparaffinized as described above, and were incubated in acetic acid (3%) for 3 min and stained with Alcian Blue solution for 45 min then washed in running tap water for 2 min. The sections were counter-stained in nuclear fast red solution for 3-5 min followed by washing in running tap water for 1 min, distilled water for 2 min, and dehydrated in methanol (70%, 95%, and 100%), 2 min each. Slides were cleared in xylene, 2x 3 min and mounted with DPX mounting medium. Colon cancer sections were used as a positive control.

## 2.4 Optimisation of FACS/ Hoechst method in HCT 116 spheroids

Spheroids were grown on ULA plates for 3 days to allow for compaction prior to use for the penetration and uptake studies. On day 3 of culture, the media was removed from the wells and replaced with media (150 µl) containing Hoechst (final concentration in the well 0.1 µM, 0. 5 µM, 2 µM and 10 µM) and was left to incubate for 4h. The plate with spheroids was placed back into the incubator. After the end of incubation time, spheroids were washed three times with PBS and processed for FACS or confocal imaging (2.9.1 and 2.9.2).

## 2.5 Preparation of Nanoparticles

*Principles behind the Nanoprecipitation method*

Nanoprecipitation was developed by Fessi and co-workers.[116]The technique is based on spontaneous agitation of the interface between the organic phase and the aqueous phase, involving flow, diffusion and surface processes. [14] The organic phase, made of polymer dissolved in a water-miscible solvent, is poured into the aqueous phase under magnetic stirring. The organic solvent diffuses instantaneously to the external aqueous causing precipitation of polymer followed by NPS formation.[14]

*Method:*

Nanoparticles from PGA and PGA derivatives were prepared by a nanoprecipitation method using acetone as a solvent as previously described by Meng et. [117] Briefly, the polymer (5 mg) was dissolved in acetone (2 mL) containing RBITC (2mg/ml).and the solution was added dropwise into HEPES buffer (5 mL). The mixture was left stirring overnight at room temperature to allow for acetone to evaporate. The unincorporated fluorescent dye from fluorescently labelled NPs was removed by Sephadex PD-10 Desalting Column using gravity flow according to manufacturer protocol.

## 2.6 Characterisation of Nanoparticles

Zetasizer Nano-ZS (Malvern Instruments, Worcestershire, UK), was used to measure size distribution, Z-potential and polydispersity index (PDI) of nanoparticles. Experiments were conducted at 25°C after diluting the nanoparticles to 200 µg/ml in 1 mM HEPES buffer, RPMI-1640 medium and RPMI-1640 medium supplemented with 10% FBS. The mean particle radius was obtained from the Stokes-Einstein equation, and results are presented as the mean particle hydrodynamic diameter +standard deviation of 30 readings. Zeta Potential results are expressed as the mean +standard deviation of 5 readings.

## 2.7 Cytotoxicity of Nanoparticles in HCT 116 cells

A stock solution of resazurin (440 mM in PBS), was aliquotted and stored at -21°C. A working solution of 60 mM resazurin was prepared in RPMI-1640 medium. Media with nanoparticles was added to cells grown as a monolayer in 96 well plate. After incubation for 24 hours, the media with nanoparticles was removed, wells were washed with PBS x 2 and replaced with resazurin working solution (200 µl), and the plates were placed back in the incubator. Fluorescence was measured at an excitation wavelength of 530 nm and emission 590 nm on a FLUOstar Omega plate reader (BMG LABTECH (Ortenberg, Germany) at 3 h after dye addition.

## 2.8 Cell Uptake in HCT 116 monolayer

HCT 116 cells were plated at a density of 2000 cells per well in 96 well plate and allowed to attach. After 72 h media was aspirated and the cells were incubated with NPs (75 µg/ml) or Dox (1 µg/ml or 10 µg/ml or 75 µg/ml as Doxil) in RPMI (supplemented with 10% FBS serum). The free Dox concentrations were chosen to be relevant to the clinical context, as the plasma mean concentration of free Dox in patients receiving a single intravenous dose is 0.2 µg/ml after 1h and 0.1 µg/ml after 4h after which it remains at this level until 24h.[20, 118] Thus in our study the lower concentration of the free Dox (1 µg/ml) is representative of the situation in vivo and the higher concentration is

used to evaluate the effect of an increase of concentration on the penetration through the spheroid. After 2 h incubation with NPs, the medium was aspirated, and the cells were washed with PBS (x3) before imaging via wide-field fluorescent microscopy.

## 2.9 Penetration and uptake in HCT 116 spheroids

Spheroids were grown on ULA plates for 3 days to allow for compaction prior to use for the penetration and uptake studies. On day 3 of culture, the media ( RPMI-1640 with 10% FBS) was removed from the wells and replaced with media ( RPMI-1640 with 10% FBS) (150 µl) containing NPs (75 µg/ml) or Dox (1 µg/ml or 10 µg/ml or 75 µg/ml as Doxil) and was left to incubate for 2h- 24 h. Hoechst was added to the wells (final concentration in the well = 0.1 µM) either before, at the same time as or after the addition of NPs or DOX to allow for complete 4h incubation with the dye and the plate with spheroids was placed back into the incubator. After the end of incubation time, spheroids were washed three times with PBS and processed for FACS or confocal imaging (see methods below).

### 2.9.1 Evaluating the penetration of fluorescent polystyrene nanoparticles by confocal microscopy

*The principle behind Confocal microscopy*

The Laser Scanning Confocal Microscope (LSCM) is a specialized type of light microscope (Figure 4.) The illumination in a confocal microscopy is achieved by scanning of the sample with a laser beam. This laser beam is reflected by a dichroic mirror and passes through the objective lens of the microscope in a focused manner on the specimen, this then excites fluorescence probe in the sample. The light is emitted at a longer wavelength which comes through the dichroic mirror and is again focused at the upper pinhole aperture. Thanks to the addition of the pinhole aperture in LSCM, out-of-focus light is eliminated, as only the information from a single, focused focal plane can pass through the pinhole and reach the detector. This allows a series of optical slices to be acquired from several discrete focus levels, z-stacks, then rebuilding it to view the sample in 3-D. This technique offers greater resolution than fluorescence microscopy due to its point illumination and detection properties. [119–121]

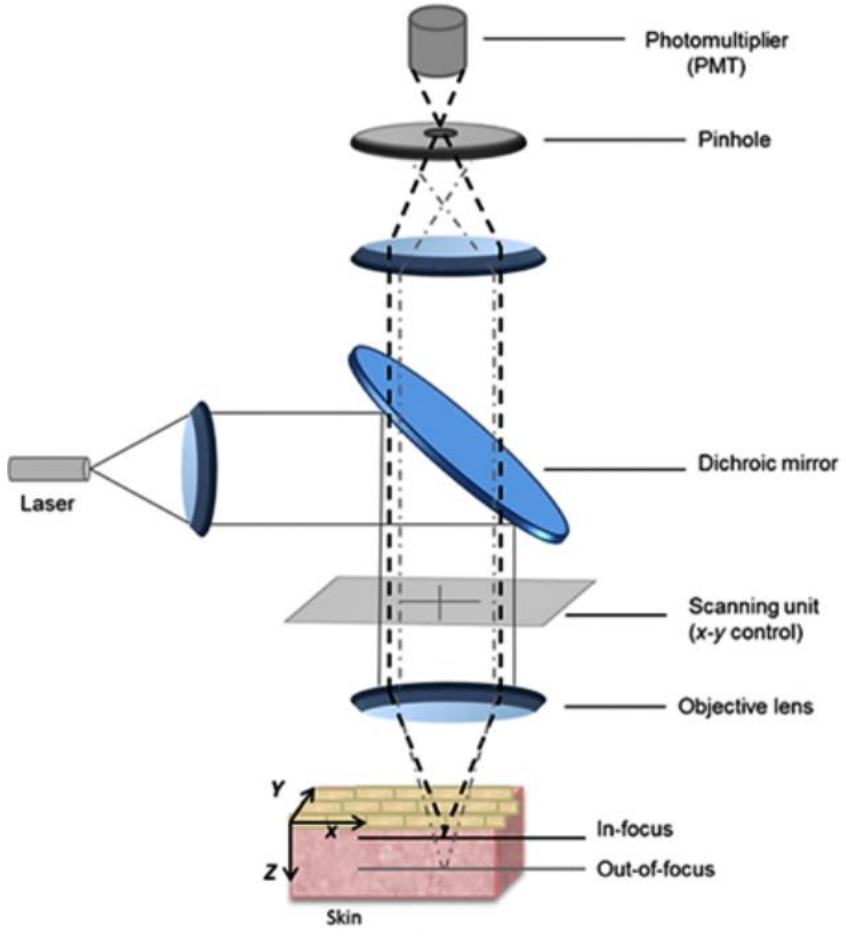


*Figure 4 Schematic of a confocal microscope.* [122]

*Method*

The spheroids were fixed with PFA (4) for 1 h. After fixation spheroids were incubated in 30% sucrose in PBS at 4°C overnight. Spheroids were transferred onto a vinyl specimen mold (CryomoldH, Tissue-Tek, and Sakura Finetek, CA). The remaining sucrose solution was aspirated, and the Tissue-TekH O.C.T. compound (Sakura Finetek, Torrance, CA) was gently poured over the spheroids. 3D spheroids were then submerged in an isopentane bath cooled by dry ice and cut into 20 µm thick sections using a cryostat microtome. The

sections were mounted onto poly-l-lysine coated glass slides and were gently immersed in PBS to remove the remaining O.C.T compound. Subsequently, the frozen sections of spheroids incubated with NPs were examined by confocal microscopy (laser 538nm) and images processed by image J software. The sections from the middle of a minimum of 2 independent spheroids per experiment were selected based on the degree of Hoechst staining, and the experiment was repeated twice. In the image J analysis, the images were pseudo-coloured with mask LUT "fire" that reflect differences in intensity of the nanoparticles within spheroids.

### 2.9.2 Evaluating the penetration and uptake of fluorescent polystyrene nanoparticles by flow cytometry

*Principle behind FACS*

Flow cytometry is a technique that allows the measurement of the physical and chemical characteristics of cells in a fluid as they pass through at least one laser. The flow cytometer is comprised of three main components: the fluidics, the optics and the electronics. (Figure 5)The fluidics system transports the cells in a stream of fluid to the laser beam. The optics system contains lasers which illuminate the cells as they pass in the liquid stream and scatter light. Cells emit light at varying wavelengths which are detected by carefully positioned lenses and direct the light signals to the relevant detectors which emit electronic signals proportional to the signals that hit them. Any cell or particle within the size range from 0.2 to 150 μm can be analysed; however, the cells are required

in a single cell suspension hence If the cells to be analysed come from a solid tissue, or spheroid they are required to be disaggregated prior to FACS analysis. Furthermore, cells or cell components need to be fluorescently labelled. Data can then be collected on each cell and their characteristics based on their fluorescent and light scattering properties. Up to thousands of particles per second can be analysed as they pass through in the liquid stream. (Brown & Wittwer n.d.)

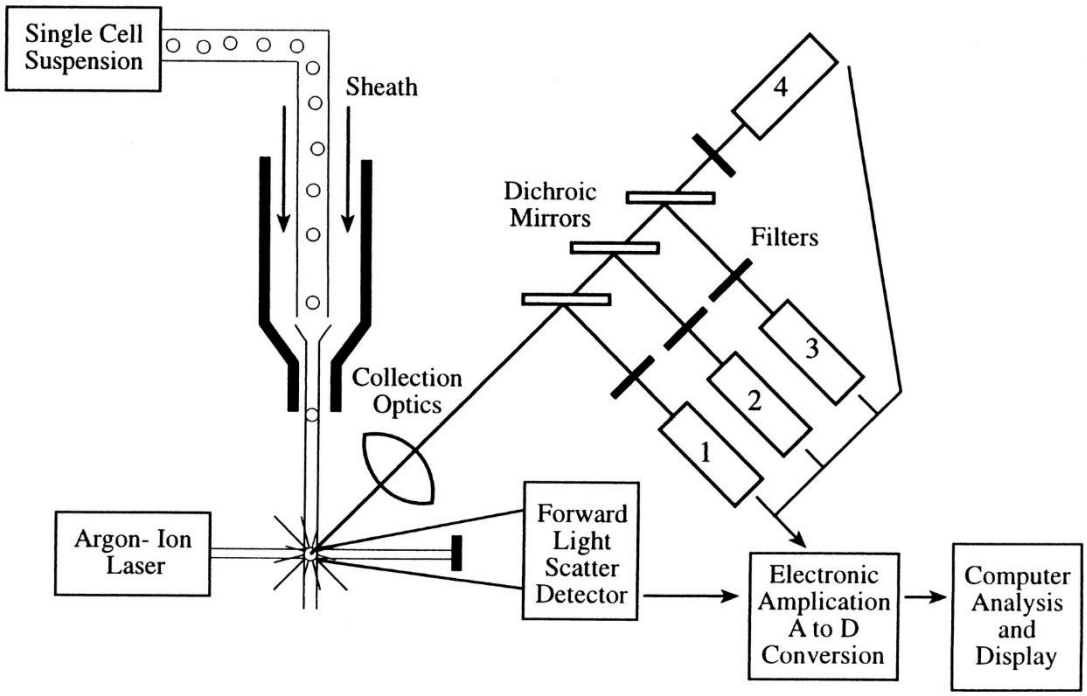


*Figure 5 Schematic representing Flow cytometer.* [123]

*Method:*

After incubation of spheroids with NPs (75 µg/ml medium) or Dox (1 µg/ml or 10 µg/ml or 75 µg/ml as Doxil) for 2 h, 4 h , 6 h and 24h and Hoechst 33342 (0.1 µM) for 4 h the spheroids were transferred into 15 ml Falcon conical tubes and washed twice with PBS (1ml). Accutase (1 ml) was then added and the tubes incubated at 37 °C for 3 min with agitation. The dissociation of spheroids was aided by mechanical pipetting. The spheroids were then centrifuged, washed with PBS and subsequently analysed by flow cytometry (MoFlo Astrios Cell sorter, Beckman Coulter) with a minimum of 8000 events measured per sample.

## 2.10 Statistical analysis

Unless otherwise stated, all data are shown as the mean ± standard deviation (SD), (n = number of spheroids per experiment), with three repeats. The coefficient of variation was calculated as $CV\% = \frac{SD}{Mean} \times 100$ (Acceptance criteria CV% < 20). One way or two-way analysis of variance (ANOVA) was applied for comparison of three or more group means. P value of <0.05 was considered statistically significant. Levels of significance $p < 0.0001$, $p < 0.001$, $p < 0.01$, and $p < 0.05$, are denoted by ****, ***, **, and * respectively. GraphPad Prism 7 software was used for data analysis.

# Chapter 3 Development and characterisation of 3D Spheroid Models

## 3.1 Introduction

The current process for testing the effectiveness of nanosystems relies greatly on animal models. However, with an increasing number of these systems being developed, it is not feasible to test them all using *in vivo* studies which are difficult to use for studying the penetration of nanosystems beyond the vasculature.

Therefore, there is a need for a representative *in vitro* tumour models that will allow the testing of penetrability of nanomedicines in the early stages of the drug development process. While the *in vitro* model should mimic the *in vivo* tumour microenvironment as far as possible, it also should be simple, and easy to reproduce and analyse. [50] We have chosen to work with 3D multicellular tumour spheroids as models for solid tumours as they are believed to closely resemble the tumour microenvironment. [76,77,78,79] Spheroids made of certain cancer lines, such as pancreatic cells or breast cancer were shown to produce some ECM matrix components. ECM is a complex substance composed of collagen, elastin, proteoglycans, GAGs in which cancer cells are embedded. Together these features in a tumour are believed to form a penetration barrier for the therapies. [57,58,59,60,] The ability of 3D cell model to produce ECM is thus paramount to establish the penetration barriers seen *in vivo*, thereby allowing

them to be used to study the penetration, distribution and binding of nanoparticles. [76,1,4,5,96,89,84,50] However, to date, there are limited numbers of studies that employ spheroids for the evaluation of nanomedicines. [58, 112]

The aim of this study was to generate a series of models to identify those with defined features that make them useful for assessing penetration and uptake of nanoparticles.

## 3.2 Results

### 3.2.1 Generation of 3D spheroids

Colorectal and pancreatic cancer cell lines were chosen to be investigated in

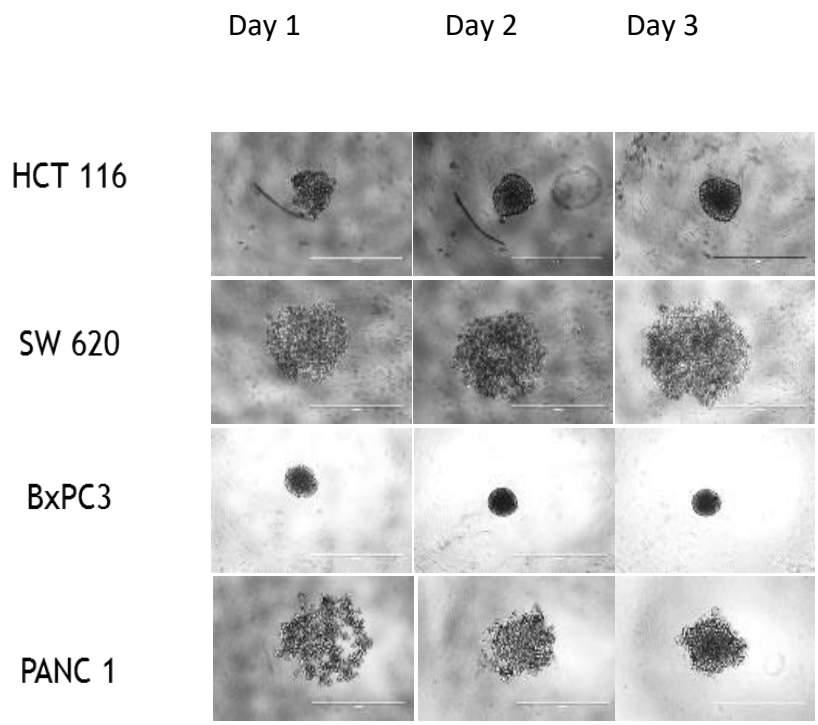


*Figure 6 Phase contrast images of HCT 116, SW620, BxPC3 and PANC 1 cells on day 1, 2 and 3 of spheroid formation using liquid overlay technique. Scale bar 1000 µm.*

the study as they belong to the most common types of cancer and remain the leading causes of cancer-related deaths due to therapy resistance.[125]

The Liquid Overlay Method (Described in the Introduction section 1.3.1.3) was employed for the generation of spheroids. The method uses round bottom plates pre-coated with a hydrophilic polymer. The hydrophilic coating prevents cell attachment to the plastic and influence cell to cell attachment which leads to the formation of 3D structures. The method does not involve the addition of any extracellular support thus rely purely on a natural ability of cells to form spheroids. For initial evaluation two colorectal (HCT 116 and SW620) and two pancreatic (BxPC3 and PANC-1) cell lines were employed in order to evaluate their ability to form spheroids spontaneously. We have chosen these cell lines based on the literature that suggests that colorectal and pancreatic cancer cell lines are capable of forming spheroids probably due to the production of some ECM matrix components.[126]

The images representing their growth and compaction over three days in culture are shown in Figure 6. The results revealed that HCT 116 colorectal cells started to compact after 24 h in culture and attained spheroid morphology after 48 h with a more spherical appearance and defined border observed. However, the SW620 cell line was unable to form compact spheroids after 72 h in culture using this method. The SW620 cells formed loose aggregates and were easily disaggregated by mechanical pipetting even after three days in culture suggesting weak cell to cell contacts. The pancreatic BxPC3 cell line formed much smaller and highly compact spheroids after only 24 h in culture.

PANC-1 cells, on the other hand, produced much larger and looser spheroids that started to compact after three days in culture (Figure 6).

HCT 116 human colorectal carcinoma cell line was chosen as a model system for investigating the influence of seeding density and time in culture on the key characteristics of the spheroids such as the presence of ECM component and development of physiological gradients.

### 3.2.2 Growth kinetics

HCT 116 cells were seeded at different densities 1000, 2000, 5000 to 10000 per well and their growth was monitored and characterised at day 3, 5 and 7. (The spheroids are named by the seeding density throughout the text, i.e. 1k, 2k, 5k and 10k.) One spheroid per well was formed after seeding the desired number of cells in a 96 well ULA round bottom plate.

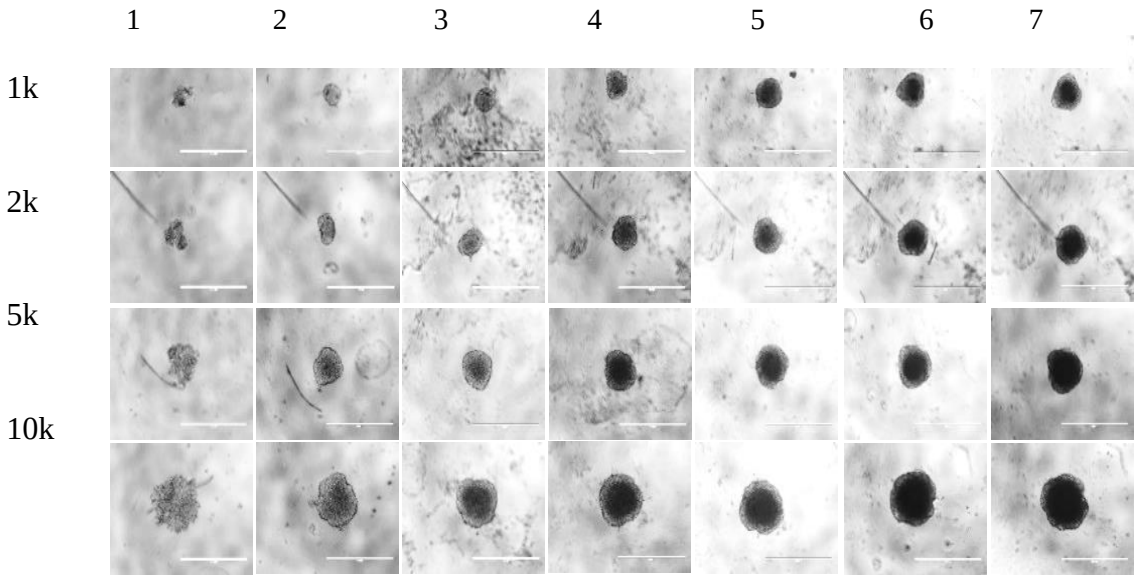


*Figure 7 Images representing HCT 116 spheroid formation and growth using ULA, round-bottom, 96-well plates (1k-10k cells/well, 7 days culture period). Scale bar 1000 µm.*

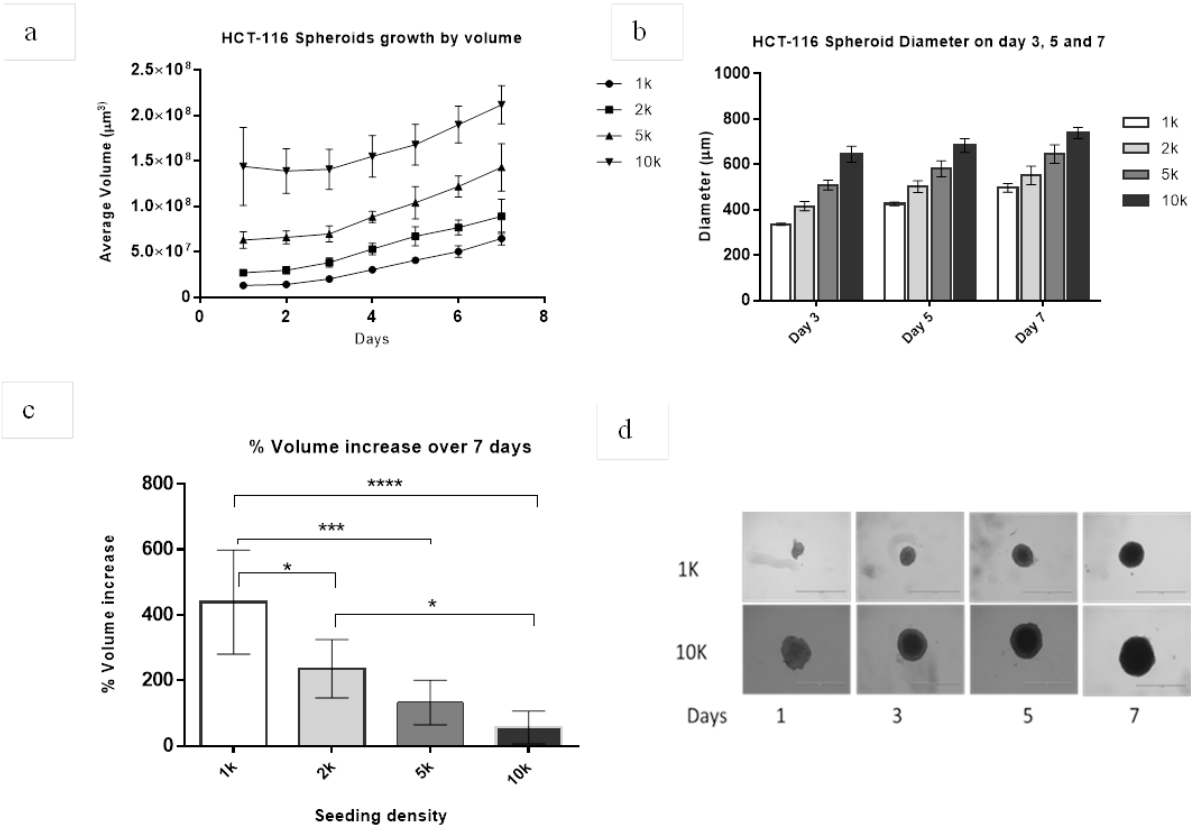


*Figure 8 (a) Growth curves of HCT 116 spheroids of various sizes (seeding 1k, 2k, 5k, 10k cells per well) monitored over 7 days culture; (b) Average diameter of spheroids on different days; (c) Percentage volume increase of HCT 116 spheroids over 7 day culture period; (d) Images of 1k and 10k HCT 116 spheroids demonstrating volume increase over 7 days. Scale bar 1000µm. Values +/- SD (based on 3 independent experiments, 6 replicates of spheroids per experiment). The volume of the spheroids was calculated using ImageJ. Percentage volume increase over 7 days was calculated using the equation: (Day7-day1)/day1 *100. P value of <0.05 was considered statistically significant. ****, *** and * display p < 0.0001, p < 0.001 and p < 0.05, respectively.*

After one day in culture, the cells started to compact as seen in Figure 7. At this stage, they still had an irregular shape and only reached more compact spheroid morphology with a more defined border after 48 h in culture. Figure 8 (a, b) represents the growth kinetics of seeded spheroids over seven days in culture. The spheroids size ranged from 337 µm diameter (1k) to 645 µm diameter for 10k on day 3. The percentage volume increase was 439%, 236%, 133% and 56 % for 1k, 2k, 5k and 10k, respectively (Figure 8 (c)). The spheroids reached diameters ranging from 497 µm (1k) to 739 µm (10k) on day 7 of growth.

The liquid overlay method allowed for the rapid, large-scale production of HCT 116 spheroids, which were easily accessible for further analysis using cellular and biochemical assays. [78] The method was shown to be reproducible with CV in spheroids diameter ≤ 6% (n=6) on day three after seeding. The variation in spheroids size between independent plates on day 3 was CV ≤ 5%.

### 3.2.3 Spheroid morphology and viability

H&E staining was used to observe the morphology of HCT 116 spheroids at different starting cell number and at different times in culture. Figure 9 shows 4 µm cross-sections of spheroids at x10 and x40 magnification, which focuses on the middle section of the spheroids determined based on the order they were cut using microtome and overall section size. It can be observed that on day three all spheroids ranging in diameter from 337-645 µm consisted of layers of tightly packed cells. On day 5, when spheroids reached

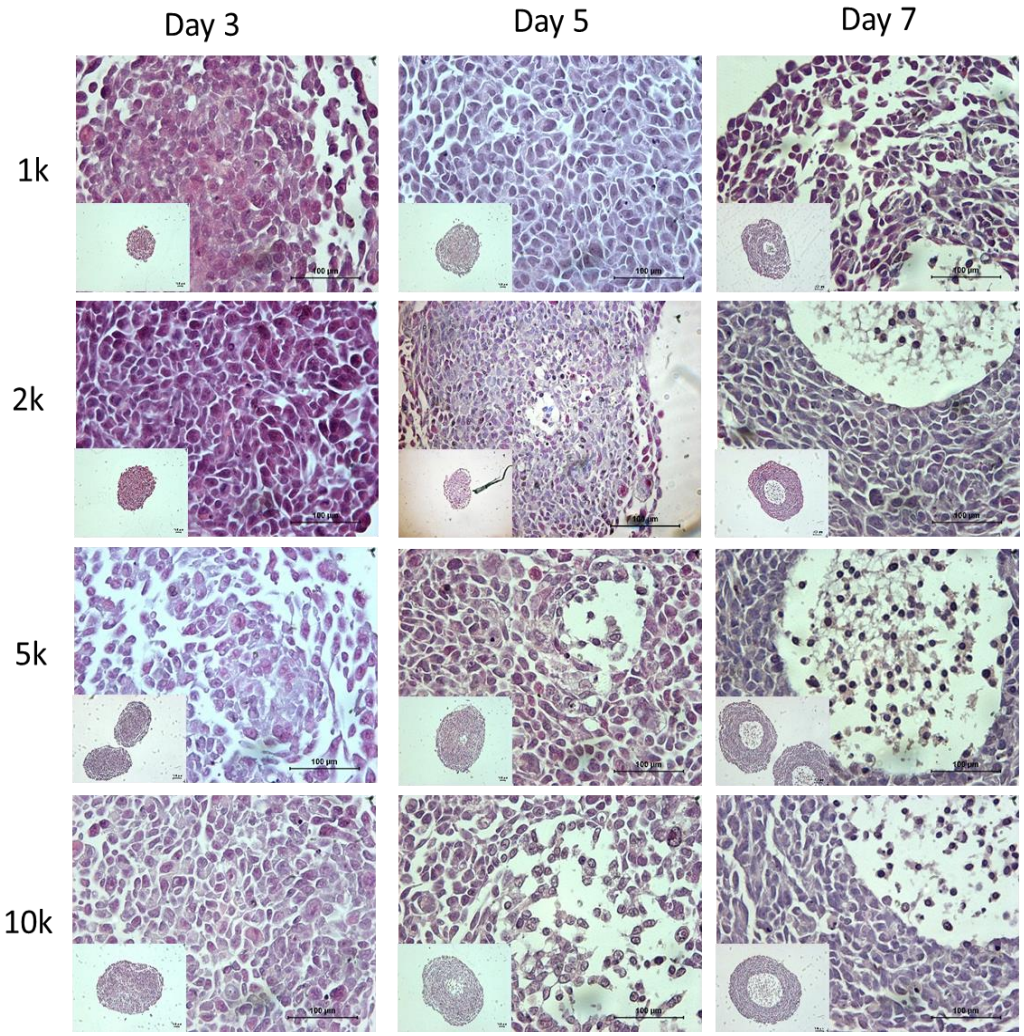


*Figure 9 Immunohistological assessment of the spheroid microenvironment; 4 µm paraffin cross sections stained with Haematoxylin and eosin (H&E) of HCT -116 spheroids grown for 3, 5 and 7 days ( Large images: magnisifcation x 40; small inserts show the spheroids at magnification x 10). Scale bar 100 µm.*

426-684 µm diameter, distorted, less densely packed cells were observed towards the centre of the larger 2k -10k spheroids (502 µm – 684 µm), suggesting the formation of a necrotic core, probably as a result of on-going

cell death due to restricted penetration of nutrients and oxygen. [78, 127] On day 7, the apparent necrotic core clearly increased in size, and at this point, it was present in all the spheroids ranging in diameter from 497 µm to 739 µm.

To further determine whether a necrotic core was being formed, the localisation of apoptotic and dead cells in HCT 116 spheroids was studied by staining them with PI and annexin V-FITC. Propidium iodide stains necrotic cells with magenta fluorescence and annexin stains apoptotic cells green. Figure 10 shows images of spheroids after three, five and seven days in culture. Spheroids on day three contained a small fraction of PI- and annexin V-positive cells distributed sparingly across the spheroids. On day five, clusters of dead, PI-positive cells were detectable in the centre of larger spheroids (5k and 10k) spheroids surrounded by a rim of viable cells confirming the presence of a necrotic core. A small fraction of PI-positive cells was also detectable in the centre on 2k spheroids implying the formation of the necrotic core. The region of dead cells in the centre of the spheroids increased considerably on day 7 of growth, which is consistent with the pattern observed in the H&E staining (Figure 9). The annexin- V staining was visible in all spheroids across all days; however, no clear pattern indicating the increase in apoptosis was detected which could be as a result of the inability of the dye to penetrate deeper into spheroids, thus need to be further investigated.

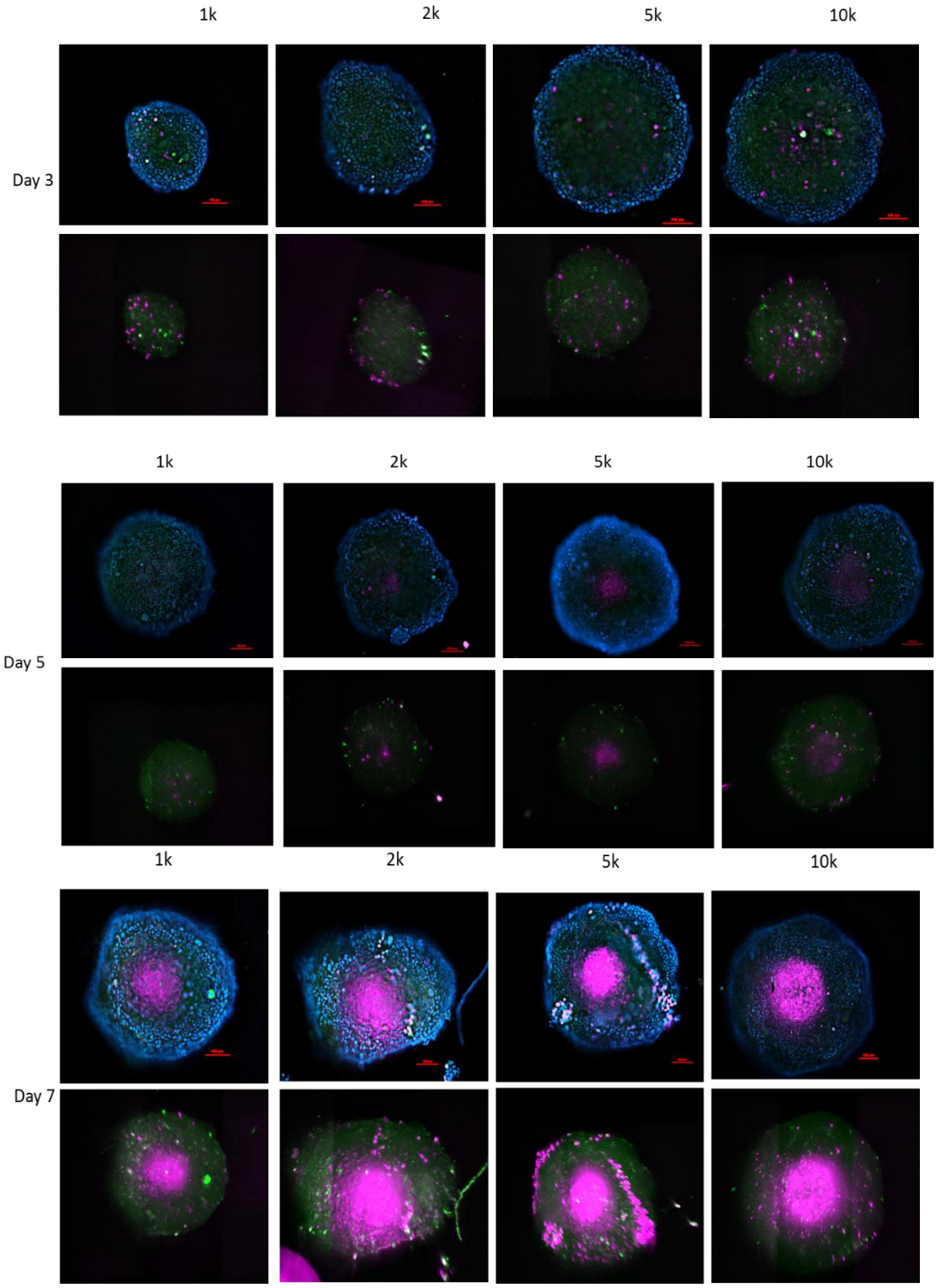


*Figure 10 Dead and apoptotic cells distribution across HCT 116 spheroids. Widefield images of 1k-10k spheroids stained with PI (magenta), Annexin V-FITC (green) and Hoechst (blue) on days 3, 5, and 7 in culture. The top images in each pair of rows illustrate Hoechst stain in individual z slices at 80 µm depth. The bottom images are 3D representations of all Z stacks (Annexin V-FITC and PI channels only). Note: the images were taken on whole spheroids using WIdefield microscopy which has limited capabilities at removing the out of focus information hence the images are of sub-optimal quality. Scale bar 100 µm.*

### 3.2.4 Localisation of cellular proliferation

Ki67 staining was used to identify proliferating cells in the spheroids. The Ki67 positive cells (dark brown nuclei) were evenly distributed across the 1k and 2k spheroids cross-section after three days from initiation (Figure 11). The staining at day 5 shows a decrease in dividing cells in the centre of spheroids with the proliferating cells concentrated towards the rim of the spheroids.

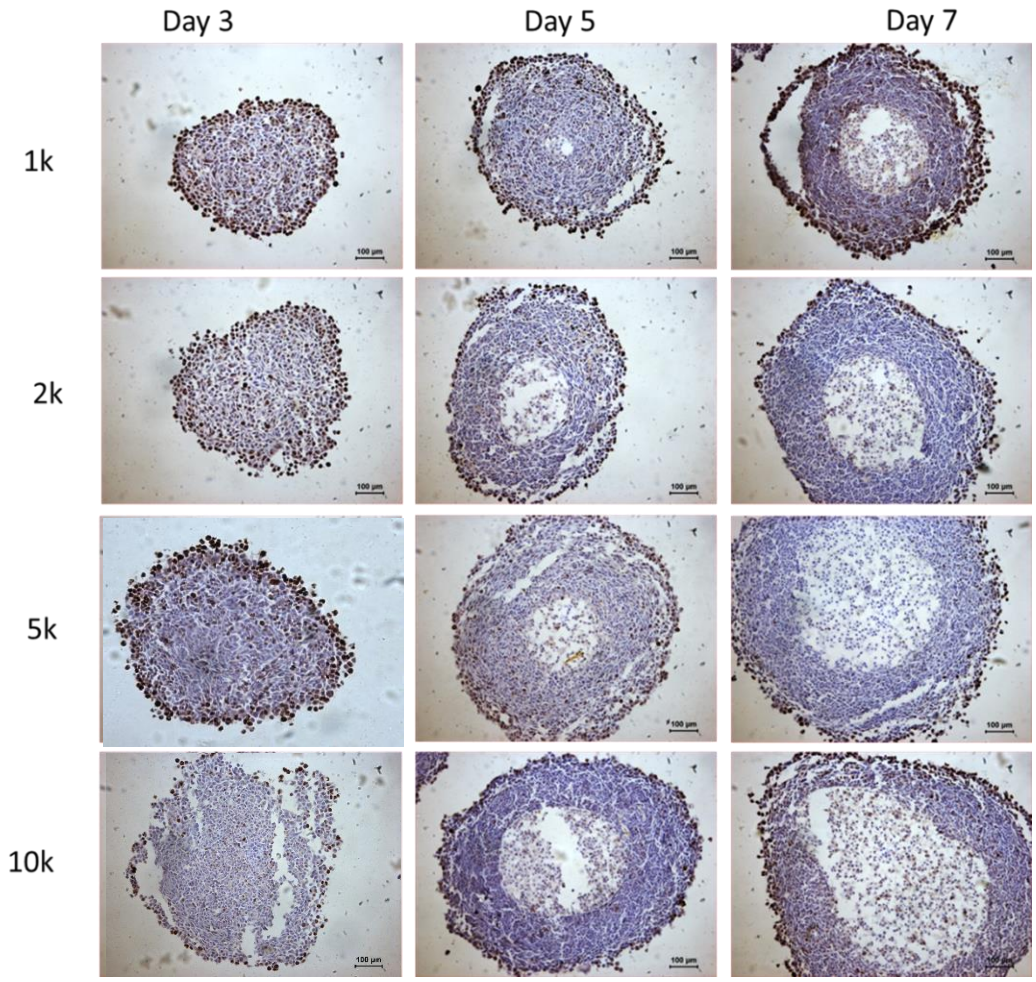


*Figure 11 Immunohistological assessment of spheroids microenvironment; 6µm frozen sections stained with Ki67 proliferation marker (Ki67 positive cells=brown) of HCT 116 spheroids grown for 3, 5 and 7 days. Scale bar 100 µm.)*

The 5k and 10 k spheroids showed less proliferating cells present in the core already after 3 days. On day seven there was a rim of proliferating cells surrounding the well-defined necrotic core at the centre of the spheroids.

### 3.2.5 Development of Hypoxia

The presence of hypoxia in the spheroids was investigated using pimonidazole hydrochloride, a bioreductive chemical probe that forms protein adducts in viable hypoxic cells detected by immunostaining with a specific antibody. The level and intensity of pimonidazole staining, brown, was expected to increase with a higher level of hypoxia. The presence of hypoxia was detected already on day three of culture in spheroids initiated from 5k and 10k (Figure 12). After day five and seven a stronger staining surrounding the well-defined necrotic core developed in these spheroids. No hypoxia was detected in 1k and 2k spheroids after three days in culture, and only a small proportion of positive hypoxia cells were visible after five days in 2k spheroids. Both had a high level of hypoxia in the centre after a long time in the culture of 7 days.

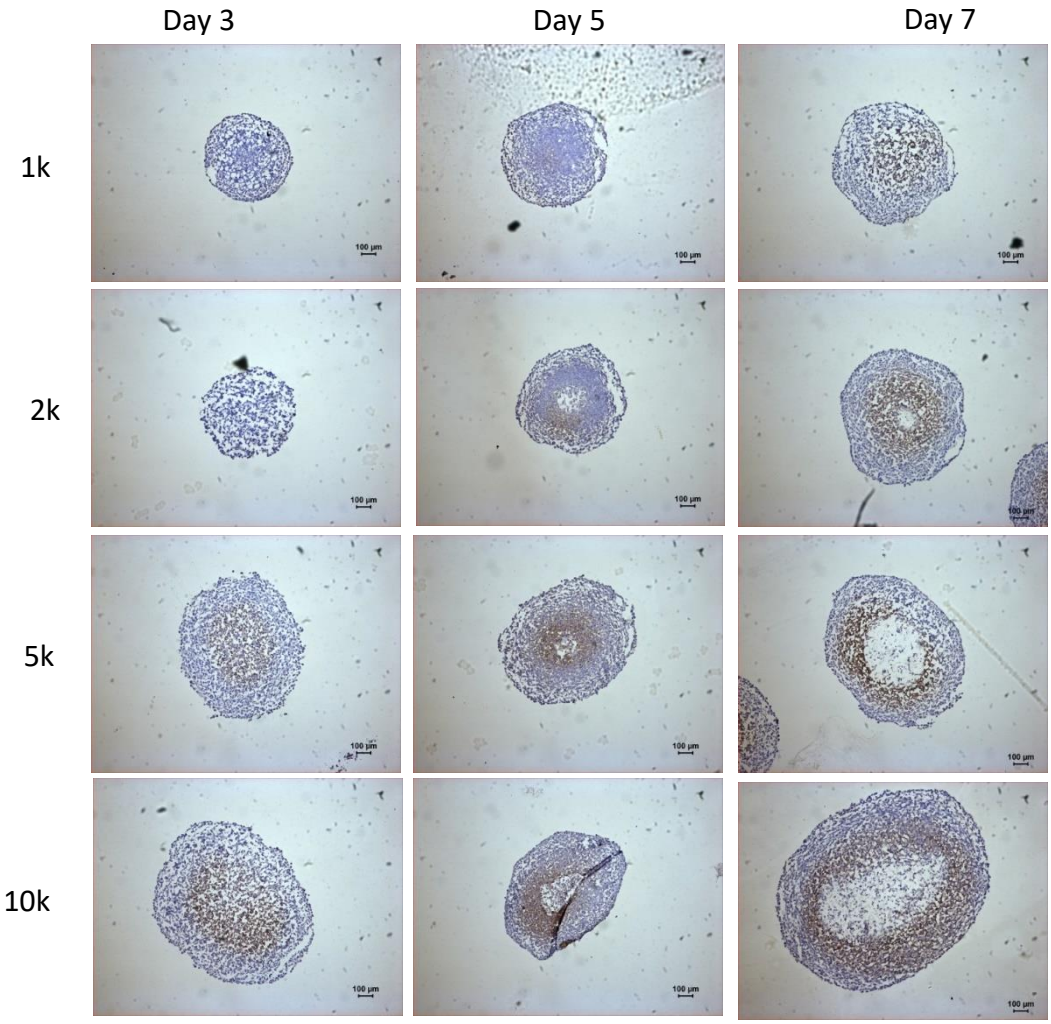


*Figure 12 Immunohistological assessment of spheroid microenvironment; 6 µm frozen cross sections of HCT 116 spheroids grown for 3, 5 and 7 days pre-treated with Pimonidazole and stained by immunohistochemistry. Hypoxia marker, PIMO-positive cells appear brown. Scale bar 100 µm.*

### 3.2.6 Presence of Mucosubstances

To evaluate the presence of ECM components in the HCT 116 spheroids, sections of tumours were stained for GAGs with Alcian blue dye. GAGs or mucosubstances are important components of the ECM, and their overproduction is associated with many types of cancer. As an outcome of the staining the acidic sulphated mucins, hyaluronic acid, and sialomucins are expected to appear blue. The HCT 116 spheroid sections stained at different days in culture are presented in Figure 13. On day three and five blue staining across spheroids can be observed indicative of the presence of the mucosubstances. On day seven, it is clear that the proportion and intensity of the blue dye within spheroids decreased.

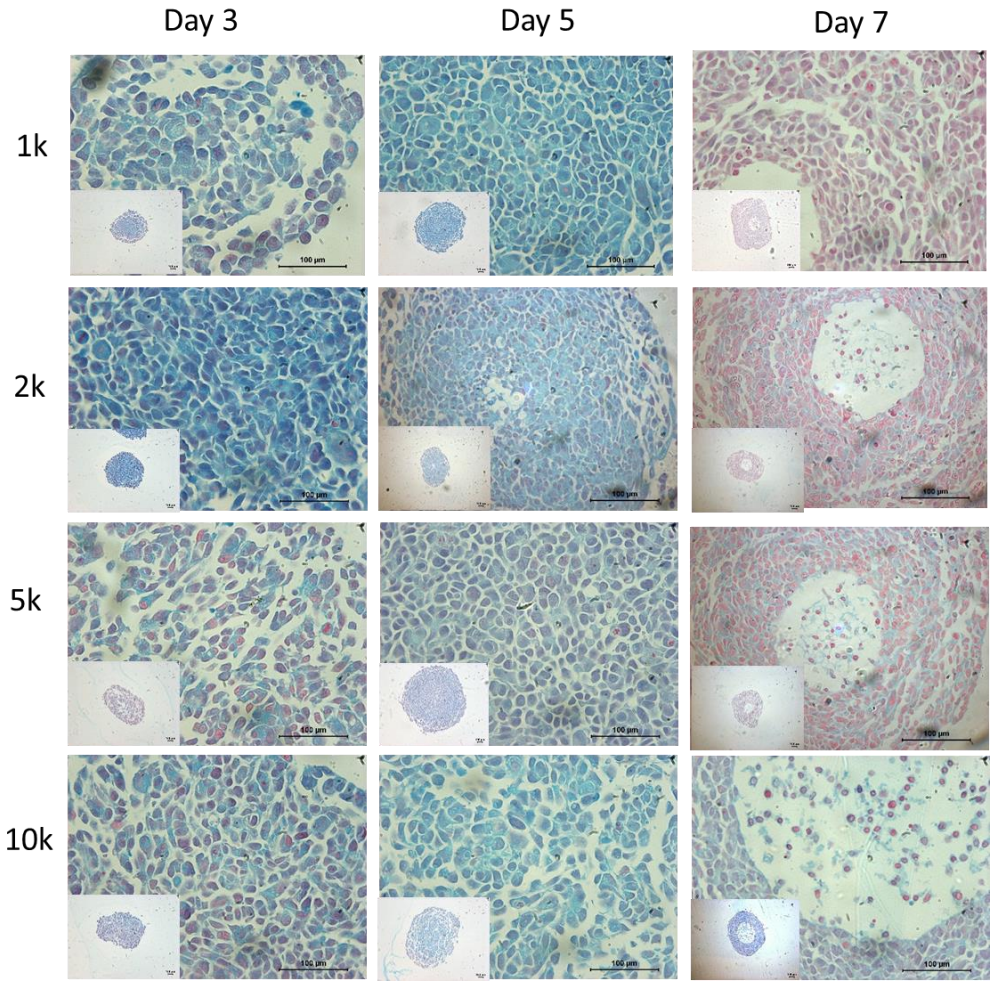


*Figure 13 Immunohistological assessment of the spheroid microenvironment; 4 µm paraffin cross sections stained with Alcian Blue/ fast red for acid mucosubstances and acidic mucins (strongly acidic sulphated mucosubstances- blue; nuclei-pink to red; cytoplasm- pale pink) of HCT -116 spheroids grown for 3, 5 and seven days. Scale bar 100 µm.*

## 3.3 Discussion:

In the study, the screen performed to assess the ability of four cancer cell lines to form spheroids, showed that while HCT 116 and BxPC3 successfully formed tight spheroids, PANC 1 formed looser spheroids and SW620 loose aggregates. HCT 116 spheroids seeded at varying starting cell number (1k, 2k, 5k and 10k) were successfully generated, and immunohistochemical assessment of their morphology, levels of proliferating cells, the presence of hypoxia and ECM components was investigated. The results showed marked differences between models and at various days after initiation. The results suggest that not only the size of spheroids but also the time that the cells are exposed to culture conditions as well as initial seeding density greatly influence the formation of the necrotic core as well as the presence of other pathological features.

The liquid overlay method was chosen for generation of spheroids. The advantages of the liquid overlay method are an easy and rapid generation of a large number of spheroids in a high-throughput manner. However, this method relies on the natural ability of cells to secrete the ECM matrix that then holds them together.[81]

As seen in our screen, some of the cell lines were incapable of reaching the spheroid morphology. The inability to form spheroids may be due to lower levels of ECM production by these cells, but this has yet to be determined. Some breast cancer cell lines, MCF7, T-47D and MDA-MB-435, have been shown to form tight 3D spheroids while other, MDA-MB-231, MDA-MB-468,

SK-BR-3, and MDA-MB-361 formed loose aggregates. [78] Spheroid formation has been shown to improve by the addition to their culture of either individual ECM components such as laminin, fibronectin, collagen or 2.5% liquid reconstituted basement membrane (BD Matrigel).[78] It has been thus suggested that the formation of spheroids relies upon the interactions of cells with ECM proteins such as integrin ß1 or fibronectin. E-cadherin-mediated cell-cell adhesion was also shown to be a key in the compaction process.[89] Although the addition of components such as Matrigel may be beneficial for spheroid formation, it has to be borne in mind that using mouse-derived products is not ideal as this can alter cell properties. Moreover, these products vary in composition from batch to batch and are relatively expensive which should be taken into the account when considering large-scale production. However, these steps may be necessary if one would like to study particular cell line in the 3D arrangements, such as SW620, which does not have an ability to reach 3D architecture spontaneously.

Different seeding densities of HCT 116 spheroids were applied, and generated spheroids were characterised at the various stages of their formation process to establish a model for the study of penetration of nanoparticles. Over the seven-day growth period, different proliferation capacities in relation to the seeding number were observed. Initiation of spheroids using lower seeding density (1k) lead to significantly higher volume increase over seven-day growth when compared to higher seeding densities. Similar results were observed by Ivanov et al. who proposed that the growth of larger spheroids was hindered by the constant volume of medium and the geometry of the well. [108]

Another explanation for the slower growth of 10k spheroids could be that due to the larger size the penetration of nutrients is limited to a greater extent which leads to ongoing cell death and slower growth.

The results from immunohistochemistry suggest that formation of features such as hypoxia, necrotic core etc. is influenced not only by the size of spheroids but also the time in culture as well as starting seeding cell number. In the literature, the 500 µm diameter of the spheroid is often considered to be a critical size above which the necrotic core develops.[106,112] Thus the 200-500 µm spheroids are often employed for drug efficacy studies based on the assumption that pathophysiological features that contribute to chemoresistance *in vivo* are developed.[108, 84] In our study spheroids of the same cell origin, initiated from various starting cell numbers were characterised, and they started to develop pathological features at different stages during culture. For instance, in the spheroids initiated from low seeding density (1k), the formation of the necrotic core was observed around day 6-7 and at day 4-5 for 2k, 5k and 10k spheroids. However, on day 3 of growth spheroids did not yet show any sign of a necrotic core despite being around 500 µm or even > 600 µm diameter (5k and 10k). Furthermore, the spheroids of similar size developed varying levels of hypoxia and proliferative gradients at different times in culture. The efficacy of drugs has been found to be greatly affected by microenvironmental factors of cell models such as size, proliferation gradients, hypoxia as well as the presence of ECM. [128 ,129,130,131, 49 132] These factors can create penetration barriers to drugs carriers reflecting on the distribution, binding and bioactivity of these therapies. Moreover, they can lead to changes at the cellular level altering

cellular RNA, protein expression and signalling pathways which can also affect response to the treatment. [84, 133,77, 111]

The HCT 116 spheroids were assessed for the presence of ECM components. The Alcian Blue staining showed the presence of GAGs between the cells in the HCT 116 spheroids. Higher levels were observed during earlier days in culture (day 3 and 5), and a decrease was observed at day 7. This could be due to a decrease of pH and a number of viable cells in the core of spheroid as a result of the formation of hypoxia and necrosis. The similar pattern of ECM production was found in the study which examined the expression of protein E-cadherin, collagen I, VI and fibronectin I. The expression of these proteins, was higher during the early days in culture in PANC-1 cell pancreatic spheroids, and it decreased after day 4. Authors speculated that higher number of ECM proteins is secreted during the formation and compaction phase of spheroid growth. [40, 83] Further, this could potentially be due to the fast metabolic turnover of proteoglycans. The half-lives of some proteoglycans were found to have a very fast metabolic turnover of 3 days. [63]

To study the penetration of nanosystems, it is essential to employ realistic models that are capable of mimicking the penetration barriers observed in a tumour *in vivo*, such as 3D architecture with close cell to cell compact and ECM matrix. GAGs are highly negatively charged molecules located primarily on the surface of cells and in the ECM. GAGs such as hyaluronic acid and heparan sulphate have been linked to transport inhibition of macromolecules due to the formation of a highly viscous and negatively charged

barrier.[134,135,136 46 57]This suggests that HCT 116 spheroids have a potential to establish the penetration barriers seen *in vivo*. [64]

It needs to be noted, that characteristics developed in the HCT 116 model will probably be cell-line dependent as well as method dependent. The HCT 116 model contains homogenous cell populations whereas a tumour has a more complex physiology made of many different cells. Incorporating stromal and immune cells in a cell model could thus influence spheroid environmental changes and onset of features such as hypoxia, proliferative gradients and necrosis. This could also lead to the production of other ECM components such as collagen.

## 3.4 Conclusions:

We hypothesised that several factors such as size, time in the culture and degree of compaction of spheroids will have an impact on the development of the pathological gradients. Different starting cell numbers were seeded per well, and the spheroids were characterised on day 3, 5 and 7 to develop the HCT 116 models with known features. By varying the seeding density, spheroids ranging in diameter from 337 µm on day 3 to 739 µm on day 7 were generated, observing that, by seeding different cell numbers and by exposing spheroids to various times in cell culture we can produce microenvironments that mimic different stages of a tumour. Based on our results it is reasonable to conclude that pathophysiological gradients and development of 3D macrostructure do not depend simply on size but a combination of factors including exposure to culture conditions as well as seeding density.

Table 3 summarises the characteristics of all the spheroids studied based on days in culture. It is clear that spheroids with similar sizes exhibit very different characteristics as a result of different starting cell number and time spent in cell culture. Selected models can thus be employed to evaluate the effect of the various morphological features on the drug efficacy or uptake into cells. These accessible models could thus replace some work with complex and expensive animal models.[76,77]

*Table 3 The summary of characteristics of HCT 116 spheroids at different days. Spheroids within similar size range colour- coded with the same colour; Presence of different features coloured in different shades of red (Paler shade indicating lower level); Green- indicates absence of the feature in the model.*

| Time in culture | Spheroid type | Size (µm) | Necrotic core | Hypoxia | Non proliferative centre | GAGs |
|---|---|---|---|---|---|---|
| Day 3 | 1k | 337 | No | No | No | yes |
| | 2k | 416 | No | No | No | yes |
| | 5k | 509 | No | Yes | No | yes |
| | 10k | 645 | No | Yes | Yes | yes |
| Day 5 | 1k | 426 | No | Yes (low) | Yes | yes |
| | 2k | 502 | Yes ( small) | Yes (low) | Yes | yes |
| | 5k | 581 | Yes ( small) | Yes | Yes | yes |
| | 10k | 684 | Yes ( medium) | Yes | Yes | yes |
| Day 7 | 1k | 497 | Yes (small) | Yes | Yes | yes |
| | 2k | 551 | Yes (large) | Yes | Yes | yes |
| | 5k | 646 | Yes (large) | Yes | Yes | yes |
| | 10k | 739 | Yes (large) | Yes | Yes | yes |

For the initial application for evaluation of nanoparticles in this project, we decided to work with 2k spheroids on day 3 of growth. The cells formed tight spheroids with a defined border and had an average diameter of 430 µm which is representative of the distances observed in a tumour *in vivo*. Immunohistochemical analysis revealed that spheroids consisted of layers of tightly packed, mainly viable proliferating cells with no necrotic core nor hypoxia present at this stage. We chose to work with this simpler model to avoid the interference of the features such as hypoxia or necrosis with the penetration study. The more complex models may be employed in the future to evaluate the effect of these particular features on the uptake and efficacy of therapeutics. The results also revealed the presence of GAGs components suggesting the model has a potential to mimic some of the penetration barriers seen *in vivo*.

Furthermore, the study highlights that it is crucial to characterise cell models and define their pathological features prior to the application in screening of drugs and NPs *in vitro*.

# Chapter 4 Evaluation of penetration of small drug molecules in 3D spheroids

## 4.1 Introduction

An anticancer drug must penetrate through a complex tumour microenvironment compromised of multiple cell layers and abundant in ECM to reach the target cancer cells. Further, to be effective, it must reach all the cells in a tumour in a pharmacologically effective concentration, which is often found to be difficult. Chemotherapy is the most widely used non-surgical treatment for solid tumours; however, limited efficacy is often observed due to tumour resistance.[128] The population of non-cycling cells deeper in a tumour can often survive the treatment and subsequently cause a relapse of the disease. Moreover, some anticancer drugs are thought to exert a weaker toxicity in acidic or nutrient-deprived microenvironments, which are often found in avascular parts of a tumour.[53–55] A range of different cellular mechanisms such as P-glycoprotein drug export pumps, alteration in the expression of topoisomerases and variation in DNA apoptosis pathways have also been linked to drug resistance. [137] Most research investigating tumour drug resistance, however, have focused on the cellular mechanism via genetic alteration while the aspect of tumour environment and limited diffusion of therapeutic agents in tumours have not been well understood. [80] Some drugs may have poor penetration capabilities within an interstitial space due to

tumour microenvironmental factors. This can lead to cells located further away from blood vessels being exposed to sub-therapeutic concentrations of the drug.[1, 138,137]

Dox, a broadly used chemotherapeutic drug used for the treatment of many solid tumours, has shown limited availability and disappointing therapeutic effect in many cases. In an attempt to enhance the therapeutic index of the drug a new class of drug delivery system of Dox has been developed. This is a PEGylated liposomal doxorubicin formulation (doxorubicin HCl liposome injection; Doxil® or Caelyx®) with a size diameter of ~80-90 nm. This liposomal system has shown advantages over free drug by improving accumulation at a tumour site *in vivo* through the EPR effect and by reducing drug uptake by the reticuloendothelial system which leads to enhanced circulation time.[20] Surprisingly, the overall treatment benefits in patients were still found to be disappointing. It has been suggested that weak therapeutic outcome of the Doxil treatment can be a result of heterogeneous distribution in tumours.

Limited penetration can reduce the efficacy of the treatment and even lead to cancer metastasis or relapse. The knowledge of tissue penetration is thus necessary to understand whether a drug is capable of reaching of all cells in a tumour. Further, this knowledge can drive further improvement of novel delivery methods.

The current process for testing the effectiveness of nanosystems relies greatly on *in vivo* models. While the measurement of average drug accumulation in tumours is a routine test for a new anticancer drug, it does not give information

about its distribution within a tumour.[52] Therefore, there is a need for a representative *in vitro* model and method that will allow testing of anticancer drugs and nanomedicine in the early stages of the drug development process.

3D spheroids have been widely recognised as promising in vitro model as they are capable of mimicking of many characteristics of a tumour *in vivo* (as seen in chapter 3). It is thus reasonable to propose that such model should be used for studying the penetration and distribution of drugs and nanoparticles. However, there is a lack of an easy and reproducible method that can be used for quantitative analysis of penetrability of nanosystems in those 3D models. It is technically challenging to study 3D spheroids using fluorescent optical microscopy due to high levels of light scattering in thick tissue samples.[80] Confocal microscopy provides good image resolution; however, it is still only useful for samples up to ~ 80-90 μm in depth due to limited laser penetration.[113] Other optical methods, such as multiphoton microscopy or light sheet microscopy have the ability to visualise much deeper into the tissue; however, they are not easily accessible and often very expensive. Moreover, the quantitative analysis can be affected due to spill-over of high fluorescence intensity from the external regions of spheroids thereby obscuring less bright signals in the middle of spheroids which could potentially lead to errors in the results. Another approach is to freeze spheroids after the initial drug treatment and cut them into thinner sections (20 μm) using a cryostat. The sections can be then easily studied via optical microscopy. However, the overall process is very time-consuming, and quantification of the penetration/ uptake is

performed on individual sections which do not always represent the conditions across the whole spheroid.

In this section, FACS/Hoechst method was optimised for the screening of the ability of nanocarriers to penetrate into the core of 3D spheroids. Hoechst 3342 dye is a nuclear stain which was found to form noticeable diffusion/consumption gradient as it diffuses through tissue. The Hoechst technique was previously employed *in vivo* to stain perivascular cells in tumours. The dye was injected intravenously and formed a fluorescent gradient from functional blood vessels towards the inside of a tumour. This was followed by a drug treatment and facilitated the study of the effects of vasoactive drugs and chemotherapeutic agents on functional tumour vasculature.[139,140,141] The method was also employed by Durand et al. for the selection of populations of cells with different proliferative status following a drug treatment in spheroids and was found highly sensitive and reproducible. However, the method was considered complex due to the use of fluorescence-activated cell sorting and assessment of cell survival in a colony-forming assay.[142]

In the present work, the FACS / Hoechst method was adapted and optimised for quantification of penetration and distribution of drugs and nanoparticles *in vitro* in the HCT 116 spheroid model. One should note that due to the disaggregation of the cells, only fluorescence associated with the cells either internally or tightly bound to the cell surface will be retained and measured by this method, as drug or nanoparticles remaining in the ECM will be eliminated during the washing steps.

We chose to work with Dox and its liposomal formulation, Doxil, as they represent two different classes of anticancer treatment, a small drug molecule and much larger liposomal nanosystem thereby allowing us to study differences in penetration kinetics between them. Furthermore, they are of interest as both are widely used clinically, yet providing limited availability and poor therapeutic effects in patients.

The FACS/Hoechst technique was employed to directly compare penetration and distribution kinetics of free Dox and Doxil in HCT 116 colorectal cancer spheroids in order to develop a better understanding of factors that influence their performance *in vivo*.

## 4.2 Results

### 4.2.1 Optimisation of FACS/ Hoechst method

The Hoechst staining was optimised by incubating HCT 116 spheroids with different concentrations of the dye (0.1 µM, 0. 5 µM, 2 µM and 10 µM). The dye showed concentration-dependent penetration as expected. It can be observed that by increasing concentration of Hoechst, more cells within the spheroid were stained with the dye. At a lower concentration, the dye has stained cells at the periphery of spheroids only. At 0.1 µM and 0.5 µM the brightly stained population of cells appeared at the rim of spheroids. As the concentration increased, all cells became brightly stained, as shown by confocal images and flow dot plots in Figure 14 a, b.

At 0.1 µM concentration and 4 h incubation in the FACS dot plots, the dye formed a noticeable fluorescent gradient from the rim to the centre of the spheroid. The total population of cells in spheroids was then allocated into 3 segments based on their degree of staining with Hoechst: unstained cells 40 % (+/- 1%) of total cell population, being the cells within the core of spheroid; the brightest 20 % (+/- 1%) of the total cell population, being the cells at the rim of spheroids and weakly stained cells located in the inner segment between the centre and the rim, 40 % (+/- 1%) of total cell population (Figure 14c).

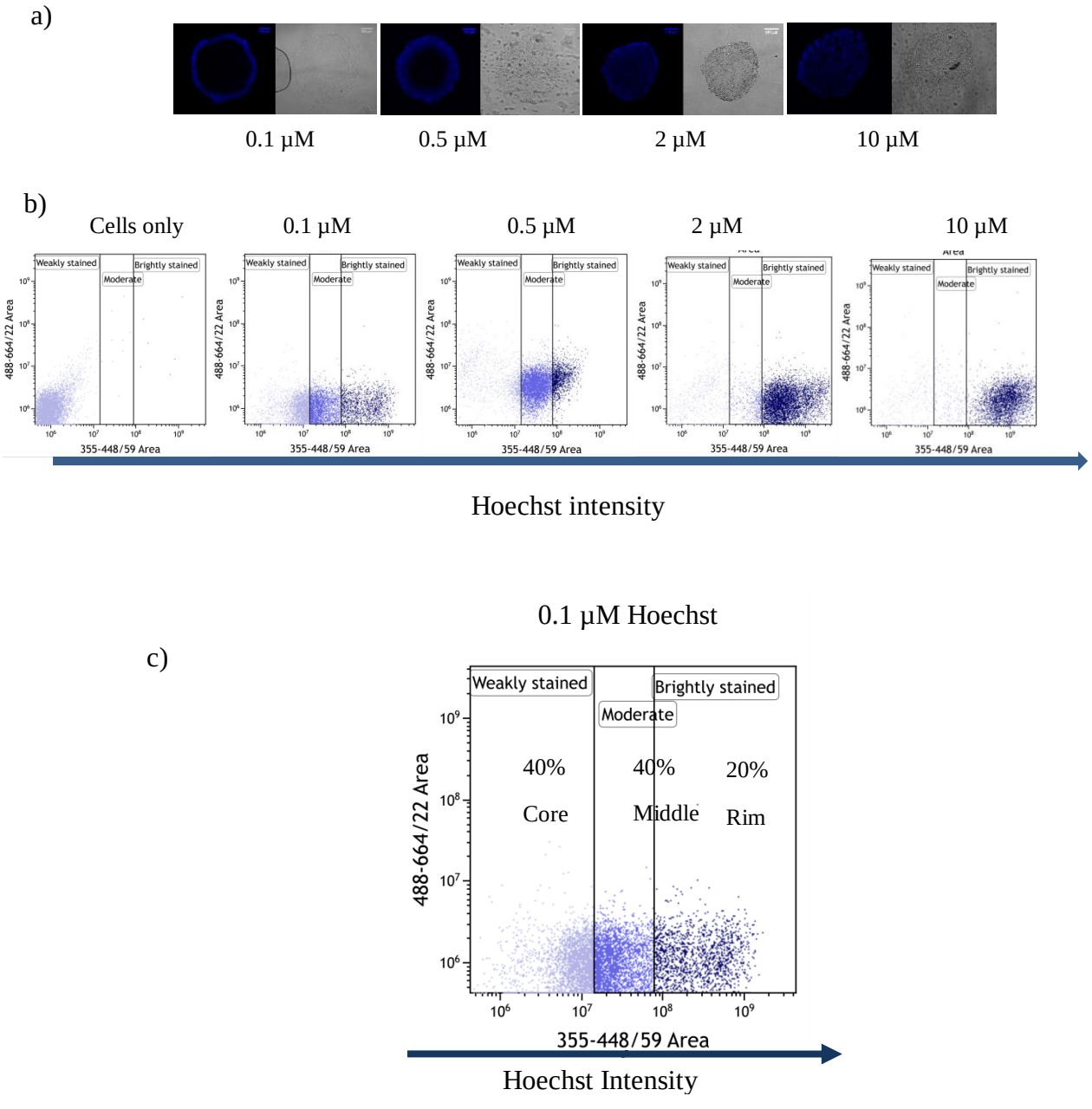


*Figure 14 Concentration-dependent penetration of Hoechst in HCT 116 spheroids incubated with 0.1 µM, 0.5 µM , 2 µM and 10 µM of Hoechst after 4 h incubation (Blue – nuclei stained with Hoechst). a) Confocal images representing the degree of staining of spheroids at different concentrations of Hoechst . b) FACS plots showing the distribution of HCT 116 cells based on the degree of Hoechst staining after tratment with varying concentrations of the dye. c) FACS dot plot of HCT 116 spheroids stained with 0.1 µM Hoechst divided into 3 segments: 40 % (+/-1%) unstained cell population representing the core; 20% (+/-1%) brightest cells representing the periphery and 40% (+/-1%) weakly stained representing cells between the rim and the core of spheroids.*

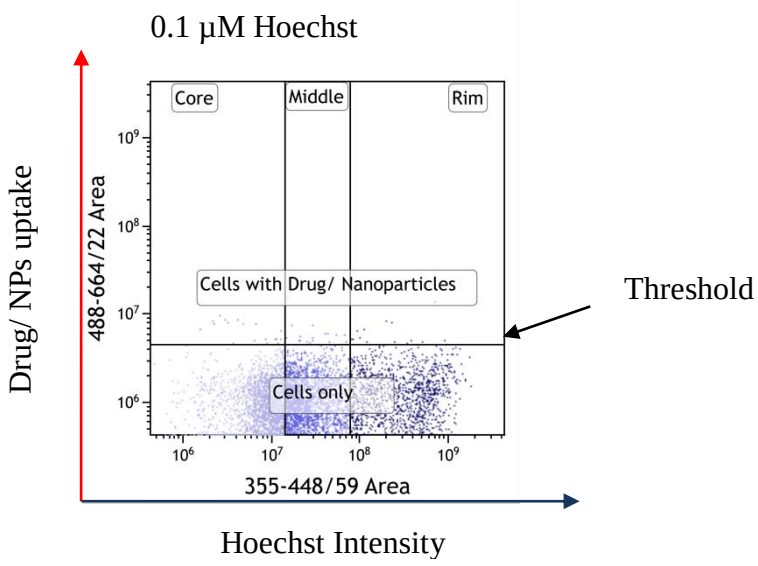


*Figure 15 FACS dot plot of HCT 116 spheroids stained with 0.1 µM Hoechst divided into 3 segments: core , middle and rim.The threshold is set based on cells only sample; In treated samples, cells with nanoparticles appear above the threshold line.*

A concentration of 0.1 µM Hoechst was employed for studying the distribution and penetration of fluorescent drugs and nanoparticles in HCT 116 spheroids.

The spheroids were incubated with 0.1 µM Hoechst for 4 h and with drug or nanoparticles for the desired time in HCT 116 spheroids. The spheroids were then dissociated into individual cells using accutase in combination with mechanical pipetting (for details see section 2); the cells were then fixed and assessed by flow cytometry. The results were quantified using Kaluza software. The cells were gated into brightest ( Rim), intermediate (Middle) and weakly stained cells (Core) and the threshold defining cell without drug or

nanoparticles was set based on the cells only controls stained with Hoechst (Figure 15). The cells with positive fluorescent signal due to fluorescently labelled nanoparticles were quantified and presented as a % + ve out of 100 % cells in each region. The penetration into different regions of spheroids was calculated based on the drug/ nanoparticle uptake in the cells within each region. This threshold, therefore, represents the advancing front of NPs or drug penetration through the spheroid and does not take into account the amount of NPs or drug in any cell in the population.

### 4.2.2 Time-dependent diffusion of Doxorubicin in HCT 116 spheroids

The penetration and distribution of free Dox have been evaluated in HCT 116 spheroids after exposing the cells to different concentrations of a drug 1ug/ml and 10 µg/ml for different incubation periods, 4h and 24h. The free Dox has a fluorescent property which allows for easy detection via confocal microscopy and FACS. The results are qualitatively displayed by confocal images of 20 µm spheroid sections in Figure 16 a and quantified by FACS/Hoechst method in Figures 16 b-d. The concentration of 1 µg/ml of the free Dox was chosen for the study as it is representative of the situation *in vivo*, the 10 µg/ml concentration was included to investigate the effect of drug concentration on penetration into a spheroid. The results show that penetration of free Dox into HCT 116 spheroids is time-dependent as well as concentration-dependent (Figure 16 a). At the lower dose, the free Dox reached less than 50% of cells within the first 2 hours of incubation, 60% after 4h, followed by further

increase up to 80 % of cells after 6h incubation time. At this concentration, it took 24h for the free Dox to reach 90% of cells in the spheroid. Looking at the distribution graphs (Figure 16 c and d) it was observed that at the earlier time point (4h) the distribution was uneven with an insignificant delivery of the drug to the core of the spheroid. A more even distribution into the spheroid is achieved after 24h incubation. By increasing concentration of the free Dox to 10ug/ml, significantly faster delivery into the core of spheroid was achieved, with over 80% cells reached after only 2h incubation. The drug was associated with more than 90% of cells after 6 h incubation.

By looking at the mean fluorescence intensity (MFI) levels, we can detect the level of a drug present in cells across the spheroids. As demonstrated in Figure 17 a-d, it can be noted that the uptake of Dox, at a concentration of 1 µg/ml, across spheroids was highly heterogeneous. Significantly higher accumulation of the therapeutic was observed at the periphery of the spheroid than in the core after 4h incubation. The accumulation of free Dox at a concentration of 10 µg/ml, was still observed to be heterogeneous at the early time point of 4h in the cells across spheroid with a much higher accumulation of Dox in the cells at the periphery of spheroid than in the core. More homogenous accumulation across all regions of spheroid were detected after 24h, as presented in FACS dot plots and quantified in Figure 17 a-d.

16 a)

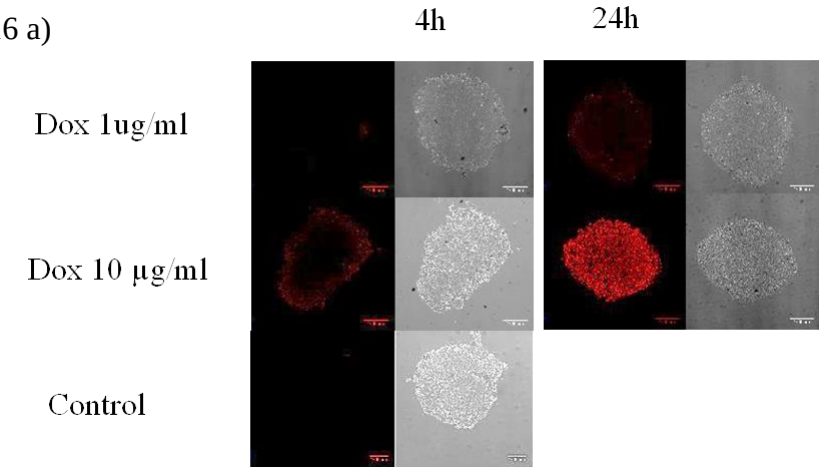
4h
24h
Dox 1ug/ml
Dox 10 µg/ml
Control

16 b)

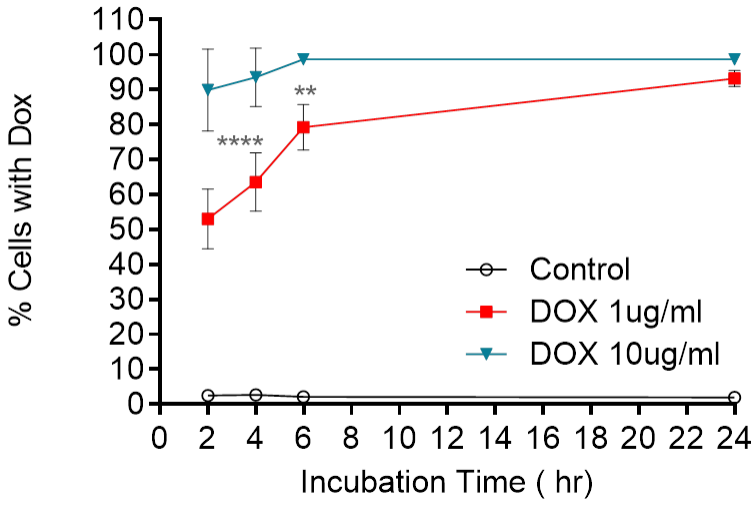
% Cells with Dox
110
100
90
80
70
60
50
40
30
20
10
0
0 2 4 6 8 10 12 14 16 18 20 22 24
Incubation Time ( hr)
****
**
Control
DOX 1ug/ml
DOX 10ug/ml

16c)

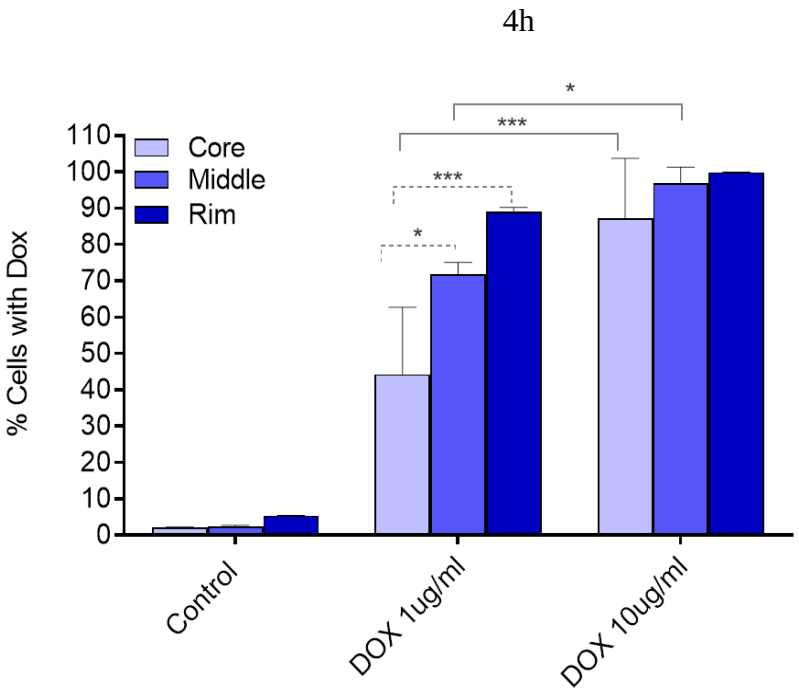


16d)

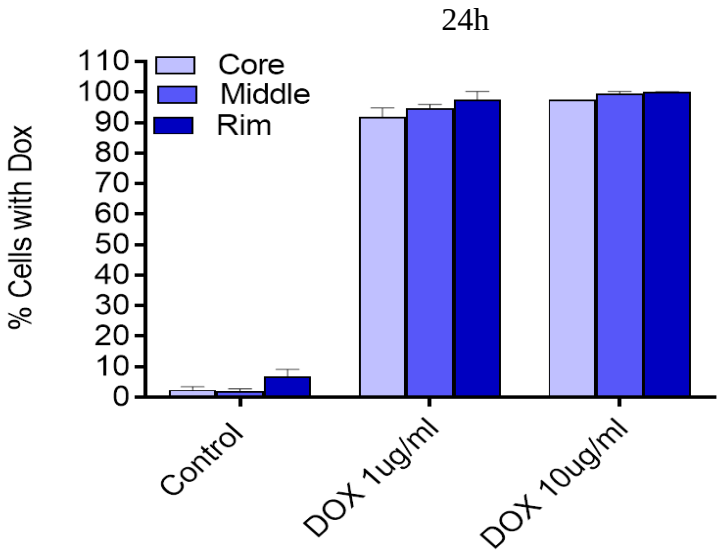


*Figure 16 Penetration of Doxorubicin in HCT 116 spheroids. a) Confocal images of frozen sections (sections = 20 µm) of HCT 116 spheroids incubated with doxorubicin (1ug/ml and 10 µg/ml) for 4h and 24h Scale bar 100 µm. b) Time-dependent penetration of Doxorubicin (1µg/ml and 10ug/ml) in HCT 116 spheroids by FACS. c),d) % cells reached by the free Dox and Doxil across different regions in spheroids after 4h and 24h incubation time. (****, ***, **, and * display $p < 0.0001$, $p < 0.001$, $p < 0.01$, and $p < 0.05$, respectively).*

a)

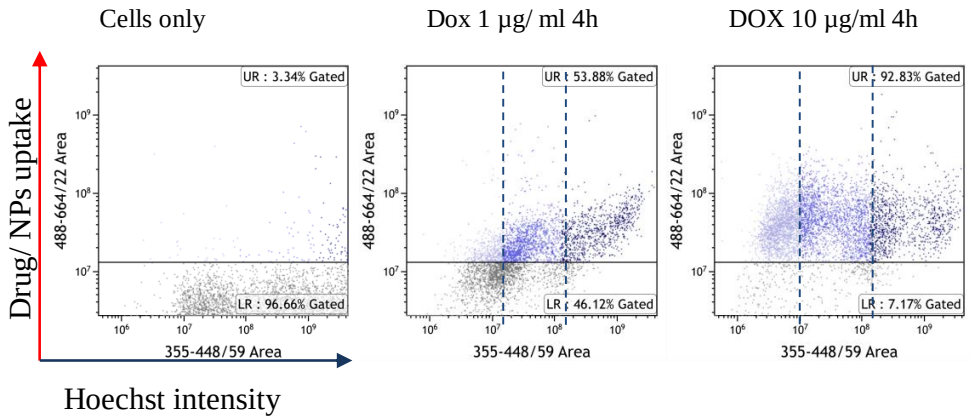
Cells only
Dox 1 µg/ ml 4h
DOX 10 µg/ml 4h
Drug/ NPs uptake
488-664/22 Area
355-448/59 Area
UR : 3.34% Gated
LR : 96.66% Gated
UR : 53.88% Gated
LR : 46.12% Gated
UR : 92.83% Gated
LR : 7.17% Gated
Hoechst intensity

b)

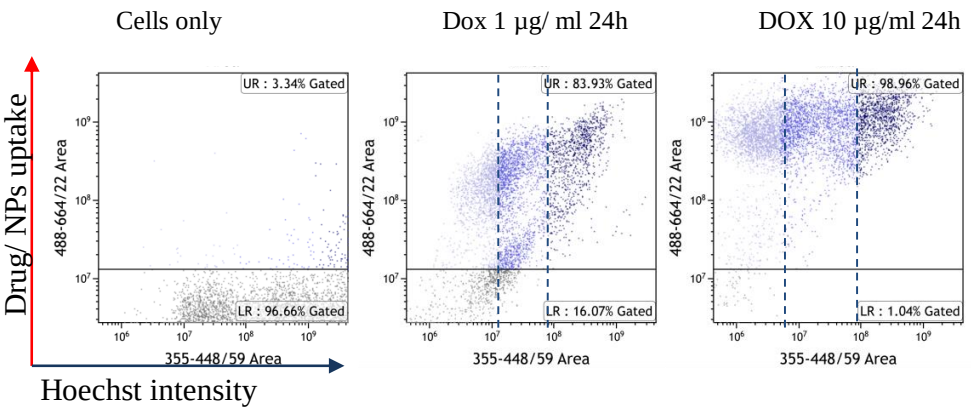
Cells only
Dox 1 µg/ ml 24h
DOX 10 µg/ml 24h
Drug/ NPs uptake
488-664/22 Area
355-448/59 Area
UR : 3.34% Gated
LR : 96.66% Gated
UR : 83.93% Gated
LR : 16.07% Gated
UR : 98.96% Gated
LR : 1.04% Gated
Hoechst intensity

c)

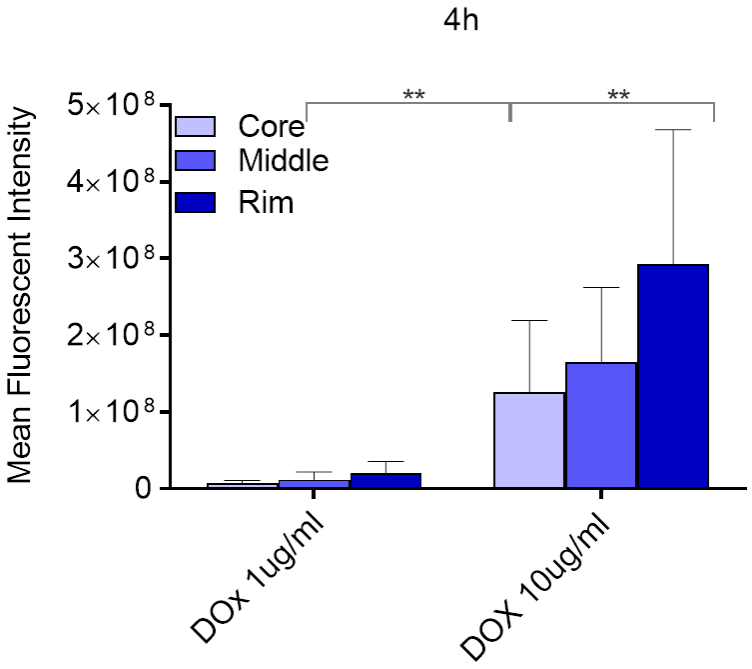


d)

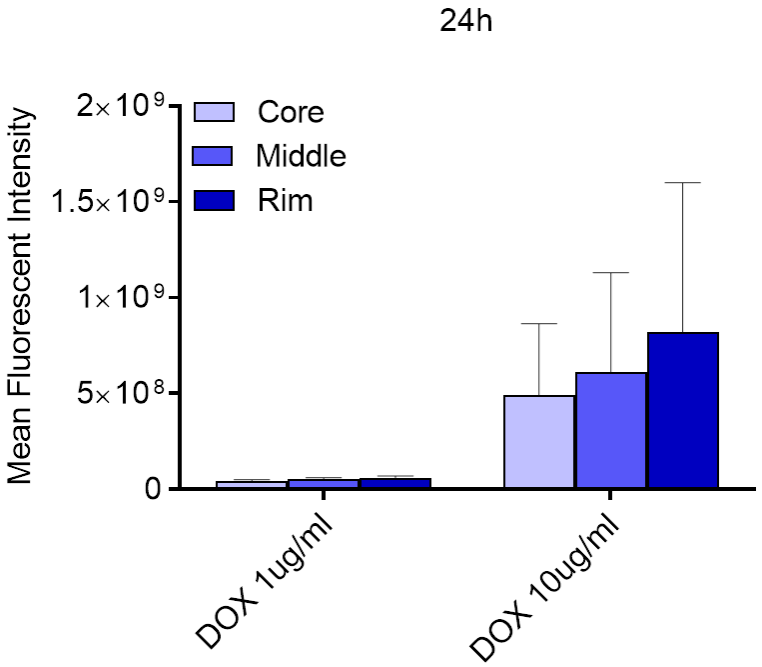


*Figure 17 Accumulation of Dox across HCT 116 spheroids. a-b) FACS dot plots representing accumulation of DOX across spheroids at 1 µg/ml and 10 µg/ml after 4h and 24h incubation. c) Uptake of free Dox across core, middle and rim in HCT 116 spheroids by MFI at 1 µg/ml and 10 µg/ml after 4h and d) after 24h incubation. ( ** display $p < 0.01$).*

In order to try to understand the above results in the clinical context, we have taken several aspects into consideration. The plasma mean concentration of free Dox in patients receiving a single intravenous dose is 0.2 mg/L after 1h, 0.1 mg/L after 4h after which it reaches a plateau and remains at this level until 24h. [118]

### 4.2.3 Cell uptake of Doxil after 2h incubation in HCT 116 monolayer cells.

To study the penetration of nano-delivery systems by FACS, they need to be taken up by the cell. The uptake of Doxil into HCT 116 monolayer cells was examined after 2 h incubation since this is the shortest time point used for the study of penetration into spheroids. Different concentrations were employed (10, 25, 50, 75 and 125 µg/ml) which represent the concentration of free Dox incorporated in the liposomal formulation. No fluorescence was detected at lower concentrations (50 µg/ml). An increase in fluorescence in the cells was observed with an increased concentration of Doxil (Figure 18).The results showed weak fluorescence signal at a concentration of 50 µg/ml fluorescent which became stronger at 75µg/ml and 150 µg/ml. Therefore, the concentration of 75 µg/ml was used for further experiments via FACS.

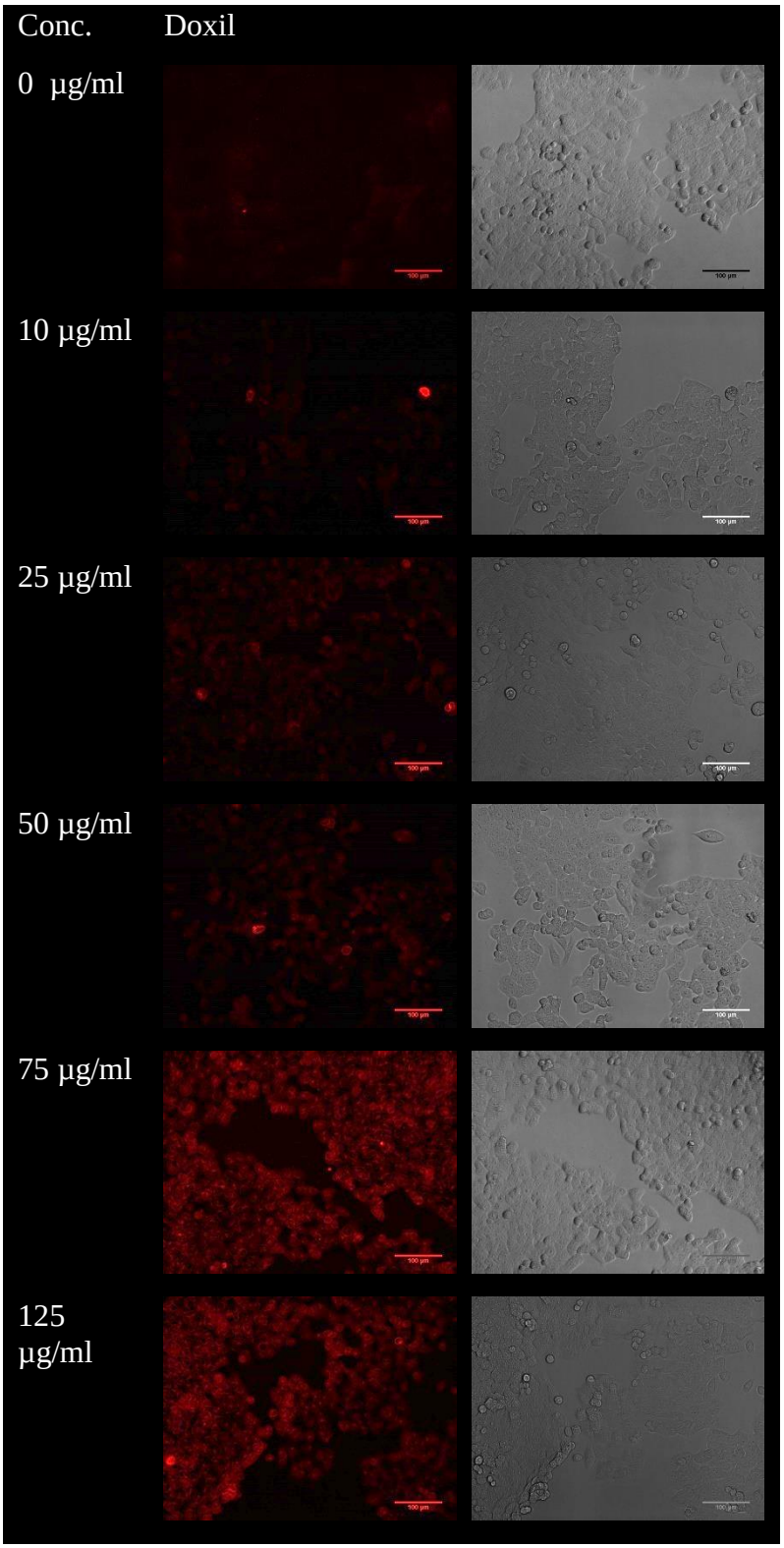


*Figure 18 Fluorescence images of HCT 116 monolayer cells incubated with different concentrations of Doxil (10, 25, 50, 75 and 125 µg/ml) for 2h.*

### 4.2.4 Penetration and uptake of Doxil in HCT 116 spheroids.

Penetration and uptake of a liposomal formulation of Dox (Doxil) have been evaluated for the ability to deliver Dox through the colorectal spheroids. The penetration profile of Dox via this nanoformulation was found to be time-dependent (Figure 19a). The diffusion of Doxil in the HCT 116 spheroid was very slow, and less than 10% of cells had Dox associated with them after 2 h incubation. Doxil reached 50% of cells after 6h and 85% after 24h incubation.

19a

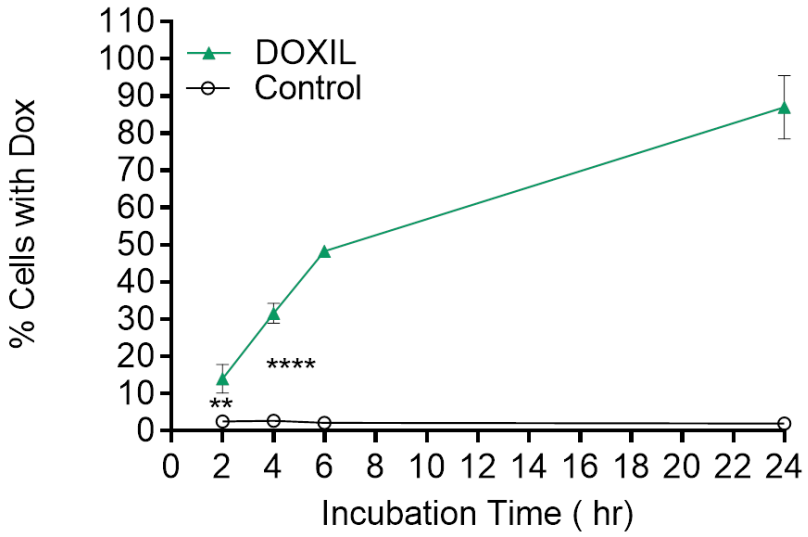

19b

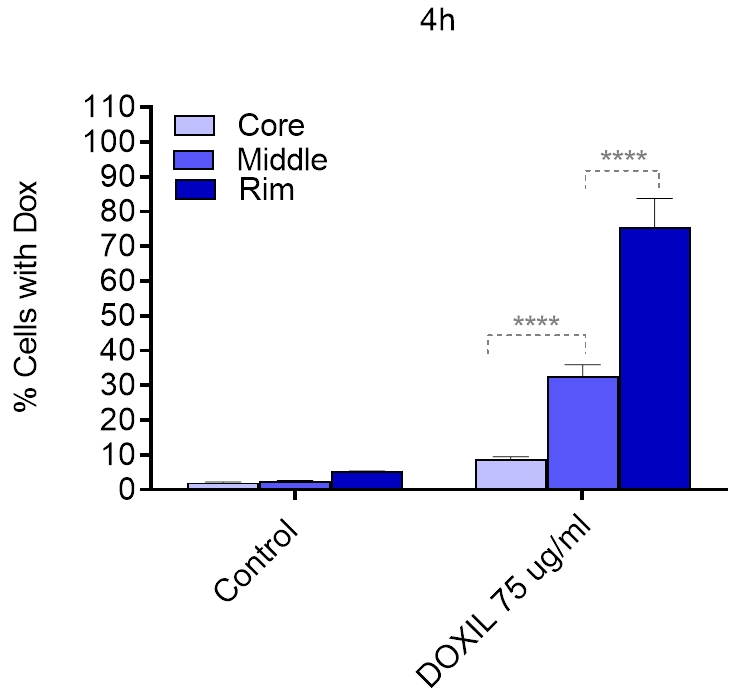


19c

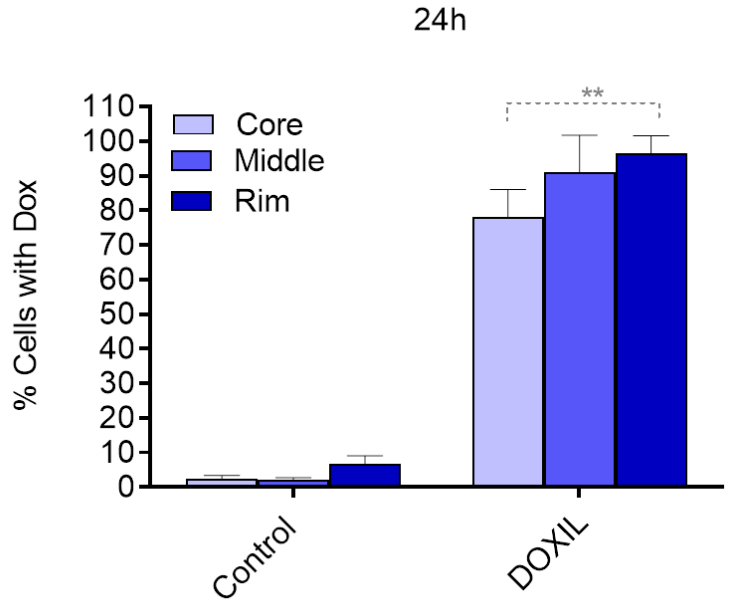


*Figure 19 Penetration of DOXIL in HCT 116 spheroids over time. a) Time-dependent penetration of Doxil (75ug/ml of free Doxorubicin) in HCT 116 spheroids by FACS. b),c) % cells reached by Doxil across different regions in spheroids after 4h and 24h incubation time. (****, ** display $p < 0.0001$, $p < 0.01$).*

a)

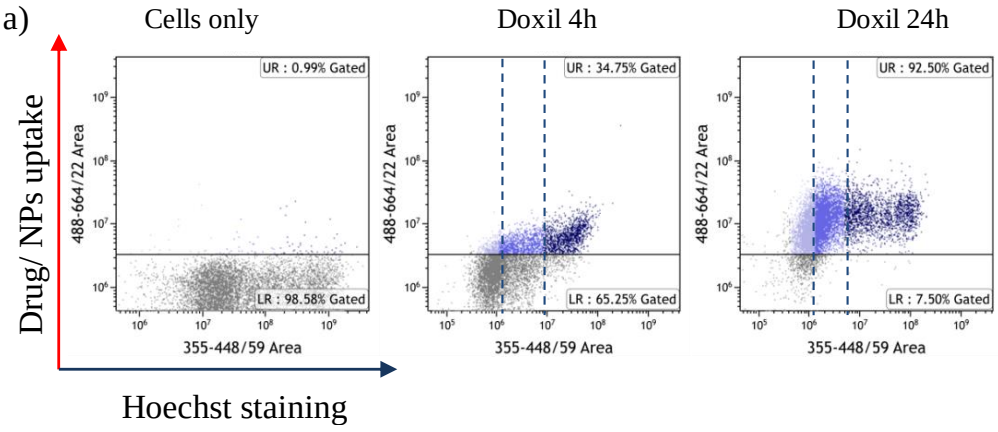
Cells only
Doxil 4h
Doxil 24h
Drug/ NPs uptake
Hoechst staining
488-664/22 Area
355-448/59 Area
UR : 0.99% Gated
LR : 98.58% Gated
UR : 34.75% Gated
LR : 65.25% Gated
UR : 92.50% Gated
LR : 7.50% Gated

b)

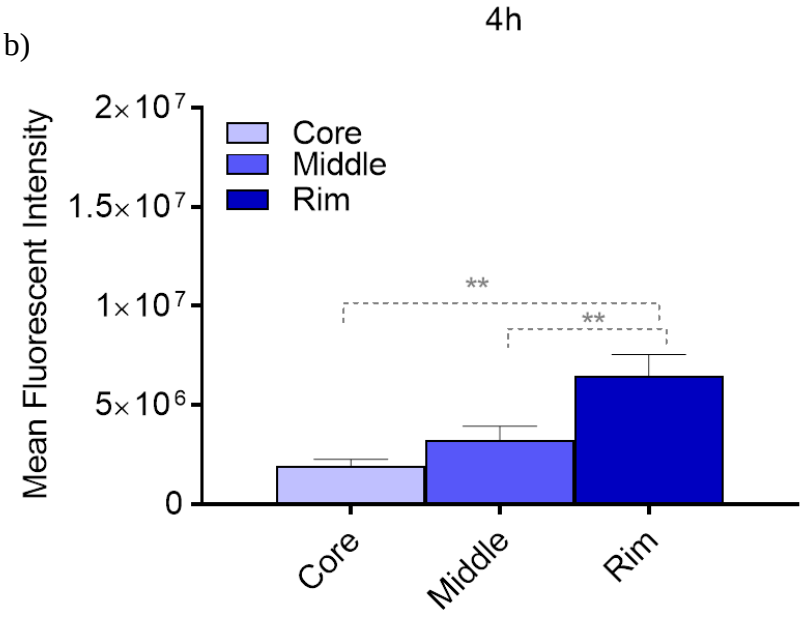
4h
Mean Fluorescent Intensity
2×10⁷
1.5×10⁷
1×10⁷
5×10⁶
0
Core
Middle
Rim
**
**
Core
Middle
Rim

c)

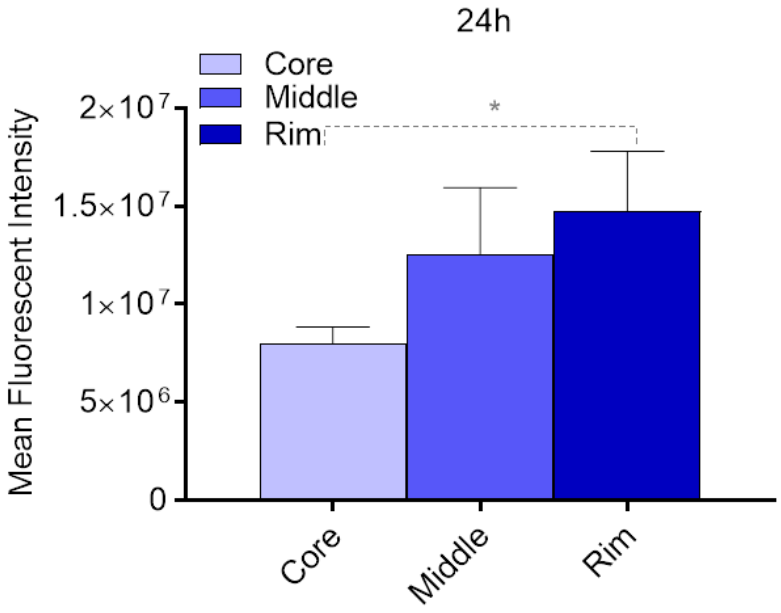


*Figure 20 Accumulation of Doxil (75ug/ml of free Doxorubicin) across HCT 116 spheroids. a. FACS dot plots representing accumulation of Doxil across spheroids at 4h and 24h. b. Uptake of Doxil across core, middle rim in HCT 116 spheroids by MFI. ( **, and * display $p < 0.01$, and $p < 0.05$, respectively).*

a)

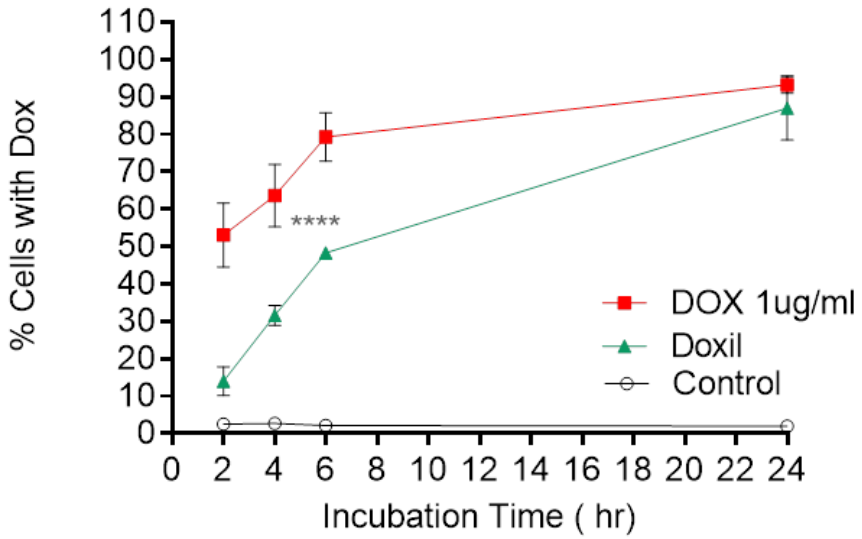


b)

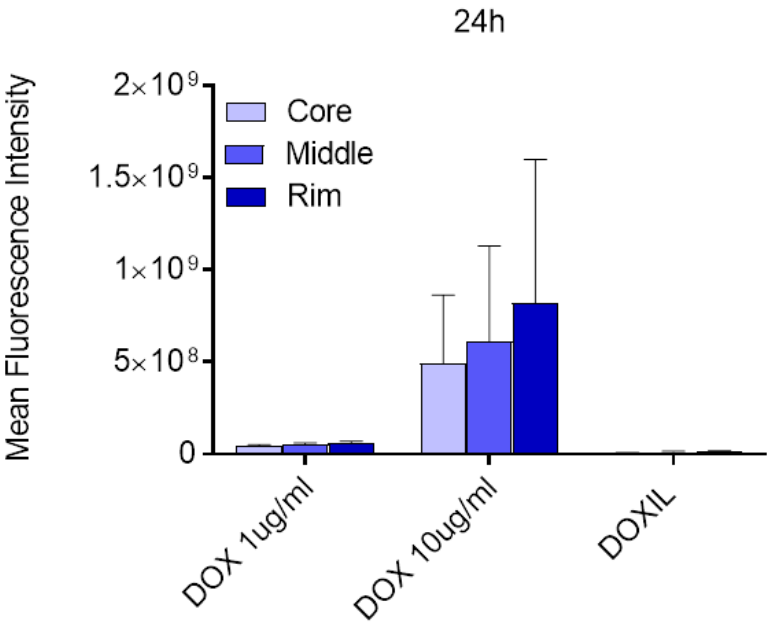


*Figure 21 Comparison of penetration and accumulation behaviour between DOX (1µg/ml) and Doxil (75 µg/ml of free Dox) in HCT 116 spheroids. a) Time dependent penetration of free Dox and Doxil. b) Level of accumulation of Dox vs. Doxil across core, middle and rim of HCT 116 spheroids. (****display $p < 0.0001$).*

The distribution and accumulation of Dox from Doxil in the cells across spheroid was observed to be higher at the periphery of spheroid than in the middle or core of spheroids at the early time points figure 19 b, c and 20 a, b. Higher uptake with more even accumulation across all regions of spheroid was detected after 24h, as presented in FACS dot plots and quantified in figure 20c.

In figure 21, differences in penetration and accumulation kinetics are presented between free Dox and Doxil. Significantly faster penetration of the drug into the core of spheroid was achieved with free Dox (Figure 21 a) than with Doxil, as well as much higher accumulation (figure 21 b.) after the 24h incubation period.

## 4.3 Discussion

In the study, flow cytometry method in combination with Hoechst was optimised and successfully employed for quantitative analysis of penetration and distribution of Dox and Doxil in HCT 116 spheroids. The results indicate that penetration of these systems is time and concentration dependent in HCT 116 spheroids. Further, it was found that distribution and accumulation profile of the anticancer drug in the spheroid was not improved by Doxil system even after 24h incubation.

For the anticancer therapy to be effective, it must be able to access all the cells in a tumour. However, limited tissue penetration of anticancer drugs has often been observed, and it presents a substantial barrier to their effectiveness.

Tumour interstitial space consists of various components including ECM and tightly packed cells that together can form a delivery barrier for macromolecules.[63] It has been proposed that rate of diffusion of macromolecules is proportional to molecular weight and size. [46,143] However, the contribution of other factors such drug metabolism, and binding to the tissue has also been demonstrated. [137] The penetration of drugs has also been shown to be affected by consumption such as metabolism, binding to tissue elements as well as uptake and retention by cancer cells.[1]

For the study, HCT 116 spheroids on day 3 of growth when their average radius falls around 220 µm were employed. The distances between the microvessels in a tumour are much greater than that seen in the normal tissue, reaching 15-20 cell diameters from the nearest blood vessel which can measure up to 200 µm.[144,145] Therefore, the spheroid model recapitulates the avascular distances seen in a tumour *in vivo*. An optimised flow cytometry method in combination with Hoechst was applied for direct and quantitative analysis of penetration and distribution of Dox and Doxil agents in the defined spheroid model.

The results indicate that penetration of Dox is time and concentration dependent in HCT 116 spheroids. The plasma mean concentration of free Dox in patients receiving a single intravenous dose is 0.2 mg/L after 1h, 0.1 mg/L after 4h after which it reaches a plateau and remains at this level until 24h. Thus in the study, the lower concentration of the free Dox (1 µg/ml) is representative of the situation *in vivo*. The higher concentration was included in the experiments to investigate the effect of drug concentration on penetration

into spheroids. The higher concentration of 10 µg/ml would require an unfeasibly large dose of the drug to be given.[118] The results have shown that at 1µg/ml, the free drug diffused into spheroid slowly over time, accessing only 50 % of all cells in the spheroid after 4h incubation. At a given dose the drug needed 24h to reach all the cells >90% within the spheroid. However, when a much higher dose of the free Dox was applied, the drug has reached all the cells in the spheroids > 90% significantly faster, 4h. The accumulation of the drug in the cells across core, middle and rim of spheroid was also significantly higher, as seen in Figure 20.

Dox has good drug characteristics, such that it is sufficiently hydrophilic for dissolution and binding to it molecular targets in an aqueous cell milieu, but sufficiently hydrophobic to partition and diffuse across cell membranes (Figure 22). It also has a positively charged amino sugar and is a substrate for p-glycoprotein. The journey of a Dox through the interstitial space is, therefore, a combination of diffusion and interaction with the ECM as well as uptake of drug into cells and its intracellular distribution, metabolism and binding. [137] Dox agent exerts its action by binding avidly to DNA. Thus, as Dox diffuses through tissue, it gets taken up by cells and strongly binds to DNA in the nucleus. It is consumed by the cells as it passes through the spheroid.

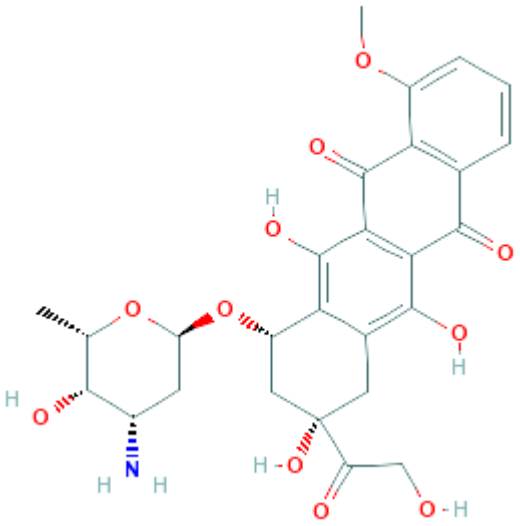

$C_{27}H_{29}NO_{11}$ Mw= 543.525 g/mol

*Figure 22 Dox chemical and physical properties.*

Therefore, when a low concentration of a drug is provided, cell uptake will reduce the concentration in ECF leading to a slower diffusion through the spheroid due to a reduction in the concentration difference, but give a high intracellular drug concentration at the rim. This highlights the importance of consumption in limiting drug penetration and drug availability.

The results showed that when a higher concentration of Dox is given, it reaches cells in the middle of spheroids much faster, which may be due to saturation of intracellular binding sites at the rim and increasing the availability of drug molecules to diffuse to more distant segments in the core. The results thus suggest that drug concentration is more important than the incubation time

since the accumulation of Dox 10 µg/ ml at 2h is the same as that of 1 µg/ ml at 24h.

In the study only Dox was investigated as an example of small drug molecules; however, we have seen similar behaviour in the case of Hoechst dye which has similar cell penetration and DNA binding properties.

Different studies have investigated many other common anticancer drugs such as cisplatin, etoposide, 5-FU, vinblastine, gemcitabine and paclitaxel and also showed their limited penetration and poor effectiveness. [137,80] Other studies that investigated Dox saw similar results in spheroids and tumours [1] however, these often lacked detailed analysis. Some found relatively rapid penetration and homogeneous distribution of Dox within 1 h with an accumulation plateau reached at 3 h in multicellular slices. This could be due to potential artefacts of their technique or much higher drug concentration used for the study. [137]

The results imply that in highly avascular tumours, where large distances are present between the blood vessels, Dox given at clinically relevant dose would not be able to gain sufficient access to all the cells in a tumour for a full therapeutic effect. One way to overcome this issue would be to increase a given dose; however, this is often not feasible due to the toxic side effects to healthy tissue. Another way to overcome such hurdle would be to use an improved formulation which can increase the drug availability at the tumour site. The liposomal formulation of Dox has been developed for that purpose. Doxil was the first FDA approved liposomal formulation for cancer treatment. However, the drug levels in a tumour *in vivo* have not been significantly improved, and the therapeutic outcome was found to be disappointing.[118]

Here, the delivery behaviour of Doxil in the tumour matrix was investigated. Again, the penetration of Dox through the matrix will be dependent on the route is taken through the spheroid, which could include passage through the ECM or endocytosis into cells.

As seen by the results, this liposomal formulation did not improve the penetration or distribution of the free Dox in HCT 116 spheroids. In fact, the penetration of Dox became significantly slower, and the amount of drug found in cells was lower than when the free drug was added despite much higher initial dose (Figure 21.) This agrees with a general belief that small therapeutics of size, up to a few nanometers, can diffuse fairly rapidly in the tumour interstitial matrix while penetration of larger systems such as nanoparticles or liposomes is hindered due to their large size. [46,143]

It needs to be noted, that while studying the penetration of Doxil, the fluorescence of the free Dox-loaded in the liposome shell was followed as a marker. Therefore, one cannot be certain whether the penetration of the liposome-doxorubicin complex or the free Dox was observed after it has been released from the liposome. Thus, the observed results could be either due to slow release of free Dox or slow diffusion of the liposome as expected due to the much larger size of the liposome compared to the drug molecule, but it could be a combination of both. However, regardless of the mechanism of action by Doxil system, it is clear that distribution and availability of Dox in the cells were not improved by this formulation in colorectal cancer spheroid during the 24h period.[20]

To date, the mechanism of Doxil penetration abilities, cell uptake and drug release in a tumour remain poorly understood.[146] Some studies suggested that liposome penetrate easily throughout an interstitial tumour space, while others claim that they accumulate at the tumour site and remain there, releasing the drug which then is available for diffusion through a tumour. [147] And others that Doxil penetrates to the interstitial space but does not get into cells, it releases free Dox in the interstitial space which then gets taken up. [146] The *in vitro* drug release rate from the Doxil has t1/2 of 118 h+/- 18h thus if the latter two cases are true then the slow release from the formulation could be the limiting step. [148] From the results of penetration kinetics of free Dox, it can be deduced that concentration is more important than the time the tumour is exposed to a drug. Doxil is believed to deliver more drugs to the tumour site due to increasing time in circulation as well as selective accumulation at a tumour. However, even if a higher drug concentration is provided at the tumour site, but liposome does not penetrate into the interstitial space, by releasing the drug slowly over time, there is a possibility that uneven distribution will be achieved as observed in the case of free Dox at 1 µg/ml. This could lead to a limited number of cells killed after a single drug administration which implies that slow regimes may not be beneficial for tumour diffusion and homogenous distribution.

Factors such as physicochemical properties of drugs which include molecular weight, charge, aqueous solubility and shape may also affect penetration through the interstitial space. Further, limited distribution of free Dox has also been found to be associated with efflux by the P-gp pump and has not been

investigated herein. The p-gp pump is believed to cause multidrug resistance by reducing drug uptake into cells and tissue. However, some studies showed that this is overcome when a high concentration of Dox is given due to saturation of the P-gp pump allowing for cell uptake and subsequent cell apoptosis. [80,149–151] Lastly, while this study was performed in HCT 116 colorectal cancer spheroids, it needs to be considered that the results may be different when another type of cell line is used.

To quantify the penetration and uptake of anticancer drugs, flow cytometry analysis was performed. The flow cytometry technique allows for highly sensitive detection of as few as 5–10 NPs per cell.[152] Furthermore, it allows studying up to thousands of cells per second. The Hoechst 33342 dye allowed for quantitative analysis of the distribution of Dox and Doxil in spheroids. At the chosen concentration the dye stained cells at the periphery of spheroid to a greater extent than the cells within the core of spheroid. The study showed that the 3D spheroid model together with FACS/ Hoechst method provides a promising *in vitro* screening method for assessing nanoparticles in the early stage of the development process.

The limitations of FACS/Hoechst method for studying the penetration and distribution of drugs/ NPs is that these systems must be fluorescent. Secondly, the system must be up-taken by the cells. A further limitation is that the method does not account for any drug systems present in the spaces between the cells. However, since these systems are not taken up by the cells, they do not exert their therapeutic effect hence the information is of lower importance. A further consideration is that Hoechst staining must be optimized for each

different cell model as it is more likely to be affected by the spheroid geometry. Additionally, the spheroids must be dissociated into a single cell suspension; however, despite that, the method was found to be highly sensitive and robust when comparing to other methods used for the detection of nanoparticles within the core of spheroids such as cryo-sectioning, microscopy or sequential trypsinisation. [139,142,153]

## 4.4 Conclusions

The aim of the study was to develop an understanding of the penetration capabilities of small drug molecules and nanoformulations. To give this some relevance, a clinically useful drug was included for comparison. To carry out this study, the FACS/Hoechst method was adopted and developed for evaluating the penetration of Dox and Doxil *in vitro*. The results showed that diffusion of Dox was concentration and time-dependent with a limited number of cells reached by a drug at a clinically relevant dose. It was also evident that by employing liposomal formulation of Dox the distribution and accumulation of the drug were significantly slower than that of the free Dox. These findings highlight that tissue penetration of drugs and nanocarriers is challenging thus should not be underestimated in the development of new anticancer treatments and should be tested and optimised in the early phase of their development. Knowledge of drug's penetration kinetics allows establishing the concentration of a drug necessary to exert a maximum effect. It is also evident that new formulations are needed with improved penetration capabilities to overcome

the hurdle caused by the tumour microenvironment and successfully deliver a therapeutic drug to all cancer cells. Improved drug penetration would mean reduced drug levels required to reach all the cells in a tumour thereby reducing systemic toxicity.[52]

# Chapter 5 Evaluation of penetration and uptake of model Polystyrene nanoparticles in HCT 116 spheroids

## 5.1 Introduction

There has been great interest in using nanodelivery systems in order to deliver anticancer drugs into tumours as they offer advantages over a free drug treatment such as selective accumulation at the tumour site, enhanced efficacy and reduced toxicity. Various nanosystems are being developed; however, many examples in the literature have demonstrated their non-uniform distribution which can often lead to poor accumulation and uptake lowering the effectiveness of the treatments.[48,49,52,154,155]

Although there is increasing evidence indicating that the physiochemical properties of NPs such as size, charge and surface chemistry play a crucial role in their ability to penetrate through the ECM, the effect of these physicochemical properties on penetration and uptake in representative tumour models has not been examined in detail.

In the present study, the effects of both the size and surface characteristics of polystyrene NPs on the penetration and cellular uptake into tumours were examined. The aim was to identify the features that promote penetration of the nanosystems into tumour tissues, which is crucial to aid development and design of NPs with characteristics that will permit them to effectively penetrate and become uniformly distributed within the tumour tissues thereby improving therapeutic performance.

## 5.2 Results:

### 5.2.1 Characterisation of Nanoparticles

To examine the effect of size and surface chemistry of NPs on trafficking into spheroids, polystyrene nanoparticles were employed as model particles as they are available in a range of different sizes and surface characteristics thereby allowing for comparative study. The surface charge of nanoparticles was assessed by performing size measurements via Zetasizer nano in DI water and in RPMI-1640 medium with 10% FBS. (Table 4.) The measurements in the latter represented the behaviour of NPs under experimental conditions as the media was used for all the subsequent penetration and uptake studies.

*Table 4 Size of Polystyrene NPs in different media.*

| **Table 4.** | | | | |
|---|---|---|---|---|
| **Media** | **DI Water** | | **RPMI-1640 +FBS** | |
| **NPs** | **Size (nm)** | **PDI** | **Size (nm)** | **PDI** |
| **NPs 30 nm** | 33±0.1 | 0.08±0.01 | 70± 1.7 | 0.28 ±0.01 |
| **NPs 50 nm** | 56±0.6 | 0.06±0.02 | 84± 0.6 | 0.17 ±0.01 |
| **NPs 50 nm COOH** | 52±0.7 | 0.14±0.01 | 75± 0.7 | 0.20±0.01 |
| **NPs 50 nm $NH_2$** | 52±0.6 | 0.06±0.00 | 209±4.0 | 0.40±0.02 |
| **NPs 100 nm** | 107±1.9 | 0.02±0.01 | 165±1.9 | 0.14±0.01 |

| **Table 5.** | | |
|---|---|---|
| **Medium** | **10 mM HEPES** | **RPMI-1640** |
| **NPs 30 nm** | -27±1.4 | -9± 0.8 |
| **NPs 50 nm** | -32±0.3 | -6± 0.7 |
| **NPs 50 nm COOH** | -32±2.6 | -9± 0.8 |
| **NPs 50 nm NH2** | 24±1.5 | -7± 0.4 |
| **NPs 100 nm** | -39±2.1 | -8± 0.1 |

*Table 5 Zeta Potential of Polystyrene NPs in different media*

The measurements performed in RPMI-1640 medium with 10% FBS showed an increase in mean diameter for unmodified, aminated and carboxylated particles when compared to the results obtained in DI water, suggesting the adsorption of serum proteins and other components of the medium to their surface. The increase in the size of 50 nm aminated nanoparticles was significantly higher indicating possible aggregation of these nanoparticles under experimental conditions.

The Zeta potential of the polystyrene NPs was measured in 10 mM HEPES buffer, and RPMI-1640 media supplemented with FBS and was media dependent, Table 5. The nanoparticles showed strong positive zeta potential for aminated polystyrene NPs and strong negative surface charges for both carboxylated and unmodified polystyrene NPs in HEPES buffer. The strong charges relate to the surface functional groups of these NPs -NH2 and -COOH

for aminated and carboxylated nanoparticles, respectively. The negative zeta potential of unmodified nanoparticles arises from the sulphated groups located on the particle surface resulting from their polymerization reaction. The surface density of these groups, however, is much lower than in the case of modified, carboxylated nanoparticles. In the RPMI-1640 medium with the addition of 10% FBS, the surface charge of all types of nanoparticles became slightly negative regardless of their original charge which further implies the adsorption of serum proteins to their surface.

### 5.2.2 Fluorescence difference between Polystyrene NPs .

The levels of fluorescence per different sizes polystyrene nanosystems were provided by the manufacture and are shown in Figure 23. The fluorescence levels varied considerably between NPs. The largest, 100 nm NPS were the brightest of all systems followed by 50 nm aminated, 50 nm, 50 nm carboxylated and 30 nm NPs. This highlights the importance of normalising data when studying tumour/cell uptake based on the fluorescence levels of NPS. In the penetration experiments, the difference in MFI between the data was normalised by designating 50 nm NPS sample as equal to 1 and applying that adjustment factor to remaining NPS by use of ratiometric results.

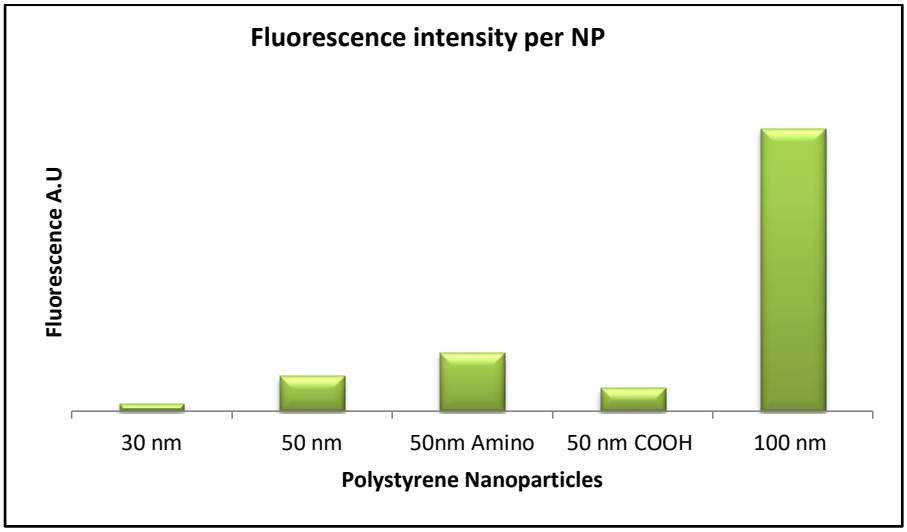


*Figure 23 Fluorescence levels per Polystyrene NP (30 nm, 50 nm, 50 nm aminated, 50 nm carboxylated, 100 nm).*

### 5.2.3 Concentration-dependent uptake of polystyrene NPs in HCT 116 monolayer cells

Uptake of polystyrene NPs into HCT 116 monolayer cells after 2h incubation time was assessed by fluorescent microscopy, Figure 24. Varying concentrations of 10-125 µg/ml were employed to find intermediate concentration at which all the different NPs gets taken up into cells over a suitable range for detection by microscopy and FACS. An increase in fluorescence was observed with the increase in concentration. Higher uptake for 30 nm, 50 nm unmodified and 50 nm aminated nanoparticles was observed than 50 nm carboxylated and 100 nm unmodified nanoparticles. At 75 µg/ml, all NPs were detected at a high level in the cells; therefore, this concentration was employed for the penetration study in spheroids.

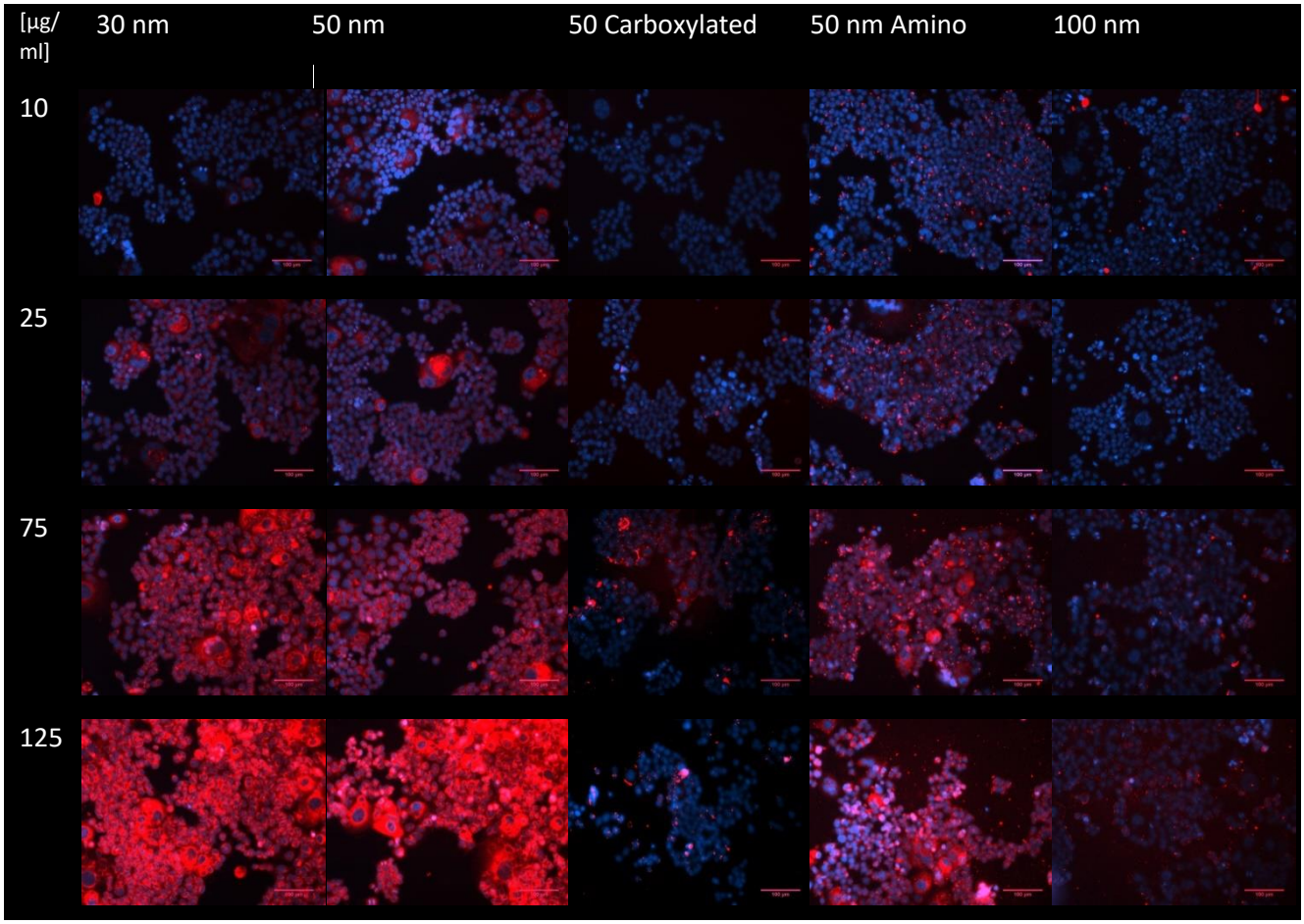


*Figure 24 Concentration-dependent cellular uptake of Polystyrene NPs (30 nm,50 nm, 50 nm aminated, 50 nm carboxylated, 100 nm) in HCT 116 cells. HCT 116 monolayer cells were exposed to different concentrations of polystyrene nanoparticles for 2 hours and imaged by fluorescence microscopy. Red= nanoparticles, blue=DAPI (nucleus). Scale bar 100 µm*

### 5.2.4 Cytotoxicity of Polystyrene NPS in HCT 116 cells

Based on the knowledge from the literature, the polystyrene NPS are not expected to be toxic to cells.[156] Some studies showed that functionalised polystyrene NPs with amino groups might lead to cell toxicity, however at much higher levels and exposure times than those used in our study.[156–158] This was further confirmed throughout the study, during the periodical inspections of the HCT 116 cells via microscope whch showed cell morphology was not affected after 24h incubation with 75 µg/ml aminated nanoparticles.

### 5.2.5 Effect of nanoparticle size on penetration and distribution in spheroids

The effect of the size of nanoparticles on the penetration into HCT 116 spheroids was evaluated by incubation of spheroids with 30 nm, 50 nm and 100 nm unmodified polystyrene particles. The size-dependent penetration and localisation of NPs are qualitatively displayed by confocal images of 20 µm spheroid sections in Figure 25a and quantified by FACS/Hoechst method in figure 25b.

The results show that small 30 nm NPs and 50 nm NPs reached over 70% and 80 % cells, respectively within the first 2 h hours of incubation. Both reached > 90 % of cells in the spheroid after a 6 h incubation. However, in the case of larger 100 nm nanoparticles, a different penetration profile was observed. Less than 10 % of cells contained 100 nm NPs after 2 h incubation which further increased to just 22% of cells after 24 h incubation. (Figure 25b).

Further, 30 nm and 50 nm nanoparticles were distributed evenly between the different cell population segments based on Hoechst staining with ~ 80% of cells in the core segment of the spheroids taking up dye (Figure 26 and 27 a and b) the 100 nm NPs were strongly associated with the periphery of spheroids with no significant penetration achieved in the core of spheroids even after the 24 h incubation period. The results obtained by FACS correlate well with the results obtained by confocal imaging.

Further, the level of nanoparticle accumulation in the spheroids was investigated. The difference in MFI between the data was normalised by designating 50 nm NPS sample as equal to 1 and applying that adjustment factor to remaining NPs by use of ratiometric results. Figure 28a shows the MFI achieved by 30 nm and 50 nm NPs in spheroids after 4 h incubation times. The plot shows a similar accumulation profile of the 30 nm and 50 nm systems, with slightly higher cell uptake achieved by 30 nm NPs. No significant difference in concentrations achieved between the core, middle and periphery of spheroid was observed.

In Figure 28b the accumulation profile for these NPs is presented after 24h incubation. It can be noted that while the MFI levels of 50 nm NPs remain similar to the ones observed after 4h incubation, the MFI of 30 nm increased considerably. This suggests that 50 nm NPs reached maximum accumulation in cells across spheroid after 4h incubation while 30 nm NPs continued to accumulate in cells over a 24h period. The MFI levels of 100 nm NPs were not investigated since these NPs do not penetrate far enough to accumulate in cells

located deeper in spheroid. Uniform uptake was observed for 30 nm and 50 nm NPs across core, middle and periphery of spheroid after 24 h.

a)

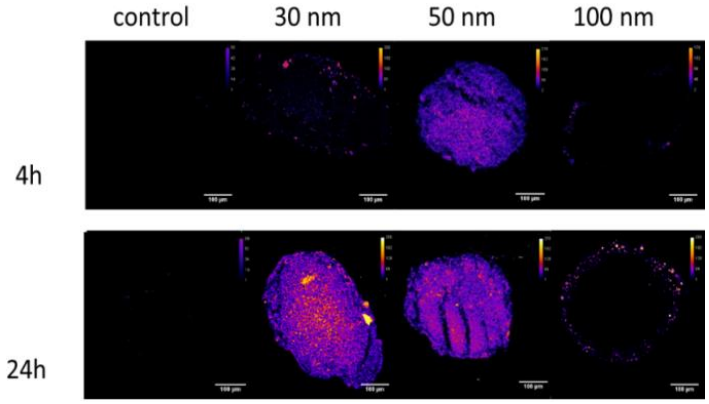


b)

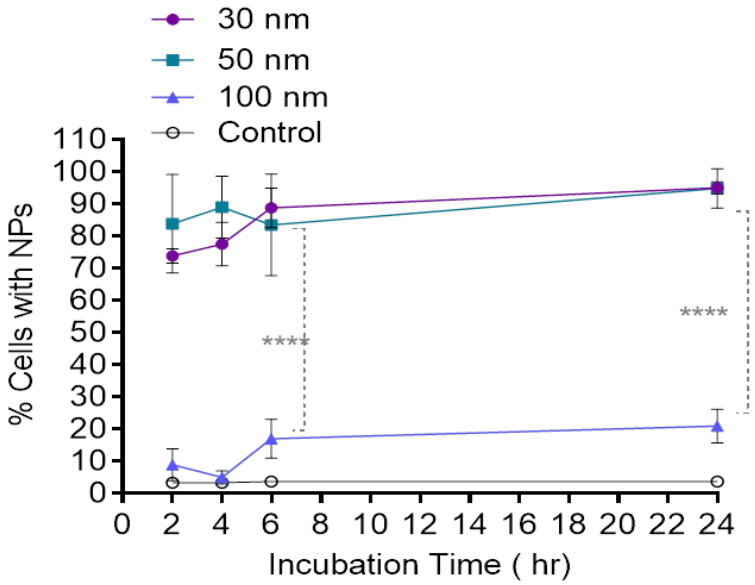


*Figure 25 Size-dependent penetration of Polystyrene NPs (30 nm,50 nm,100 nm) into HCT 116 spheroids. a) Confocal images of frozen sections (section s= 20 µm) of HCT 116 spheroids incubated with 30 nm, 50 nm and 100 nm unmodified polystyrene nanoparticles (75 µg/ml). Scale bar 100 µm. Images processed by applying LUT fire in Image J software. b) Time-dependent penetration of NPs in spheroids by FACS/Hoechst method. (****, indicates $p < 0.0001$).*

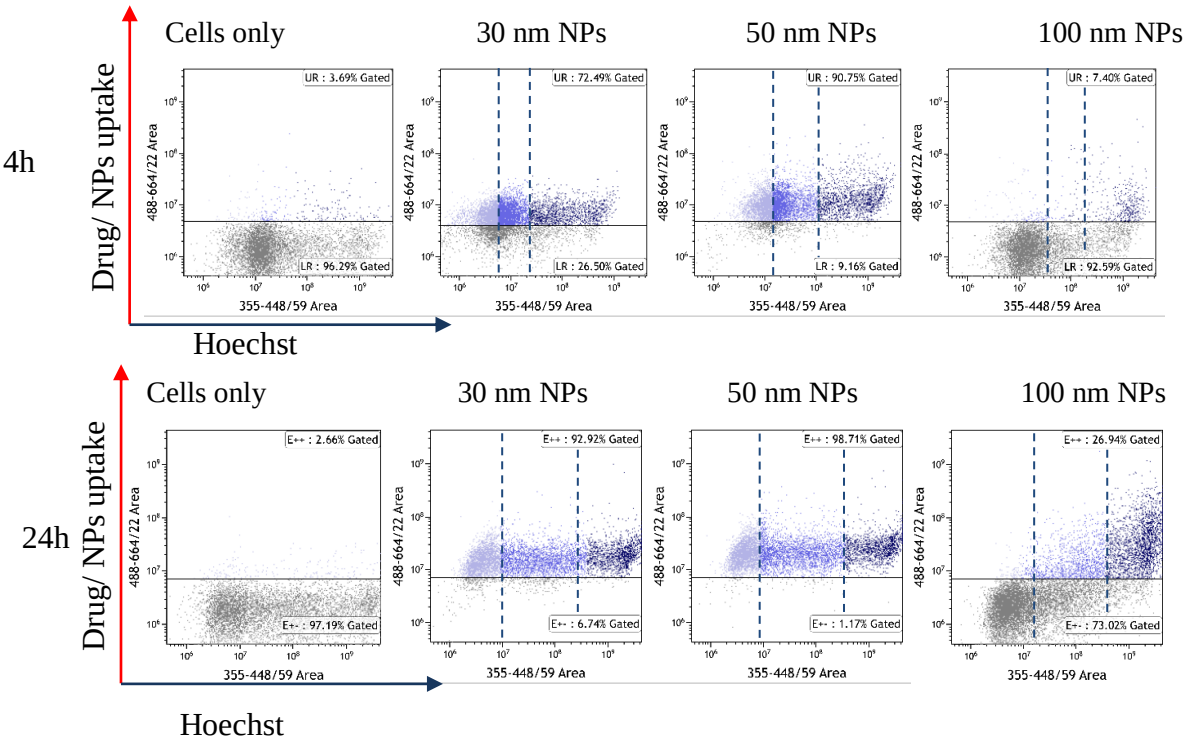


*Figure 26 Size-dependent penetration of Polystyrene NPs (30 nm,50 nm,100 nm) into HCT 116 spheroids. Distribution of Polystyrene NPs (30 nm,50 nm,100 nm) across HCT 116 spheroids after 4h and 24h shown by FACS dot plots.*

a)

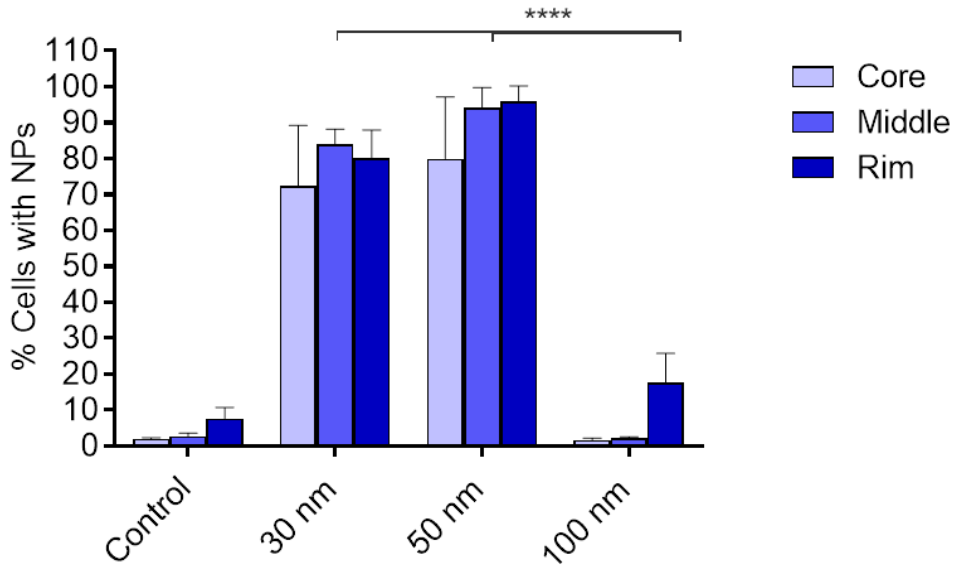


b)

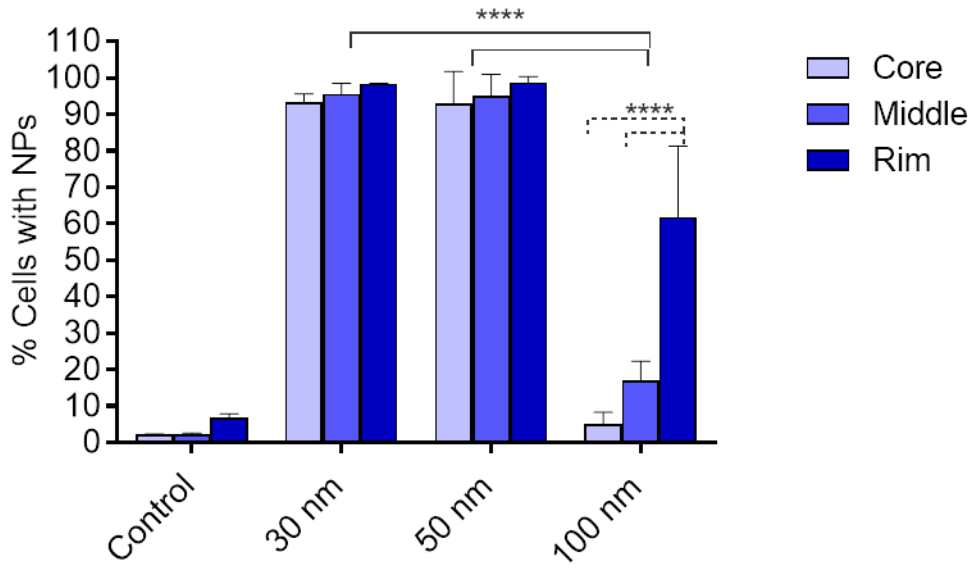


*Figure 27 Size-dependent penetration of Polystyrene NPs (30 nm,50 nm,100 nm) into HCT 116 spheroids. a) Distribution of Polystyrene NPs (30 nm,50 nm,100 nm )in HCT 116 spheroids 4h. b) Distribution of Polystyrene NPs (30 nm,50 nm,100 nm ) in HCT 116 spheroids 24h. (**** display p < 0.0001, respectively).*

a)

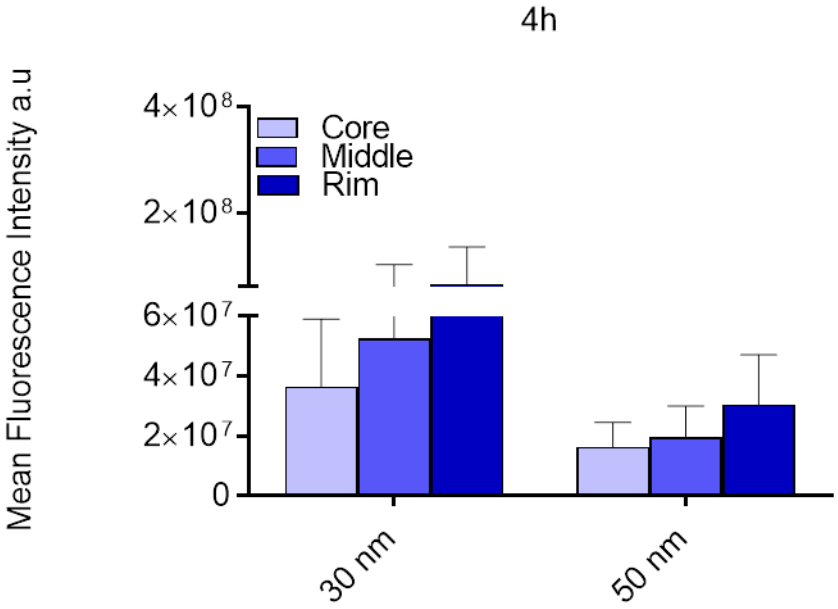


b)

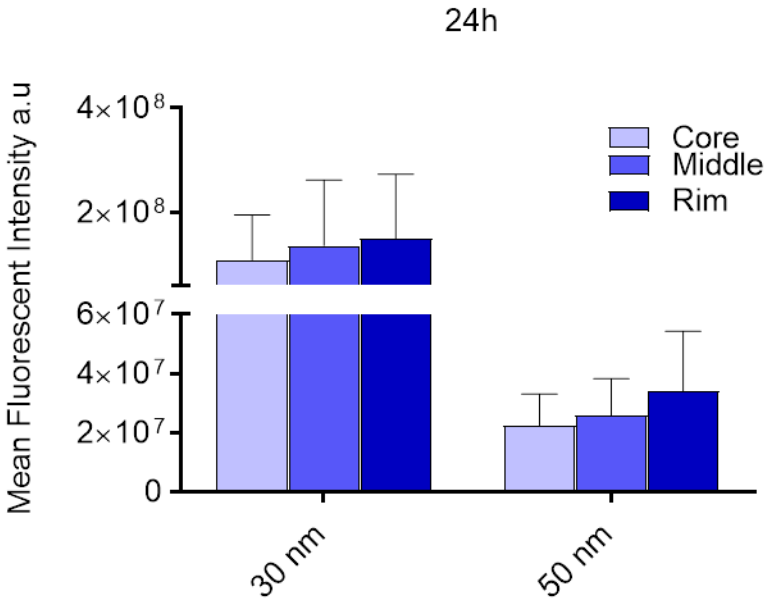


*Figure 28 Size-dependent penetration of Polystyrene NPs (30 nm, 50 nm ) into HCT 116 spheroids. a) Accumulation of nanoparticles in HCT 116 spheroids measured by the mean fluorescence intensity of nanoparticles after 4h incubation. b) Accumulation of nanoparticles in HCT 116 spheroids measured by the mean fluorescence intensity of nanoparticles after 24h incubation. (* displays $p < 0.05$.)*

### 5.2.6 Effect of the surface charge of NPs on penetration and distribution in spheroids.

In the next stage the effect of nanoparticles with the same size of 50 nm but different surface charges were investigated; slightly negative unmodified NPs, positive aminated and negative carboxylated polystyrene nanoparticles on their ability to penetrate through spheroids. When comparing these systems, marked effects of these modifications on penetration were observed. In the results by confocal microscopy, only 50 nm unmodified NPs were detectable within the core after 4 h incubation while aminated 50 nm NPs showed preferential association with the periphery of spheroids. The 50 nm carboxylated nanoparticles were not detected at this stage by confocal microscopy. FACS confirmed that 50 nm unmodified nanoparticles achieved significantly faster and higher penetration, 2 fold higher than 50 nm aminated NPs and 8 fold higher than 50 nm carboxylated NPs into HCT 116 spheroids after 4 h incubation (Figure 29a, b).

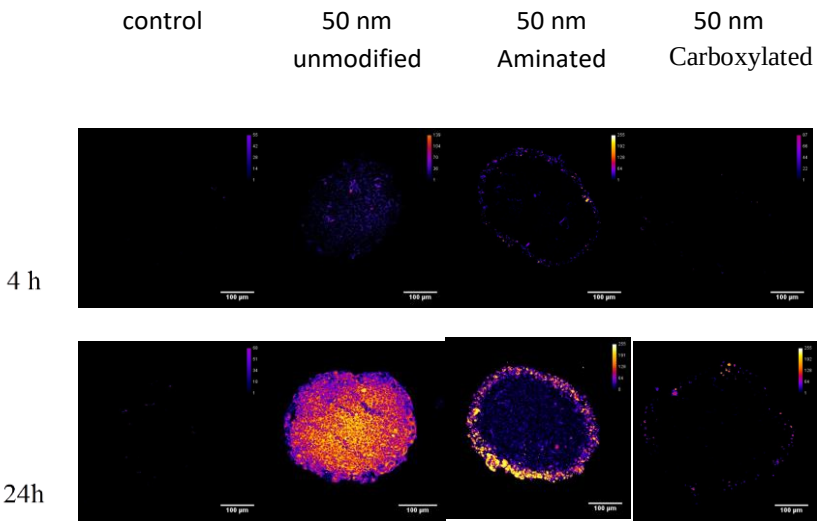


b)

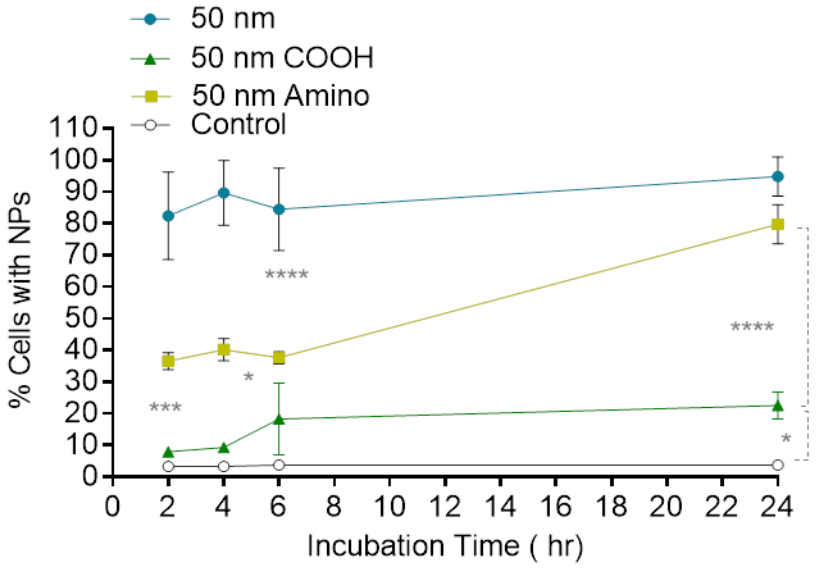


*Figure 29 a) Surface-dependent penetration of Polystyrene NPs (50 nm unmodified, 50 nm, aminated, 50 nm carboxylated) into HCT 116 spheroids. Confocal images of frozen sections (sections = 20 µm) of HCT 116 spheroids incubated with 50 nm unmodified, aminated and carboxylated polystyrene nanoparticles. Images processed by applying LUT fire based on the fluorescent intensity in Image J software. b) Time-dependent penetration of 50 nm and 50 nm Amino and 50 nm Carboxylated NPs in spheroids. (**** represents p-value < 0.001).*

The penetration of 50 nm aminated NPs was found to be much slower and more time-dependent. The % of cell uptake remained at < 40% until 6h incubation. The % cells with detectable levels of NPs continued to increase reaching ~80% cells after 24h. Despite the overall high percentage of cell association of 50 nm aminated nanoparticles after 24h, the distribution profile reveals significantly lower penetration (<70%) into the core of the spheroid compared to the outer layers after 24h incubation. (Figure 30 and 31a, b). The 50 nm carboxylated nanoparticles were restricted to the rim of spheroids only, with low total cell uptake of 20% after 24 h and inefficient penetration abilities into the core of spheroid (Figure 30 and 31a, b)

The amount of cell uptake after 4h incubation revealed low NPs uptake in the core and middle section of 50 nm aminated NPs with much higher levels accumulated in cells at the rim (Figure 32 a). After 24h incubation (Figure 32b) an increase in uptake of aminated NPs into cells in the core and middle section of spheroids was observed suggesting these NPs continued to penetrate and accumulate in the spheroid over time. The amount of cell uptake in these regions was comparable to the levels of 50 nm unmodified NPs. However, much higher levels of aminated nanoparticles were observed at the periphery of the spheroid.

a)

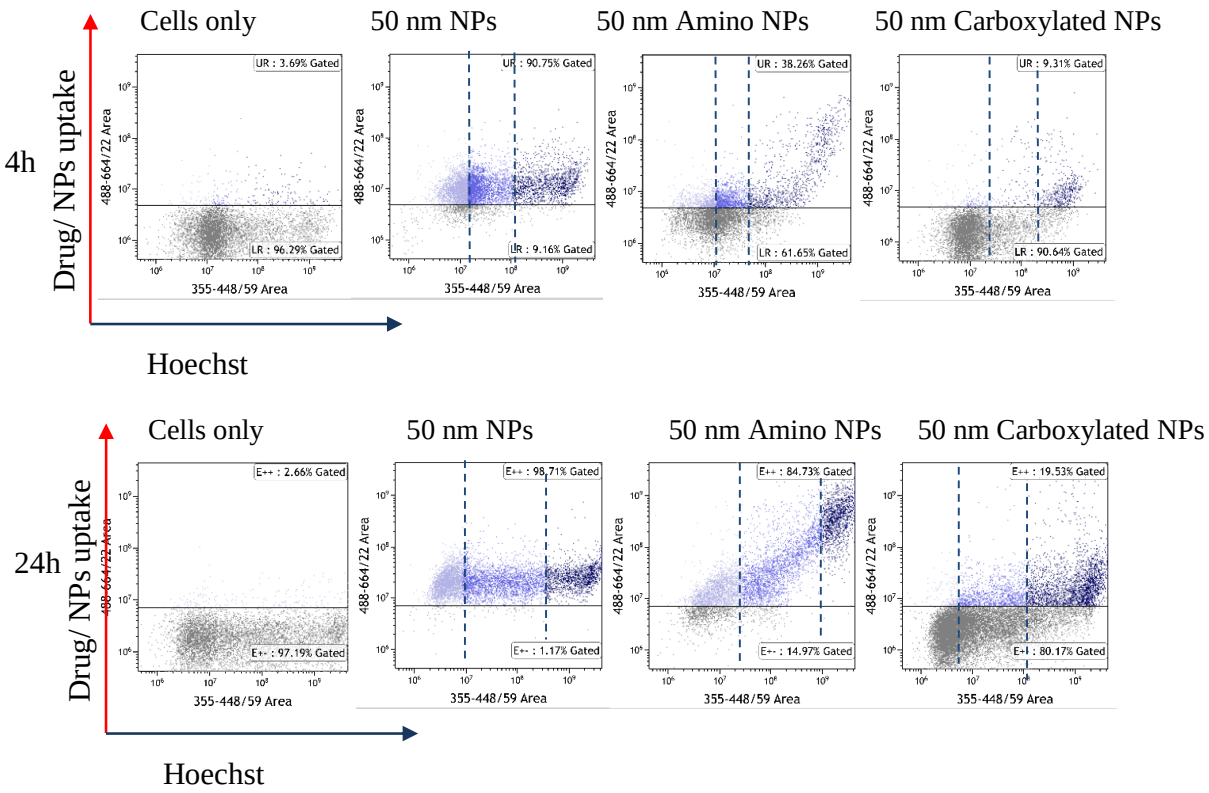


*Figure 30 Surface-dependent penetration Polystyrene NPs (50 nm unmodified, 50 nm, Aminated, 50 nm carboxylated) into HCT 116 spheroids. Distribution of Polystyrene NPs (50 nm unmodified, 50 nm, Aminated, 50 nm carboxylated) across HCT 116 spheroids after 4h and 24h shown by FACS dot plots.*

a)

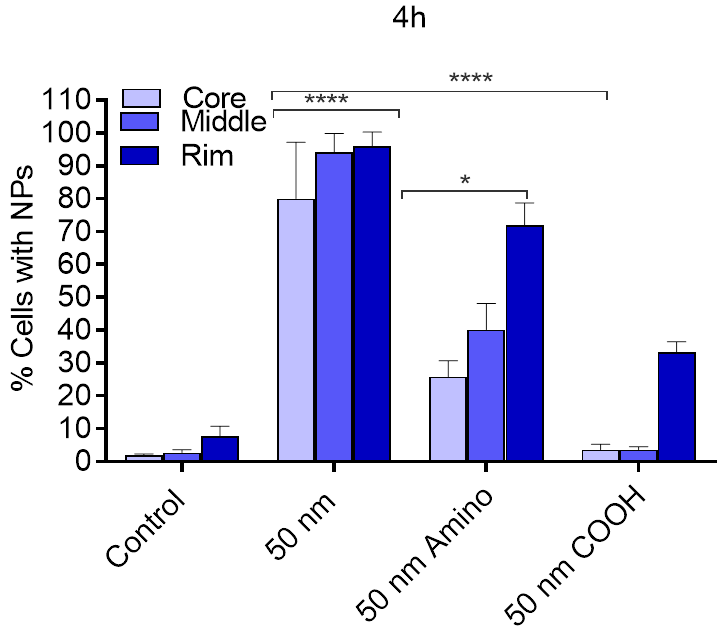


b)

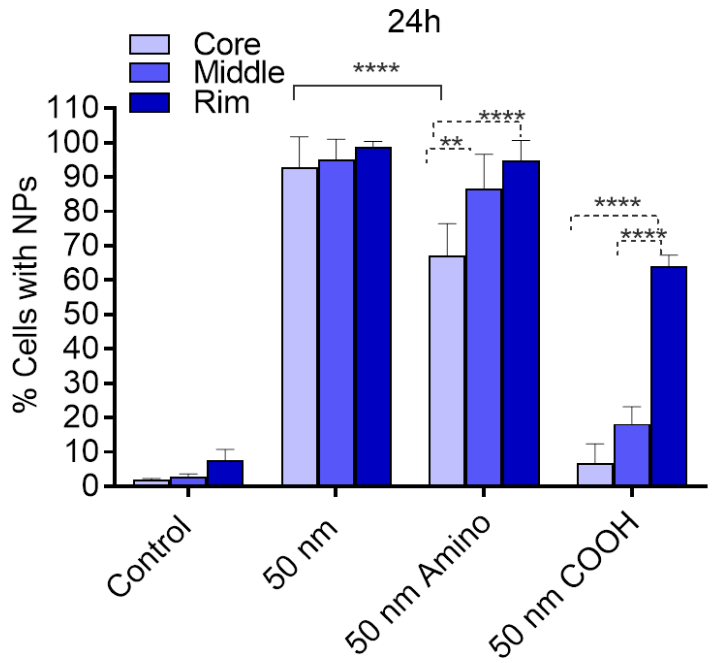


*Figure 31 Surface-dependent penetration of Polystyrene NPs (50 nm unmodified, 50 nm, Aminated, 50 nm carboxylated) into HCT 116 spheroids. a) Distribution of 50 nm unmodified, aminated and carboxylated NPs across core, middle and rim region of HCT 116 spheroids after 4h. b) Distribution of 50 nm unmodified, aminated and carboxylated NPs across core, middle and rim region of HCT 116 spheroids after 24h incubation. Measured by FACS/Hoechst method. (****, ** display $p < 0.0001$, $p < 0.01$,)*

a)

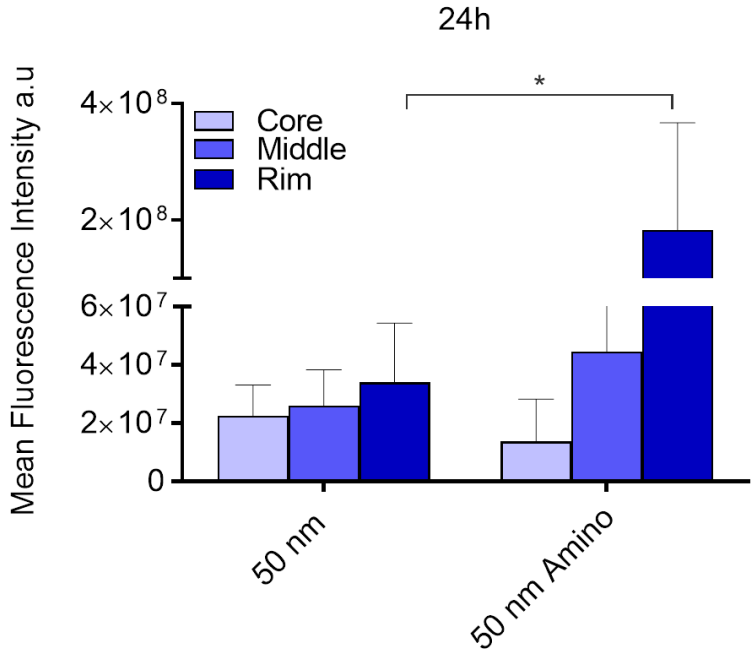


b)

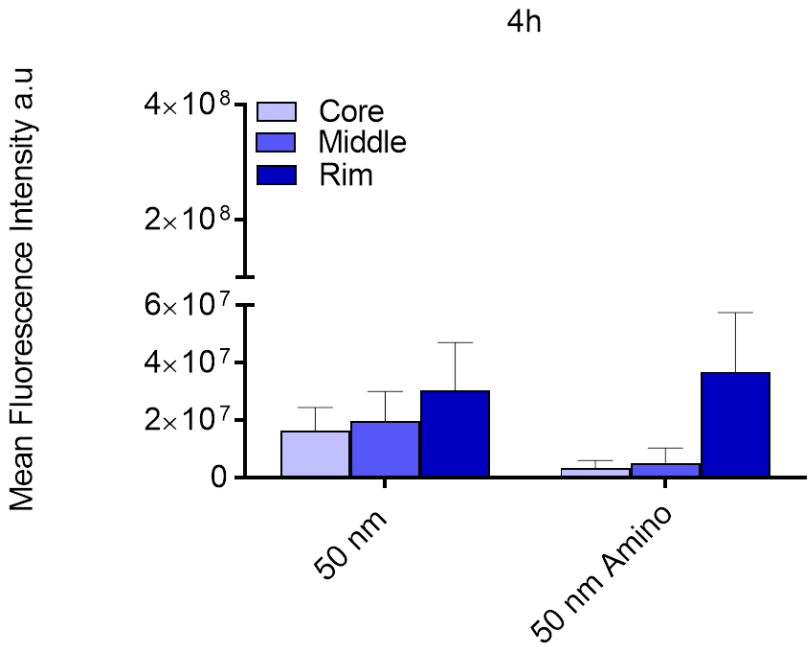


*Figure 32 Surface-dependent penetration of Polystyrene NPs (50 nm unmodified, 50 nm, Aminated) into HCT 116 spheroids. a) Accumulation of 50 nm unmodified, and aminated NPs across core, middle and rim regions of spheroids measured by the mean fluorescence intensity of nanoparticles after 4h incubation. b) Accumulation of 50 nm unmodified and aminated NPs across core, middle and rim region of spheroids measured by the mean fluorescence intensity of nanoparticles after 24h incubation. (****, ***, **, and * display $p < 0.0001$, $p < 0.001$, $p < 0.01$, and $p < 0.05$.)*

## 5.3 Discussion

Here, the effects of both size and surface characteristics of polystyrene nanoparticles on the penetration and cellular uptake *in vitro* in 3D spheroids were investigated. The results showed that smaller nanoparticles (30 nm and 50 nm) showed greater penetration and accumulation in the core of HCT 116 spheroids when compared to the larger (100 nm) nanoparticles. It was also observed that penetration of the smaller nanoparticles (50 nm) was strongly influenced by their surface characteristics.

The results are consistent with the outcomes of previous *in vivo* and *in vitro* studies. Tung *et al*. compared the penetration abilities of 50 nm and 200 nm camptothecin-silica nanoparticle conjugates in murine tumour models *in vivo* and *ex vivo* and found higher penetration, accumulation and internalisation of the 50 nm nanoparticles in comparison to 200 nm particles that localised at the surface of tumours only. [45] These results suggest that the extracellular space together with ECM matrix acts to filter nanoparticles by size. It has been suggested that smaller nanoparticles are capable of diffusing through pores between the collagen fibrils which have been measured to reach 20–40 nm in compact tumours and up to 75–130 nm in poorly organised tumours. [49] This theory has been supported by previous studies which found that improved penetration of several therapeutic systems in solid tumours was achieved after the disruption of the ECM by the use of protease enzymes, collagenase, hyaluronidase or drugs such as losartan. However, it is still not clear what the limiting factor to sufficient tumour accumulation is. For instance, a study done

by Huang et al. found that the maximum size for efficient penetration is approximately 15 nm for gold particles. Others also reported the difference in penetration capabilities between dendrimers with diameter 2 nm and 4 nm/ 7 nm with the smallest showing better penetration than the 7 nm particle.[159] On the other hand, our results, have demonstrated that particles up to 50 nm can successfully penetrate the tumour and are no different in penetration characteristics to 30nm NPs. [45,97,160]

This suggests that other mechanisms in addition to size play a crucial role in the penetration process of nanoparticles. Indeed, it was proposed that charged components of ECM restrict the diffusion of positively and negatively charged particles due to electrostatic attraction and binding. [136] Thus the influence of the surface charge of the nanoparticles with the same size of 50 nm but different chemical groups, unmodified and carboxylated nanoparticles with negative surface charges and aminated, positively charged nanoparticles was investigated. The results showed that penetration of these particles was strongly dependent on surface characteristics: whereas slightly negative unmodified 50 nm nanoparticles were capable of penetration into the centre of the spheroid (>200 μm depth), the carboxylated, negatively charged NPs were incapable of penetrating further than one cell diameter from the rim. This exclusion from entering the spheroids by carboxylated NPs is probably due to negative electrostatic repulsion from the –ve components of ECM towards the negatively charged surface of the both the spheroid and the cell surfaces. [134] In the study both unmodified and carboxylated nanoparticles had the same zeta potential in the HEPES buffer (-32 mV) and both became slightly negative -6

± 0.7 and -9 ± 0.8, respectively, in RPMI-1640 medium supplemented with FBS, conditions which were used for the studies. Despite similar characteristics shown by the zetasizer, the nanoparticles behaved very differently in the biological environment affecting their ability to penetrate and accumulate in the spheroids. This suggests that the type of the groups or perhaps charge density on the surface influence the way the nanoparticles interact with biological components. [159]

The aminated NPs achieved a higher uptake into cells than negative NPs, presumably due to interactions with negatively charged plasma membrane proteins on the cell surface.[30, 26] However, their penetration through the tumour tissue was slow and limited to the outer cell layers of a spheroid, ~30-50 μm depth. This may be partly due to a binding effect with the negatively charged ECM components which hindered further diffusion. However, because of the increased cellular uptake of these positively charged NPs both in 2D and at the periphery of 3D culture, it may be that the uptake of NPs into cells provides the larger barrier to penetration of these particles further into the spheroid in much the same way as a binding site barrier operates for antitumour antibodies. [161–163] These results suggest that these particles could deliver a high therapeutic dose to the most accessible cells, but that cells deeper within a tumour would receive subtherapeutic drug amounts.

Our study showed that smaller ~50 nm, near neutral NPs can penetrate easily into the core of spheroids thus systems with these characteristics would be a promising choice for cancer treatment.

While the present study gives us a good idea of the relative performance of different types of NPs, this is still a first step towards understanding how to develop useful delivery systems for tumours. Different tumours will have various combinations of host cells and tumour cells with different properties which are likely to affect both ECM and rates of endocytosis.

## 5.4 Conclusion:

Well-characterised HCT 116 spheroids were taken as a model to compare the penetration of polystyrene nanosystems with different physicochemical characteristics. The results showed that unmodified polystyrene NPs (30 nm/50 nm) were able to penetrate to the core of HCT 116 spheroids more efficiently than larger polystyrene NPs (100 nm). Further, penetration was also dependent on surface charge, while near neutral 50 nm NPs were able to penetrate freely into the core of spheroid, the negatively and positively charged 50 nm nanoparticles showed restricted diffusion.

The results highlight the need to control physicochemical features of nanoparticles such as size and surface charge when designing nanomedicines in order to achieve the best delivery of therapeutic agents into tumours.

# Chapter 6 Evaluation of penetration and uptake of experimental nanoparticles in HCT 116 spheroids

## 6.1 Introduction

An increasing number of nanosystems are being developed which vary considerably in their physicochemical properties. Although there is growing evidence indicating that the physiochemical properties of NPs such as size, charge and surface chemistry play a crucial role in their ability to penetrate through the ECM, the effect of these physicochemical properties on penetration and uptake in representative tumour models has not been examined systematically.

Developing such understanding is crucial to aid the design of nanocarriers capable of sufficient accumulation in a tumour to optimise therapeutic performance.

Herein experimental polymeric nanoparticles were employed based on poly (glycerol-adipate) (PGA) polymer (shown in Figure 33) which showed promise as a potential carrier of anticancer drugs.[99,102,] PGA polymer has been found highly attractive for applications in biomimetic, pharmaceutical and biomedical fields as it is enzymatically biodegradable to natural metabolites. It is typically produced from divinyl adipate, and unprotected glycerol is yielding polymers with an average molecular weight of 12 kDa. The PGA is amorphous, insoluble in water and contains free hydroxyl groups in its backbone which can be easily

modified by esterification reaction with fatty acids to generate systems with varying degree of lipophilicity or hydrophobicity. [34] These unique properties made this polymer more desirable than widely used PLA and PCL materials which, due to high hydrophobicity and crystallinity, provide a slow rate of hydrolysis/degradability.

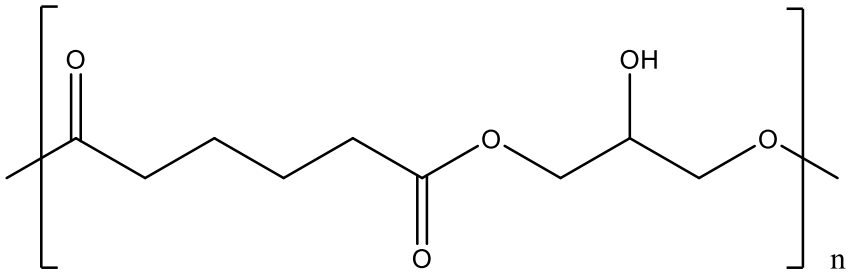


*Figure 33 Structure of poly(glycerol adipate backbone.*

PGA has been investigated for use in the production of NPs and showed it was capable of self-assembly into NPs and were very efficient at entrapping drugs of different polarity. [34,165] Further, it can be easily tuned to generate systems with improved drug loading and slow drug release. PGA thus offers opportunities for delivery of many drugs.

In this study, NPs from unsubstituted PGA polymer and PGA modified with C18 groups (stearoyl, $C_{18}$ chain), as well as PEG, were prepared and evaluated in colorectal cancer spheroids. By employing these systems, we aimed to answer important questions about how the changes to physicochemical properties of PGA such as increased hydrophobicity and rigidity will affect the

penetration kinetics and distribution of those NPs in spheroids. We also aimed to investigate how the addition of PEG group to their surface might influence the penetration, localization and uptake of these NPs.

## 6.2 Results

NPs were prepared from unmodified PGA, PGA substituted with a PEG group, PGA modified with C18 groups and PGA modified with C18 and a PEG groups via solvent displacement method. These NPs were loaded with Rhodamine B Isothiocyanate (RBITC) as a fluorescent marker. RBITC was chosen as previous research by our group showed it provided higher dye loading in comparison to other dye Rhodamine B (RB) as well as produced NPs of a more consistent size. The encapsulated RBITC, also reacts with the polymer terminal carboxyl groups to ensure that the label is not easily lost from the polymer. Detailed characterization of the polymers and NPs can be found in the references.[34,165]

### 6.2.1 Size and Zeta potential of PGAs Nanoparticles

Zetasizer Nano was used to measure the mean hydrodynamic diameter and polydispersity index (PDI) of the NPs in DI water and in the cell culture media (RPMI + 10% FBS). The results are shown in Table 6. The mean size of PGA and PGA –PEG NPs was 109 nm and 107 nm and for PGA-C18 and PGA –

C18-PEG NPs, 114 nm and 117 nm respectively when measured in DI water. The PDI was quite broad for unPEGylated NPS PGA and PGA-C18, 0.22 and 0.25 respectively; however when the system was PEGylated, much narrower PDI was achieved, 0.04 for PGA and 0.11 for PGA-C18 NPs. This is expected as PEGylation is known to facilitate the formation of more regular NPs with less aggregation. The mean size diameter, as well as PDI, increased when the measurements were performed in the cell culture media. The unsubstituted PGA NPs had the smallest mean size with 115 nm and PDI of 0.23 and PGA – C18 NPs showed the highest increase in size, with an average diameter of 154 nm and much higher PDI of 0.57, indicating possible aggregation or protein adsorption to the surface of these NPs. Both formulations substituted with PEG reached the size of 134 nm and PDI of 0.25-0.3 when measured in the cell culture media.

Zeta potential of nanoparticles is presented in Table 7. All formulations tested showed negative zeta potential, ranging between -30 to -35 mV when measured in HEPES buffer. However, when measurements were performed in RPMI media with FBS, the value dropped to ~ -10 mV for all formulations, confirming protein adsorption.

*Table 6 Size of PGA NPs in different media.*

| **Table 6.** | | | | |
|---|---|---|---|---|
| | DI water | | RPMI+FBS | |
| Sample | Z-Ave (d.nm) | PDI | Z-Ave (d.nm) | PDI |
| PGA | 109 | 0.22 | 115 | 0.23 |
| PGA- PEG | 107 | 0.04 | 134 | 0.30 |
| PGA- C18 | 114 | 0.25 | 154 | 0.57 |
| PGA-C18-PEG | 117 | 0.11 | 134 | 0.25 |

*Table 7 Zeta Potential of PGA NPs in different media.*

| **Table 7.** | | |
|---|---|---|
| | HEPES | RPMI+FBS |
| Sample | ZP (mV) | ZP (mV) |
| PGA | -30 | -12 |
| PGA- PEG | -30 | -10 |
| PGA- C18 | -35 | -10 |
| PGA-C18-PEG | -32 | -12 |

### 6.2.2 Cytotoxicity of PGAs NPS in HCT 116 cells

Cytotoxicity of the NPs in HCT- 116 monolayer culture was assessed after 24 incubation, Figure 34. The 24h time point was chosen as it was representative of the longest time point used in the penetration/ uptake study by flow cytometry. HCT 116 cells were incubated with varying concentration of NPs (10 – 125 µg/ml); Alamar Blue was used to assess toxicity to cells. All the formulations were found nontoxic to the HCT 116 cells after a 24h incubation period at concentrations up to 125 µg/ml.

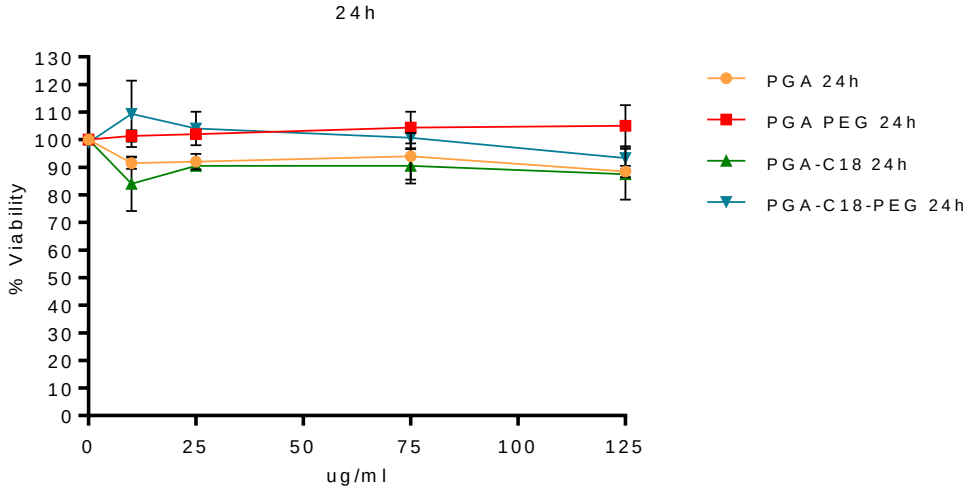


*Figure 34 Cytotoxicity of PGA nanoparticles (PGA, PGA- PEG, PGA -C18, PGA-C18-PEG) in HCT 116 monolayer cells after 24h incubation with different concentrations (10 – 125 µg/ml) of PGA NPs.*

### 6.2.3 Fluorescence difference between PGA formulations.

Levels of RBITC fluorescence per PGA system were analysed using a fluorometer Figure 35. The result showed that despite an equal amount of RBITC utilized in the preparation of these systems, the fluorescence levels varied considerably between NPs. The PGA-PEG was the brightest of all systems followed by PGA NPS which had a slightly lower level of fluorescence. The fluorescence levels of PGA-C18-PEG and PGA–C18 however, were considerably lower (1.5 and 2.7 fold difference) highlighting the importance of normalising data when studying cell uptake based on the fluorescence levels of NPs.

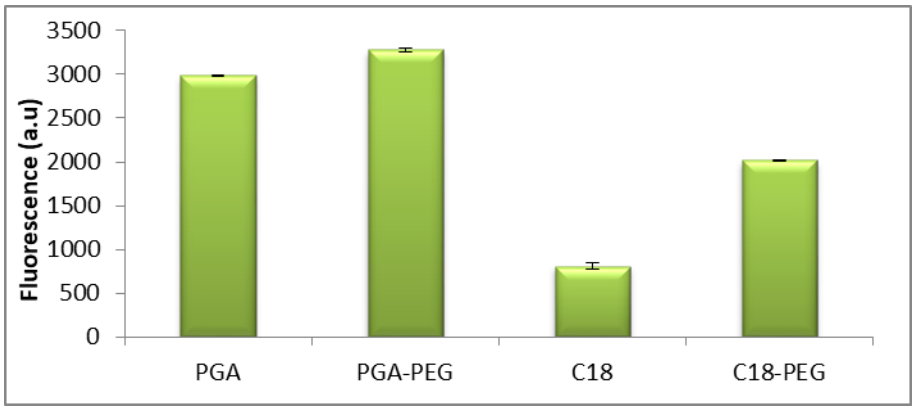


*Figure 35 Fluorescence levels per PGAs nanoparticles (PGA, PGA- PEG, PGA -C18, PGA- C18-PEG) at 75 µg/ ml measured by a fluorometer.*

### 6.2.4 Concentration-dependent uptake of NPs in HCT 116 monolayer cells

Cell uptake of NPs after 2h incubation time in HCT- 116 monolayer cells was assessed by fluorescence microscopy (Figure 36). Different NPS concentrations varying from 10 -125 µg/ ml were employed to evaluate whether all formulations could be detected in the HCT 116 cells after 2h incubation which represents the shortest incubation time used in the penetration study. As seen in Figure 36, the fluorescence in the cells became brighter with an increase of NPs concentration. Further, the fluorescence levels of PGA–C18–PEG NPs appeared much higher at a concentration of 25 µg/ml when compared to other systems which were not yet visible within the cells. This indicates these NPs have a greater ability to accumulate in the HCT 116 cells than other formulation tested. At a higher concentration (75 µg / ml), however, the fluorescence of all the NPs was detected in the cells, and it became even brighter at 125 µg/ ml. The concentration of 75 µg/ml was chosen for the penetration study in 3D spheroids since this concentration provided sufficient fluorescence for detection of all four formulations at 2 h incubation. At a higher concentration (125 µg/ ml) the cells seemed to be overloaded with fluorescence. Furthermore, it should be noted a different appearance of PGA and PGA–PEG NPs across the cells in comparison with PGA-C18 and PGA-C18-PEG. In the images of the former, distinct spots of the high level of fluorescence can be observed close to the nucleus; however, the fluorescence seems to diffuse more evenly across the cytoplasm of the cells in the case of the latter NPs. This may indicate the different route of uptake of NPs and/ or

different localization of these NPs in HCT 116 cells; however, this needs further evaluation.

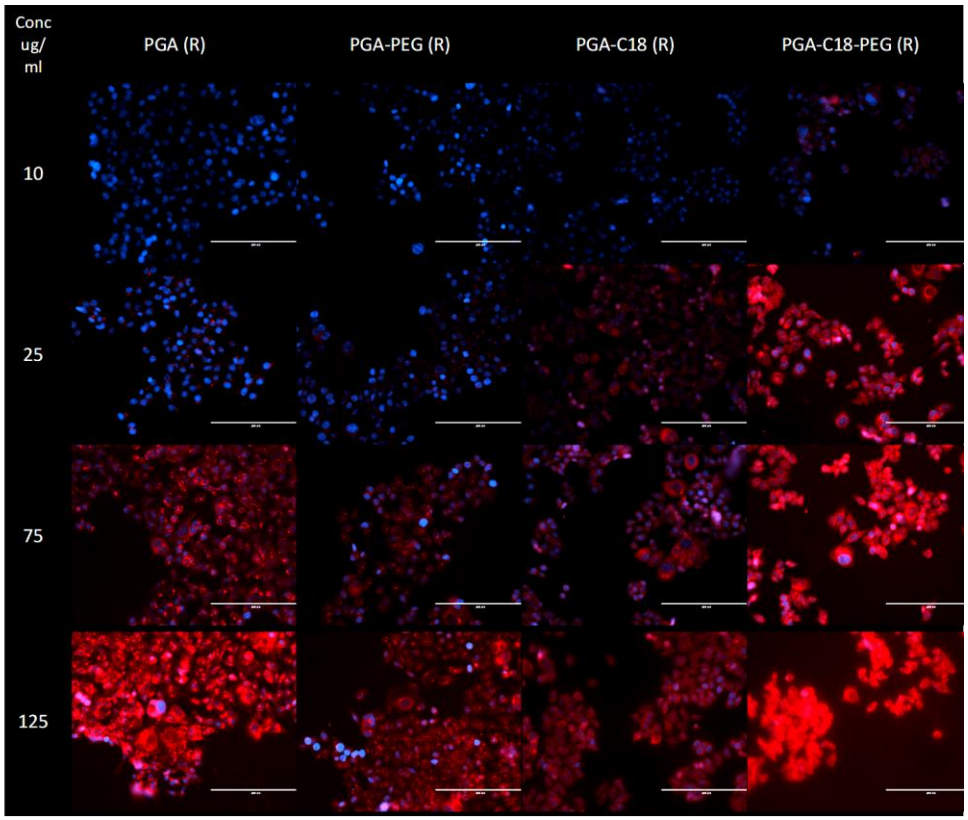


*Figure 36 Concentration-dependent cellular uptake of PGA, PGA- PEG, PGA -C18, PGA- C18-PEG nanoparticles in HCT 116 cells. Fluorescence images of HCT 116 monolayer cells exposed to different concentrations of PGA, PGA-PEG, PGA-C18 and PGA-C18-PEG nanoparticles for 2 hours. Red= NPs, blue=DAPI (nucleus). Scale bar 100 µm.;*

### 6.2.5 Time-dependent penetration of NPs in HCT 116 spheroids

Penetration abilities of all PGA systems were investigated with time over 24 h periods using FACS/Hoechst method. Fluorescence of NPs was from the RBITC dye. Previous research from our lab investigated the contribution of

free RBITC to the results from PGA NPs study and showed that the contribution of RBITC to the overall MFI was very low and accounted for 1% of overall intracellular fluorescence intensity, therefore assuring the MFI detected was from RBITC labelled NPs.[117]

Fast penetration of unmodified PGA NPs was observed with 80% cell association detected after 2h incubation. The cell association further increased to 90% after 4h and NPs reached all the cells in spheroids (~100%) after 6h incubation. In comparison, PGA-C18 NPs reached only 30% of all cells after 2h incubation after that the percentage of cell uptake increased slowly over time until it reached 60% of cells after 6h incubation and ~90 % of cells after 24h incubation. The results indicate that substitution of the PGA system with C18 group significantly slowed the penetration abilities of these NPs. Further, the addition of a PEG group to both PGA and PGA-C18 systems on their penetration kinetics was evaluated. As presented in Figure 37 the penetration profile of PGA-PEG NPs does not differ from the profile of unsubstituted PGA NPs. The modification of the PGA-C18 NPs with the PEG group, however, lead to significant improvement in the penetration (>3 fold increase) of these NPs. The PEGylated PGA-C18 NPs exhibited the same penetration profile as the unmodified PGA or PEGylated PGA NPs.

Further, the distribution and accumulation of all PGA formulations across rim, middle and core regions of HCT 116 spheroids were studied. Figures 38 a, b and c show the percentage of cell association with NPs in different regions of spheroids after 4h and 24h period. While PGA, PGA-PEG and PGA-C18-PEG reached ~90% cells in the core of spheroids after 4h incubation, the PGA-C18

reached less than 20 % cells in the core. Further, this formulation only reached 40% of the cells in the middle part of spheroids. Figure 38e also shows that accumulation across spheroid was uneven after shorter incubation time (4h), for all these systems. Despite reaching all the cells in the core of spheroid, a lower level of fluorescence in the core than at the periphery of spheroids was observed.

Figure 38d and f, reveals that all NPs continued to accumulate over a period of 24h, and achieved more uniform distribution and significantly higher uptake

across the core, middle and rim of the spheroid. After 24h incubation, PGA-C18 NPs also reached > 90 % of cells in the core of spheroid. It should also be noted that the cellular uptake of PEGylated PGA-C18 NPs was much higher across the spheroid in comparison with all other PGA nanoparticles after 4h and 24h incubation.

a)

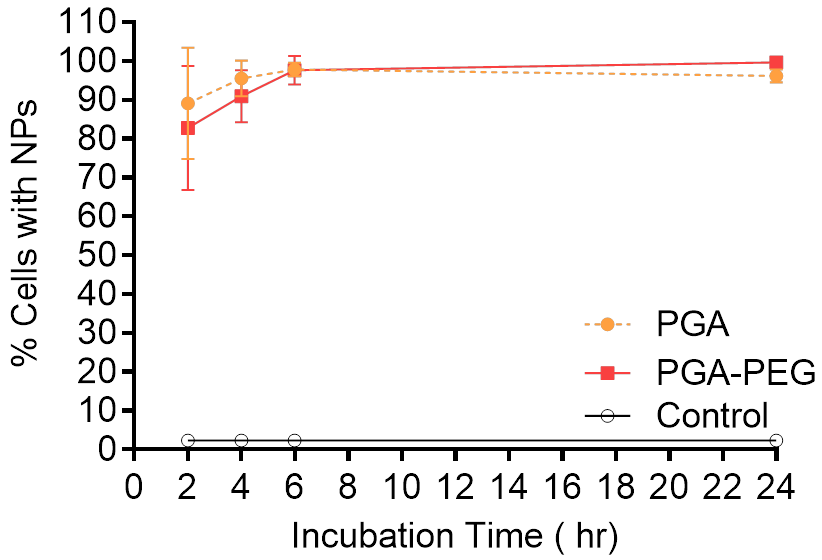


b)

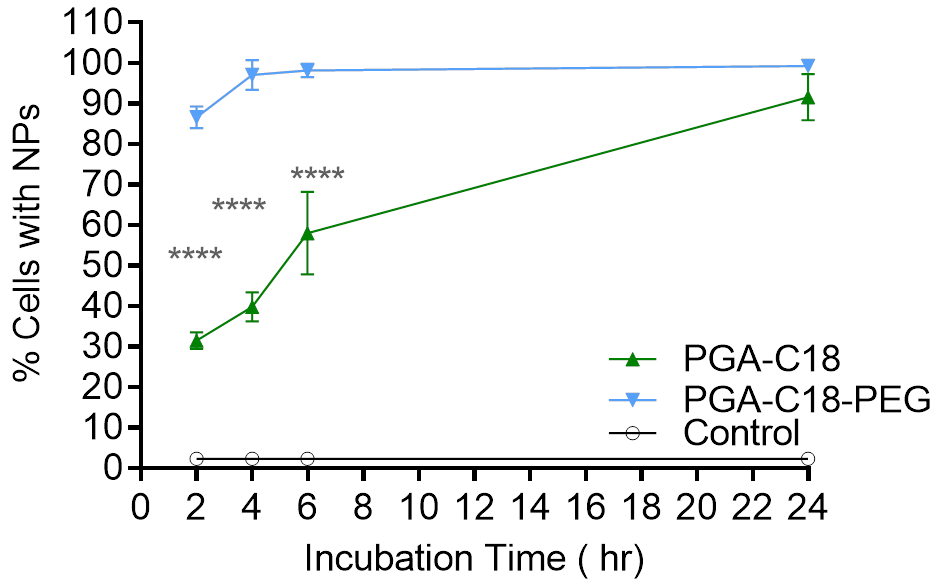


*Figure 37 Time-dependent penetration of NPs (PGA, PGA- PEG, PGA -C18, PGA-C18-PEG) in HCT 116 spheroids by FACS/Hoechst method. a) PGA and PGA- PEG b) PGA-C18 and PGA-C18-PEG NPs. Concentration of NPs= 75µg/ml. (**** display $p < 0.0001$).*

a)

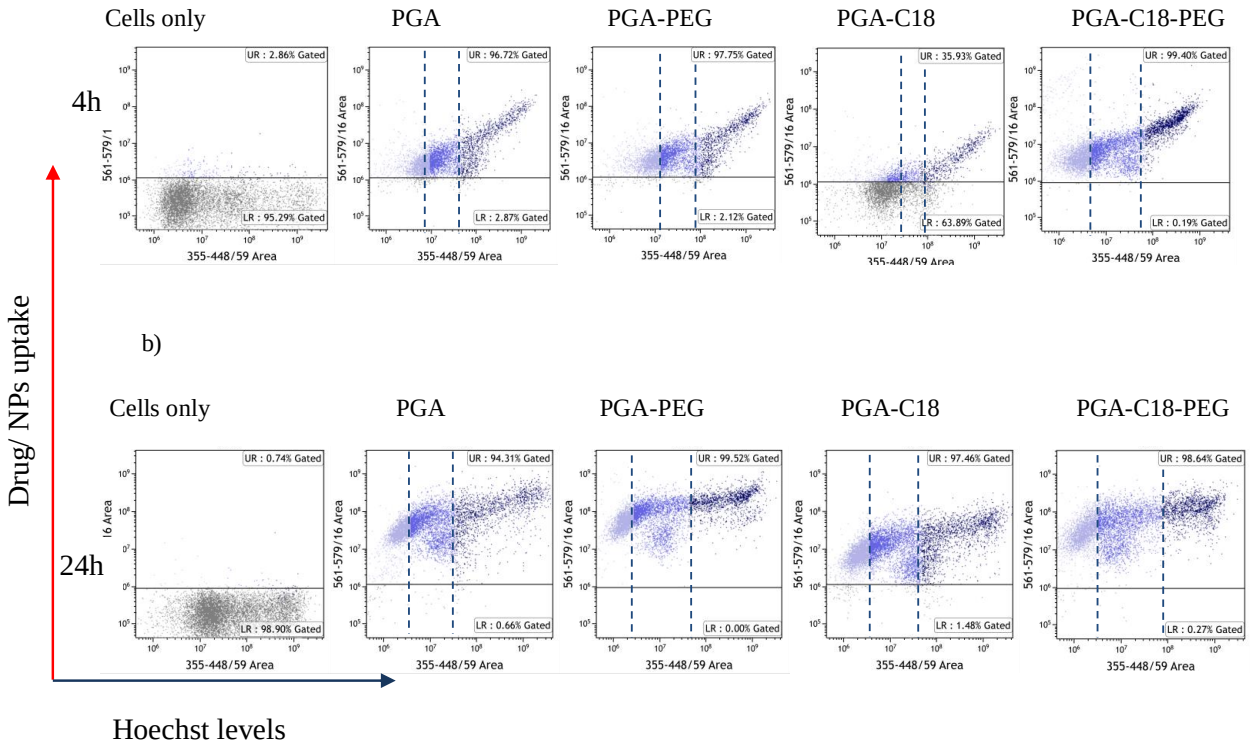
Cells only
PGA
PGA-PEG
PGA-C18
PGA-C18-PEG
4h
24h
Drug/ NPs uptake
Hoechst levels
355-448/59 Area
561-579/16 Area

b)

c)

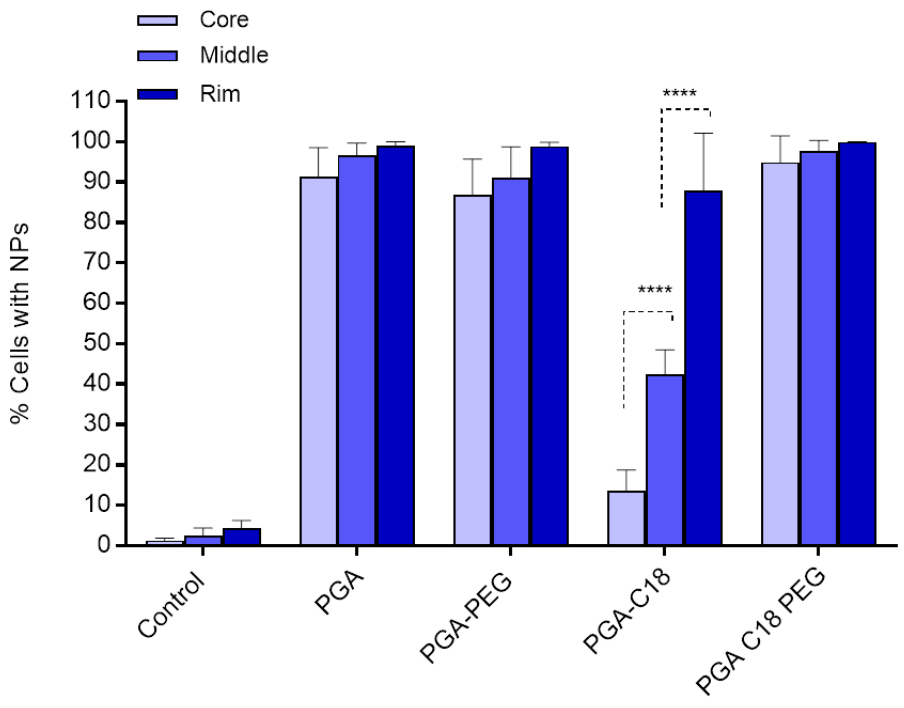
Core
Middle
Rim
% Cells with NPs
Control
PGA
PGA-PEG
PGA-C18
PGA C18 PEG
****
****

d)

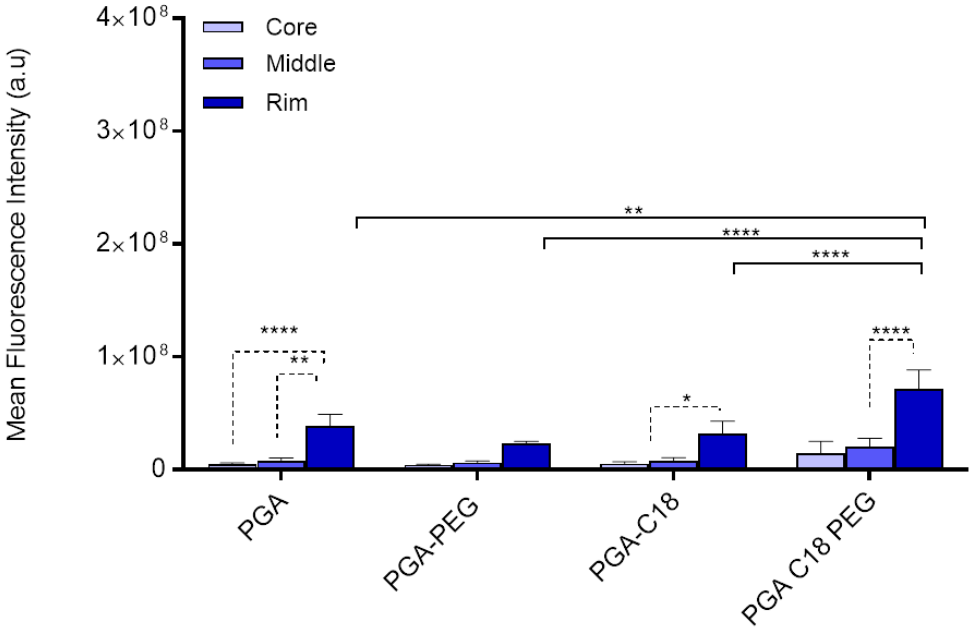
Mean Fluorescence Intensity (a.u)
4×10^8
3×10^8
2×10^8
1×10^8
0
Core
Middle
Rim
**
****
****
****
**
*
****
PGA
PGA-PEG
PGA-C18
PGA C18 PEG

e)

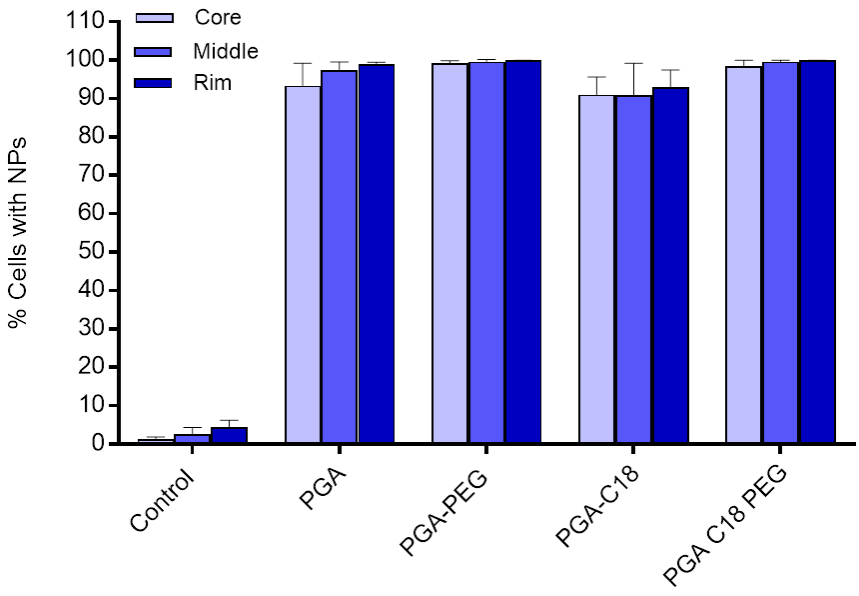
% Cells with NPs
110
100
90
80
70
60
50
40
30
20
10
0
Core
Middle
Rim
Control
PGA
PGA-PEG
PGA-C18
PGA C18 PEG

f)

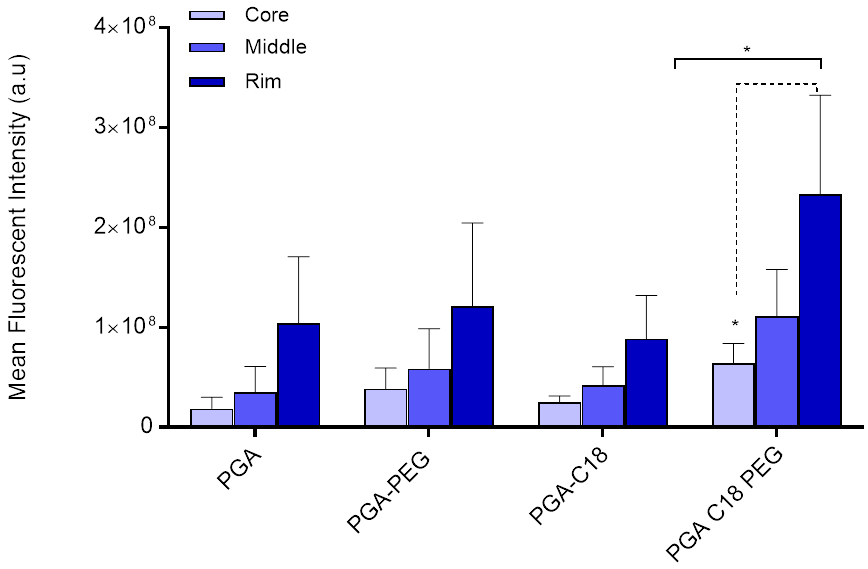


*Figure 38 Distribution of PGA NPs (PGA, PGA- PEG, PGA -C18, PGA- C18-PEG) in HCT 116 spheroids across core, middle and rim by FACS/Hoechst method. a) FACS dot plots showing penetration profile of PGA NPs after 4 and b) 24h; c) Distribution of PGA NPs in spheroids across core, middle and rim after 4h and e) 24h. d) Accumulation of PGA nanoparticles in HCT 116 spheroids measured by mean fluorescence intensity of nanoparticles after 4h (e) and 24h (f) incubation. Concentration of NPs= 75µg/ml; MFI normalized; (****, **, and * display $p < 0.0001$, $p < 0.01$, and $p < 0.05$, respectively).*

## 6.3 Discussion

As highlighted in chapter 4, there is a need for novel anti-cancer delivery systems that are tumour-specific and cell-specific and capable of accessing all the cells in a tumour. Many systems have been developed and characterised in the literature which showed potential as drug carriers; however, they vary

greatly in their physicochemical properties and their abilities to penetrate a tumour is often not well-studied and poorly understood.

PGA NPs are gaining interest due to advantages such as high drug loading and sustained release of the encapsulated therapeutic agent over a longer time period.[166,34] The easily tuneable hydrophobic/hydrophilic properties make this polymer very attractive for drug delivery application. However, little is known about penetration, distribution and uptake behaviour of PGA nanoparticles in a tumour. Unsubstituted PGA NPs and its modified formulations with C18 and PEG groups were prepared to evaluate the influence of these changes on the diffusion and accumulation in 3D colorectal cancer spheroids. We hoped to develop a greater insight into features that enhance or decrease the ability of these systems to deliver drugs deep into the tumour tissue.

NPs were prepared by the solvent displacement method and were characterised by size and charge via Zetasizer Nano. The results showed that all formulations had a comparable mean diameter in a range from 107-119 nm when measured in water and in a range of 115-154 nm when measured under the experimental conditions, in RPMI media with FBS. The sizes corresponded well with the previous observations recorded by others. [34,165,167] Meng et al. measured the considerably larger mean diameter of PGA-C18 NPs of 176 nm.[117] This discrepancy could be a result of variability in the preparation method such as polymer concentration, the rate of stirring or rate of polymer addition to the aqueous phase.

The PDI under the experimental condition was quite broad for unPEGylated PGA NPs (0.25) and even broader for PGA-C18 NPs, (0.54), which indicate

protein adsorption and possibly aggregation. However, once PEG was added more stable formulation was obtained with a considerably narrower PDI (0.04 and 0.11 for PGA-PEG and PGA-C18-PEG respectively).

All NPs had a strongly negative zeta potential in HEPES buffer which became less negative/ near neutral in the culture media suggesting protein adsorption to the surface of these systems under the experimental condition. The negative charge of the particles is thought to arise from free terminal Carboxyl terminal groups of the polymer backbone. [166]

Further, all formulations were found to be non-toxic to HCT- 116 cells after 24h incubation which is consistent with previous reports done in HL-60 and HePG2 cell lines. [166]

In this study, 3D HCT 116 spheroid and the FACS /Hoechst method were employed to investigate the ability of all the formulated PGA NPs to penetrate through the tissue. The results showed that unmodified PGA NPs were able to penetrate to the core of the spheroids already after 2h incubation, reaching 90 % of the cell. However, when this system was modified with the C18 group, the NPs showed significantly slower penetration into spheroids and restricted distribution across middle, core and rim regions of spheroids. The size and charge of those two type NPs were comparable which indicates that other physicochemical features influenced the behaviour of these NPs. By modifying the PGA via partial esterification of the pendant hydroxyl group with the acid chloride of fatty acids, a material with very different characteristics was produced, which may explain the observed results. It was found that contact angle of PGA increased with increased substitution and length of acyl chains

indicating more hydrophobic character. Further, PGA substituted with C18 groups resulted in a semi-crystalline nature. [34, 165] Mackenzie R. et al. found that when the polymer is used for NPs formulation, the C18 groups arrange themselves towards the inside of the nanoparticle shell.[168] This indicates that the hydrophobicity on the surface of nanoparticles should not be affected to a great extent. We thus hypothesise that differences in flexibility of these nanosystems could be responsible for their altered penetration behaviour. The unsubstituted PGA polymer has a glass temperature transition (Tg) much below the room temperature (Tg -30), thus at a body temperature, it exists in its rubbery state, it is soft and flexible. It was suggested that when it is used for the production of NPs, the polymer forms soft and flexible nanosystems. [34] However, an increase of substitution of PGA with C18 groups was shown to increase the Tg values due to a higher fatty acid chain interaction and high steric hindrance amongst polymer chains. This lead to the higher rigidity of NPs produced. In the previous chapter, model polystyrene NPs of comparable size, ~ 100 nm, were also investigated and it was observed that their penetration was restricted to only 20 % of the cell at the periphery of spheroids.[34] Polystyrene is a hard plastic which has a Tg well above the room temperature, (~ 90 °C). This means that at the body temperature this material is in its glassy state thus forms hard and rigid NPs. Thus the slower penetration abilities of PGA-C18 NPs and polystyrene NPs could be a result of lower flexibility in comparison to unsubstituted PGA NPs. Perhaps more flexible PGA systems are capable of squeezing through restricted spaces between the ECM fibres providing more efficient diffusion than the rigid NPs which end up being trapped in the ECM pores restricting their further diffusion. This theory

is in agreement with the observations done in 2 % agarose gel where semi-flexible macromolecules were able to penetrate more efficiently through the gel than rigid spherical systems of the same hydrodynamic radius. [26,46,169,170]

Furthermore, an addition of PEG group to PGA systems was investigated. PEG is a hydrophilic and neutral molecule. It is often attached to the surface of liposomes and NPs to shield their surface charges making them more neutral. This prevents interactions of these systems with blood proteins, opsonins and macrophages allowing for a longer circulation time. [9,20,171,172]

By adding the PEG to unsubstituted PGA and PGA-C18 NPs, it was found they were capable of efficient penetration into the core of spheroids within a short time frame (2-6h) and continued to accumulate until 24h. The addition of PEG to PGA-C18 system significantly improved the penetration and accumulation of the system in spheroids. The PDI results showed that addition of PEG, lead to the production of more stable NPs with much narrower PDI distribution which could influence the penetration of nanoparticles. Further, the addition of PEG to the surface of nanosystems is thought to reduce electrostatic interactions with ECM components thereby improving their diffusion. [47,67,172] This suggests that by adding the PEG groups onto the negative surface of unPEGylated PGA–C18 NPs the surface charges were shielded which resulted in improved penetration capabilities. This is in agreement with previous studies which investigated the effect of the addition of PEG to charged nanoparticles in different ECM matrices and in mucus and found their improved penetration. [67,173] Addition of PEG to NPs > 100 nm was also shown to facilitate diffusion in brain extracellular space. [47,174]

Furthermore, it should be noted that significantly higher cell uptake was achieved with PGA-C18–PEG NPs in cells than in the case of unsubstituted PGA, PGA-C18 and PGA- PEG. This was shown by increased fluorescence levels after 2h incubation in monolayer cells in Figure 36 as well as in spheroids study in Figure 38. This is somewhat surprising as typically PEGylation was shown to lower cell uptake as a result of reduced interactions with the cell surface. Perhaps this mechanism is dependent on the density and Mw of PEG groups on the NPS surface; Different density and MW of PEG may also be a key in achieving the maximal penetration into a tumour; however, this was not investigated in this research. [67]

## 6.4 Conclusions

Here the abilities of experimental NPs to penetrate through spheroids were investigated. PGA based NPs were employed, and their properties modified by the addition of fatty acid chains and /or PEG to evaluate the effect of these changes on the penetration and uptake in 3D cell culture model.

The results highlight that a careful balance of physicochemical properties needs to be achieved when designing nanosystems in order to allow for good penetration as well as high accumulation in tumour cells. The study also shows that rigidity of material used for the production of NPs might play a crucial role in the development of successful drug delivery system for tumour application. While softer unsubstituted PGA NPs of > 100 nm were able to penetrate easily

through the HCT 116 spheroid, the more rigid PGA- C18 NPs showed slower penetration. Furthermore, the positive influence of PEGylation of NPs on penetration through spheroids was demonstrated.

The results highlight the importance of testing the NPs for their tumour diffusion capabilities in the early stages of the development process in order to develop the design with optimal features.

# Chapter 7 Summary and future perspectives

Limited penetration and poor spatial distribution of drugs throughout solid tumours represent a significant barrier to their anticancer efficacy. As seen in this study certain drugs and nanosystems show poor diffusion and distribution throughout spheroids. This may impair their effectiveness in a tumour as they may localise in the regions close to blood vessels, leaving large regions of a tumour untreated. This can lead to cancer regrowth and progression. The knowledge of the features of nanoparticles that affect penetration and distribution in tissue is thus paramount for the design of improved anticancer drug delivery systems.

The pharmacokinetic properties of drugs and nanodelivery systems are evaluated in early-development phase using animal models. This allows the determination of important parameters such as the volume of distribution, plasma half-life and clearance from the body. However, tests performed in these models provide limited information about the behaviour of therapeutics after they access a tumour. Therefore information about how well these systems diffuse, distribute and localise in a tumour space is not readily accessible. The failure to account for this problem in the *in vivo* assessment may lead to the poor prediction of drug efficiency since a drug can show higher concentration in a tumour on average than in normal tissues, but due to poor penetration, only small percentage of cells close to blood vessels will be exposed to a cytotoxic concentration.[175] A rapid and easy *in vitro* cell screening assay would aid the process of testing for penetration and distribution of

systems in a tumour and allow adjustment of the properties of NPs to achieve optimal delivery of the drug into a tumour.

In this study, 3D colorectal cancer models were optimised and characterised at different stages of their growth. Our results showed that development of pathological features such as necrotic core and hypoxia were dependent on seeding cell density and time in culture. A well-defined 3D HCT 116 model at day 3 in culture with an average diameter of 440 μm and no hypoxia nor necrotic core present was employed for *in vitro* evaluation of diffusion of drug and nanoparticles. The quantitative *in vitro* method using Flow cytometry in combination with Hoechst dye was optimised for assessing drug delivery systems in the 3D model. The method was shown to be robust and highly sensitive.

To develop a better understanding of the features affecting tissue penetration a series of model polystyrene nanoparticles were investigated with different sizes and surface chemistries.

Our results showed that the size of the nanoparticles is important in achieving good diffusion in tumours. While 100 nm near neutral polystyrene NPs could not penetrate through spheroids, 50 nm and 30 nm near neutral NPs showed good penetration. This is in agreement with the reports in the literature which suggested that when the diameter of NPs starts to exceed ECM pore size, its diffusion becomes slower. For instance, penetration of particles larger than 60 nm in diameter was showed to have a hindered diffusion through the collagen matrix. [46,64,66,143,169]

The results also showed that when the surface charge of these smaller particles (50 nm) was changed to positive or negative, their penetration became significantly slower or restricted. This shows that even if the nanoparticle size lies below the ECM pore sizes, the penetration may still be limited due to electrostatic interactions of charged NPs with ECM.

It needs also be noted that nanoparticle surface charge is known to influence cell uptake which is also essential for therapeutic activity.[176]. Various nanosystems have been used to study these interactions, and it has been seen that positively charged particles, in general, show higher uptake into cells than negatively charged nanoparticles.[176–179] This was observed in the study done by Yameen et al., who investigated nanoparticles of approximately the same particle size but with different surface charge (ranging from ~ –25 mV to +30 mV) and showed that the positively charged nanoparticles exhibited a high accumulation in the mitochondria of human cervical cancer (HeLa) cell than negatively charged NPs.[177] It has been hypothesised that this is a result of increased interaction between the positively charged nanoparticles and negatively charged cell surface that enhances the nanoparticles internalisation into cells via endocytosis. [157,176,180] Further, positively charged NPs have also been showed to be internalised more rapidly than the than the neutral NPs or PEGylated NPs which have reduced electrostatic interactions with the cell membrane. [178,179] This suggests that the requirements for rapid and effective endocytosis into cells, i.e. positive surface charge are in conflict with the requirements for improved penetration through interstitial space, i.e., near neutral surface charge. This implies that the surface chemistry must be

carefully adjusted to achieve improved penetration into a tumour as well as high uptake into cells.

Doxorubicin drug was also studied in the 3D model via Flow/ Hoechst method. It was found that its penetration was slow and time-dependent. The results imply that Dox given at clinically relevant dose would not be able to gain sufficient access to all the cells in a tumour for a full therapeutic effect. It was also observed that commercially available liposomal formulation of Dox-Doxil did not improve accumulation of Dox in spheroids after 24h incubation.

Another matter that requires more in-depth investigation is the observed limited diffusion of small anticancer drug Dox, but a good movement of much larger 50 nm rigid polystyrene nanoparticles.

This is somewhat surprising as diffusion was shown to be inversely proportional to molecular weight which suggests that larger nanoparticles would diffuse much more slowly than low molecular weight drugs. [47]

The tumour ECM consists of a highly interconnected network of collagen fibres, proteoglycans and GAGs. Penetration of drugs through tissue is believed to be largely through the ECM, and it will be dependent on factors such as metabolism of the drugs, and on binding to cells and tissue components. [137, 61] Laurent et al. explained this behaviour in terms of a sieving mechanism based on the behaviour of globular proteins in hyaluronate solutions and sulphated proteoglycans. It was proposed that protein molecules act as if they are enclosed in “holes “in the network from which they cannot escape because of steric restriction. Ogston and co-workers proposed that the

diffusion acts as a random process in which the particles move by unit displacements and in which the decreased diffusion rate in a polymer network is dependent on the probability that a particle finds a "hole" in the network into which it can move. They compared the interstitial space to a chromatographic column as they observed that large molecules appear to equilibrate in the tissue faster than smaller ones.[65,66,181,182] Our results showing longer accumulation of smaller drug molecules in comparison to larger NPs which penetrated and accumulated in cells across spheroid much faster fits well with these theories. Furthermore, it was proposed that liposomes of larger size and near neutral surface chemistry have decreased interactions with surrounding cells and ECM, and their movement is mediated by convection. [147] In a later study, Jain et al. also suggested that small molecules travel by diffusion which is very restricted through the interstitial space; however, larger molecules (up to ECM pore size) can take advantage of movement by convection.[26] This implies that nanosystems with small enough diameter and rightly adjusted surface charge, could penetrate into a tumour easily and be retained there over time. This means they could deliver uniform drug payload into all cells across spheroid/ tumour, unlike a free drug which diffusion was slow and delivery of a drug would be restricted to the cells close to blood vessels.

Further, in the study, a series of novel biodegradable PGA polymers were synthesised with the aim of investigating a promising, new, realistic system in 3D spheroids. Penetration abilities through spheroids of PGA NPs with different modifications were studied. Our results showed that despite the larger size of ~100 nm, PGA NPs penetrated to the core of spheroids effectively;

unlike polystyrene model nanoparticles of comparable size (100 nm). We propose that this greater ability of these systems to penetrate through spheroids is due to a softer, more flexible polymer used in their formulation. With the Tg of PGA being -37, they are thought to be much more like an emulsion and produce viscous liquid-like NPs. It has been shown that linear or more flexible molecules are better at diffusion through ECM than globular systems with a similar hydrodynamic radius.[169]

Modifications of the surface of nanoparticles by adding hydrophilic PEG is often employed in the design of nanosystems as it was showed to decrease clearance by the MPS/ RES system.[20,183] In the present work, the effect of PEG on the penetration of PGA- NPs through spheroids was investigated. Our results showed that addition of PEG to PGA-C18 NPs significantly improved its delivery to the core of spheroids. While it is likely that shielding the NPs surface prevents its interactions with ECM and cell components, PGA-C18 is more rigid than PGA, and PEGylation of this polymer reduces the rigidity, and this may also have some impact on penetration. Further, it was observed these systems provided higher cell uptake than the unPEGylated NPs which is contradictory with the reports by others. [67,184] This discrepancy could be a result of different PEG density and length on the surface used in the studies. In this study PEG 2000 was evaluated using PGA; however, this may be relevant exclusively for these NPs and evaluating varying lengths and densities of PEG on the surface of various systems may be necessary for researchers to optimise particle penetration and uptake capabilities.[67] This can also be related to the rigidity of the system or type of cell line used. [9]

The findings of this study highlight that tissue penetration of drugs and nanodrug delivery systems is challenging and should not be underestimated in the development of new anticancer treatments. Improved tissue penetration would be one of many parameters that novel drug delivery systems should account for.

With previous reports of advantages of PGA systems such as possibilities of enhanced drug loading and slow release this data further highlights the potential of PGA NPs as antitumor delivery systems. The finding also implies that more flexible systems could be more advantageous for drug delivery into a tumour.

Developing the system capable of easy penetration and uniform drug delivery to cells would lead to a reduction in systemic toxicity as lower blood drug levels would be required to achieve maximum response. Fast and more even delivery of a drug into cells across a whole tumour would also mean that all cells would be exposed to equal therapeutic levels of the drug for a longer time, which could reduce the effects of the lower S-phase fraction often observed during treatment in a tumour. [52]

However, in the design of nanoparticles, one must remember that the system encounters other barriers *in vivo* that need to be accounted for. The hydrophilic surface is required to reduce opsonisation reactions and clearance by MPS. [14] The nanoformulation should also be small enough to allow for extravasation through blood vessels and tumour interstitial ECM. [20] However, not too small, as some studies demonstrated that PEG-b-PCL micelles with diameters in the range of 15–25 nm have shorter circulation half-lives and are susceptible to

more rapid clearance relative to 60 nm micelles.[73] Smaller micelles (15 nm) were also showed to have limited retention in HeLa and HT29 tumours. [73] The optimal drug delivery systems thus should be large enough to avoid this mechanism but small enough to allow for good delivery of drug payload into a tumour. Larger carrier size is also beneficial for incorporating higher amounts of drug per particle.

Treatments combined with ECM degrading enzymes to influence the penetration of NPS have also been explored.[185,186] Further, the innovative idea of multistage NPs was also proposed whereby large 100-nm particles are designed to enable passage via EPR effect but once inside the tumour environment the system can release 10-nm particles to enhance the interstitial diffusion. [47]

Our results suggest that NPs of ~ 50 nm or larger but more flexible NPs with near neutral surface charge or coated with PEG may be more beneficial for anticancer drug delivery application.

While the findings give us insights into parameters that can positively or negatively impact the ability of nanosystems to penetrate a tumour, more importantly, they highlight the need to screen the systems for their ability to diffuse and accumulate in a tumour at an early stage in their development process. It is clear that a careful balance of physicochemical features needs to be achieved to design nanosystems with optimal performance. [162]

The *in vitro* method using 3D spheroids and Flow cytometry combined with Hoechst allow for robust quantitative analysis of NPs and could be readily

employed *in vitro* during design and development of novel anticancer nano drug carriers. [1]

# Chapter 8 Future steps

While the present study gives us a good idea of the relative performance of different types of NPs, this is still a first step towards understanding how to develop useful delivery systems for a tumour.

Evaluating more nanoparticles made of different materials, of varying size, shape and with different targeting ligands using our FACS screening system would further enhance the understanding of optimal characteristics of nanoparticles necessary to effectively deliver an anticancer drug into a tumour.

Further, our 3D cell culture models used in the study are made of relatively homogenous cell populations whereas in a tumour more heterogeneous environment is found. A tumour has various combinations of host cells and tumour cells which vary in their properties. These are likely to affect both ECM and rates of endocytosis which can impact on uptake and penetration of anticancer nanosystems. Developing different realistic co-culture models with tumour cells and in combination with host cells, e.g. fibroblasts and/or immune cells and using them to perform penetration studies of the nanosystems would further enhance the picture of how NPs penetrate through tumours. Additionally, such models could potentially be used to study different signalling pathways and interactions in a tumour such as autocrine and paracrine interactions as well as to look for new targets for anticancer drugs.

It would also be advantageous to repeat the NPs penetration experiments in an animal model *in vivo*. This would allow us to confirm whether the same trend

was achieved *in vivo* as seen in our 3D spheroids thus help to validate the predictive capabilities of our *in vitro* model.

Also, future research on the influence of spheroid microenvironment such as hypoxia, proliferative gradients or necrosis on the penetration and uptake of NPs and anticancer drugs would be advantageous. The 3D models with specific characteristics can be selected from our library of well-characterised colorectal models described in chapter 3 and used to perform such studies. These models could be an invaluable tool for developing and testing new cancer therapies *in vitro*.

In the future, developing methods that incorporate the angiogenesis process in the spheroids would undoubtedly better mimic a real tumour and thus allow for more meaningful data to be generated early in the drug discovery phase. Developing such advanced 3D models would fast-track drug screening hopefully, yielding more effective and less toxic anticancer drugs and nanodrug delivery systems as future therapies.

# Bibliography


(1) Minchinton, A. I.; Tannock, I. F. Drug Penetration in Solid Tumours. *Nat. Rev. Cancer* **2006**, *6*, 583–592.

(2) Brown, J. M.; Giaccia, A. J. The Unique Physiology of Solid Tumors : Opportunities ( and Problems ) for Cancer Therapy The Unique Physiology of Solid Tumors : Opportunities ( and Problems ) for Cancer Therapy1. *Cancer Res.* **1998**, *58*, 1408–1416.

(3) Dreher, M. R.; Liu, W.; Michelich, C. R.; Dewhirst, M. W.; Yuan, F.; Chilkoti, A. Tumor Vascular Permeability, Accumulation, and Penetration of Macromolecular Drug Carriers. *J. Natl. Cancer Inst.* **2006**, *98*, 335–344.

(4) Lütfi Genç1, G. D. and G. G. Formulation of Nano Drug Delivery Systems. *J. Mater. Sci.* **2011**, *A1*, 132–137.

(5) Ferrari, M. Cancer Nanotechnology: Opportunities and Challenges. *Nat. Rev. Cancer* **2005**.

(6) Duncan, R.; Ringsdorf, H.; Satchi-Fainaro, R. Polymer Therapeutics—polymers as Drugs, Drug and Protein Conjugates and Gene Delivery Systems: Past, Present and Future Opportunities. *J. Drug Target.* **2006**, *14*, 337–341.

(7) Fang, J.; Nakamura, H.; Maeda, H. The EPR Effect: Unique Features of Tumor Blood Vessels for Drug Delivery, Factors Involved, and

Limitations and Augmentation of the Effect ☆. *Adv. Drug Deliv. Rev.* **2011**, *63*, 136–151.

(8) Nakamura, Y.; Mochida, A.; Choyke, P. L.; Kobayashi, H. Nanodrug Delivery: Is the Enhanced Permeability and Retention Effect Sufficient for Curing Cancer? *Bioconjug. Chem.* **2016**, *27*, 2225–2238.

(9) Steichen, S. D.; Caldorera-Moore, M.; Peppas, N. a. A Review of Current Nanoparticle and Targeting Moieties for the Delivery of Cancer Therapeutics. *Eur. J. Pharm. Sci.* **2012**, *48*, 416–427.

(10) Karmali, P. P.; Kotamraju, V. R.; Kastantin, M.; Black, M.; Missirlis, D.; Tirrell, M.; Ruoslahti, E. Targeting of Albumin-Embedded Paclitaxel Nanoparticles to Tumors. *Nanomedicine* **2009**, *5*, 73–82.

(11) Hu, Y.; Xie, J.; Tong, Y. W.; Wang, C.-H. Effect of PEG Conformation and Particle Size on the Cellular Uptake Efficiency of Nanoparticles with the HepG2 Cells. **2006**.

(12) Verma, A.; Stellacci, F. Effect of Surface Properties on Nanoparticleâ€“Cell Interactions. *Small* **2010**, *6*, 12–21.

(13) De Jong, W. H.; Borm, P. J. Drug Delivery and Nanoparticles: Applications and Hazards. *Int. J. Nanomedicine* **2008**, *3*, 133–149.

(14) Meng, W. EVALUATION OF A NANOPARTICLE DRUG DELIVERY VEHICLE IN MEDULLOBLASTOMA AND ORGANOTYPIC BRAIN CELL CULTURES Thesis Submitted to the University of Nottingham. **2006**.

(15) Panyam, J.; Labhasetwar, V. B Iodegradable Nanoparticles for Drug and Gene Delivery to Cells and Tissue. *Adv. Drug Deliv. Rev.* **2003**, *55*, 329–347.

(16) Govender, T.; Stolnik, S.; Garnett, M. C.; Illum, L.; Davis, S. S. PLGA Nanoparticles Prepared by Nanoprecipitation: Drug Loading and Release Studies of a Water Soluble Drug. *J. Control. Release* **1999**, *57*, 171–185.

(17) Govender, T.; Riley, T.; Ehtezazi, T.; Garnett, M. C.; Stolnik, S.; Illum, L.; Davis, S. S. Defining the Drug Incorporation Properties of PLA–PEG Nanoparticles. *Int. J. Pharm.* **2000**, *199*, 95–110.

(18) Brigger, I.; Dubernet, C.; Couvreû, P. N Anoparticles in Cancer Therapy and Diagnosis. *Adv. Drug Deliv. Rev.* **2002**, *54*, 631–651.

(19) Desai, M. P.; Labhasetwar, V.; Walter, E.; Levy, R. J.; Amidon, G. L. The Mechanism of Uptake of Biodegradable Microparticles in Caco-2 Cells Is Size Dependent. *Pharm. Res.* **1997**.

(20) Gabizon, A.; Shmeeda, H.; Barenholz, Y. Pharmacokinetics of Pegylated Liposomal Doxorubicin Review of Animal and Human Studies. *Clin Pharmacokinet* **2003**, *42*, 419–436.

(21) Gaur, U.; Sahoo, S. K.; De, T. K.; Ghosh, P. C.; Maitra, A.; Ghosh, P. K. Biodistribution of Fluoresceinated Dextran Using Novel Nanoparticles Evading Reticuloendothelial System. *Int. J. Pharm.* **2000**, *202*, 1–10.

(22) Brannon-Peppas, L.; Blanchette, J. O. Nanoparticle and Targeted

Systems for Cancer Therapy. **2004**.

(23) Storm " ', G.; Belliot, S. 0; Daemenb, T.; Lasic, D. D. Surface Modification of Nanoparticles to Oppose Uptake by the Mononuclear Phagocyte System. *Adv. Drug Deliv. Rev.* **1995**, *17*, 31–48.

(24) Wang, X.; Zhen, X.; Wang, J.; Zhang, J.; Wu, W.; Jiang, X. Doxorubicin Delivery to 3D Multicellular Spheroids and Tumors Based on Boronic Acid-Rich Chitosan Nanoparticles. *Biomaterials* **2013**, *34*, 4667–4679.

(25) Campbell, R. B.; Fukumura, D.; Brown, E. B.; Mazzola, L. M.; Izumi, Y.; Jain, R. K.; Torchilin, V. P.; Munn, L. L. Cationic Charge Determines the Distribution of Liposomes between the Vascular and Extravascular Compartments of Tumors. *Cancer Res.* **2002**, *62*, 6831–6836.

(26) Jain, R. K. Transport of Molecules in the Tumor Interstitium: A Review. *Cancer Res.* **1987**, *47*, 3039–3051.

(27) Gref, R.; Lü Ck, M.; Quellec, P.; Marchand, M.; Dellacherie, E.; Harnisch, S.; Blunk, T.; Mü Ller, R. H. "Stealth" Corona-Core Nanoparticles Surface Modified by Polyethylene Glycol (PEG): Influences of the Corona (PEG Chain Length and Surface Density) and of the Core Composition on Phagocytic Uptake and Plasma Protein Adsorption. *Colloids Surfaces B Biointerfaces* **2000**, *18*, 301–313.

(28) Sheng, Y.; Yuan, Y.; Liu, C.; Tao, X.; Shan, X.; Xu, F. In Vitro Macrophage Uptake and in Vivo Biodistribution of PLA–PEG

Nanoparticles Loaded with Hemoglobin as Blood Substitutes: Effect of PEG Content. *J. Mater. Sci. Mater. Med.* **2009**, *20*, 1881–1891.

(29) Richards, D. A.; Maruani, A.; Chudasama, V. Antibody Fragments as Nanoparticle Targeting Ligands: A Step in the Right Direction. *Chem. Sci.* **2017**, *8*, 63–77.

(30) Riley, T.; Govender, T.; Stolnik, S.; Xiong, C. D.; Garnett, M. C.; Illum, L.; Davis, S. S. Colloidal Stability and Drug Incorporation Aspects of Micellar-like PLA–PEG Nanoparticles. *Colloids Surfaces B Biointerfaces* **1999**, *16*, 147–159.

(31) Ló pez-Dá vila, V.; Seifalian, A. M.; Loizidou, M. Organic Nanocarriers for Cancer Drug Delivery. *Curr. Opin. Pharmacol.* **2012**, *12*, 414–419.

(32) Fu, Y.; Kao, W. J. Drug Release Kinetics and Transport Mechanisms of Non-Degradable and Degradable Polymeric Delivery Systems. *Expert Opin. Drug Deliv.* **2010**, *7*, 429–444.

(33) Panyam, J.; Williams, D.; Dash, A.; Leslie-Pelecky, D.; Labhasetwar, V.; Amidon, G. L.; Levy, R. J.; Labhasetwar, V. Solid-state Solubility Influences Encapsulation and Release of Hydrophobic Drugs from PLGA/PLA Nanoparticles. *J. Pharm. Sci.* **2004**, *93*, 1804–1814.

(34) Taresco, V.; Creasey, R. G.; Kennon, J.; Mantovani, G.; Alexander, C.; Burley, J. C.; Garnett, M. C. Variation in Structure and Properties of Poly(Glycerol Adipate) via Control of Chain Branching during Enzymatic Synthesis. *Polymer (Guildf).* **2016**, *89*, 41–49.

(35) Lasic, D. Novel Applications of Liposomes. *Trends Biotechnol.* **1998**,

*16*, 307–321.

(36) Malam, Y.; Loizidou, M.; Seifalian, A. M. Liposomes and Nanoparticles: Nanosized Vehicles for Drug Delivery in Cancer. *Trends Pharmacol. Sci.* **2009**, *Vol.30*, 592–599.

(37) Singer, J. W.; Baker, B.; de Vries, P.; Kumar, A.; Shaffer, S.; Vawter, E.; Bolton, M.; Garzone, P. Poly-(L)-Glutamic Acid-Paclitaxel (CT-2103) [XYOTAX$^{TM}$], a Biodegradable Polymeric Drug Conjugate. In; Springer, Boston, MA, 2004; pp. 81–99.

(38) Yared, J. A.; Tkaczuk, K. H. R. Update on Taxane Development: New Analogs and New Formulations. *Drug Des. Devel. Ther.* **2012**, *6*, 371–384.

(39) Kataoka, K.; Harada, A.; Nagasaki, Y. Block Copolymer Micelles for Drug Delivery: Design, Characterization and Biological Significance ☆. *Adv. Drug Deliv. Rev.* **2012**, *64*, 37–48.

(40) Nasongkla, N.; Bey, E.; Ren, J.; Ai, H.; Khemtong, C.; Guthi, J. S.; Chin, S.-F.; Sherry, A. D.; Boothman, D. A.; Gao, J. Multifunctional Polymeric Micelles as Cancer-Targeted, MRI-Ultrasensitive Drug Delivery Systems. *Nano Lett.* **2006**, *6*, 2427–2430.

(41) Gaucher, G.; Dufresne, M.-H.; Sant, V. P.; Kang, N.; Maysinger, D.; Leroux, J.-C. Block Copolymer Micelles: Preparation, Characterization and Application in Drug Delivery. *J. Control. Release* **2005**, *109*, 169–188.

(42) Yellepeddi, V. K.; Kumar, A.; Palakurthi, S. Biotinylated Poly(Amido)Amine (PAMAM) Dendrimers as Carriers for Drug Delivery to Ovarian Cancer Cells in Vitro. *Anticancer Res.* **2009**, *29*, 2933–2943.

(43) Dhanikula, R. S.; Argaw, A.; Bouchard, J. F.; Hildgen, P. Methotrexate Loaded Polyether-Copolyester Dendrimers for the Treatment of Gliomas: Enhanced Efficacy and Intratumoral Transport Capability. *Mol. Pharm.* **2008**, *5*, 105–116.

(44) Kukowska-Latallo, J. F.; Candido, K. A.; Cao, Z.; Nigavekar, S. S.; Majoros, I. J.; Thomas, T. P.; Balogh, L. P.; Khan, M. K.; Baker, J. R. Nanoparticle Targeting of Anticancer Drug Improves Therapeutic Response in Animal Model of Human Epithelial Cancer. *Cancer Res.* **2005**, *65*.

(45) Tang, L.; Gabrielson, N. P.; Uckun, F. M.; Fan, T. M.; Cheng, J. Size-Dependent Tumor Penetration and in Vivo Efficacy of Monodisperse Drug-Silica Nanoconjugates. *Mol. Pharm.* **2013**, *10*, 883–892.

(46) Jain, R. K.; Stylianopoulos, T. Delivering Nanomedicine to Solid Tumors. *Nat. Rev. Clin. Oncol.* **2010**, *7*, 653–664.

(47) Waite, C. L.; Roth, C. M. Nanoscale Drug Delivery Systems for Enhanced Drug Penetration into Solid Tumors: Current Progress and Opportunities. *Crit. Rev. Biomed. Eng.* **2012**, *40*, 21–41.

(48) Barua, S.; Mitragotri, S. Challenges Associated with Penetration of Nanoparticles across Cell and Tissue Barriers: A Review of Current

Status and Future Prospects. *Nano Today* **2014**, *9*, 223–243.

(49) Pluen, A.; Boucher, Y.; Ramanujan, S.; McKee, T. D.; Gohongi, T.; di Tomaso, E.; Brown, E. B.; Izumi, Y.; Campbell, R. B.; Berk, D. A.; *et al.* Role of Tumor-Host Interactions in Interstitial Diffusion of Macromolecules: Cranial vs. Subcutaneous Tumors. *Proc. Natl. Acad. Sci. U. S. A.* **2001**, *98*, 4628–4633.

(50) Wenzel, C.; Riefke, B.; Gründemann, S.; Krebs, A.; Christian, S.; Prinz, F.; Osterland, M.; Golfier, S.; Räse, S.; Ansari, N.; *et al.* 3D High-Content Screening for the Identification of Compounds That Target Cells in Dormant Tumor Spheroid Regions. *Exp. Cell Res.* **2014**, *323*, 131–143.

(51) Nyga, A.; Cheema, U.; Loizidou, M. 3D Tumour Models: Novel in Vitro Approaches to Cancer Studies. *J. Cell Commun. Signal.* **2011**, *5*, 239–248.

(52) Kyle, A. H.; Huxham, L. A.; Yeoman, D. M.; Minchinton, A. I. Cancer Therapy : Preclinical Limited Tissue Penetration of T Axanes : A Mechanism for Resistance in Solid T Umors. **2007**, *13*, 2804–2811.

(53) Tannock, I. F.; Hot, D. Acid PH in Tumors and Its Potential for Therapeutic Exploitation1. *CANCER Res.* **1989**, *49*, 4373–4384.

(54) Huber, V.; Camisaschi, C.; Berzi, A.; Ferro, S.; Lugini, L.; Triulzi, T.; Tuccitto, A.; Tagliabue, E.; Castelli, C.; Rivoltini, L. Cancer Acidity: An Ultimate Frontier of Tumor Immune Escape and a Novel Target of Immunomodulation. *Semin. Cancer Biol.* **2017**, *43*, 74–89.

(55) Kato, Y.; Ozawa, S.; Miyamoto, C.; Maehata, Y.; Suzuki, A.; Maeda, T.; Baba, Y. Acidic Extracellular Microenvironment and Cancer. *Cancer Cell Int.* **2013**, *13*, 89.

(56) Davies, C. de L.; Berk, D. A.; Pluen, A.; Jain, R. K. Comparison of IgG Diffusion and Extracellular Matrix Composition in Rhabdomyosarcomas Grown in Mice versus in Vitro as Spheroids Reveals the Role of Host Stromal Cells. *Br. J. Cancer* **2002**, *86*, 1639–1644.

(57) Netti, P. A.; Berk, D. A.; Swartz, M. A.; Grodzinsky, A. J.; Jain, R. K. Role of Extracellular Matrix Assembly in Interstitial Transport in Solid Tumors. *Cancer Res.* **2000**, *60*, 2497–2503.

(58) Mikhail, A. S.; Eetezadi, S.; Allen, C. Multicellular Tumor Spheroids for Evaluation of Cytotoxicity and Tumor Growth Inhibitory Effects of Nanomedicines in Vitro: A Comparison of Docetaxel-Loaded Block Copolymer Micelles and Taxotere®. *PLoS One* **2013**, *8*, e62630.

(59) Goodman, T. T.; Chen, J.; Matveev, K.; Pun, S. H. NIH Public Access. **2010**, *101*, 388–399.

(60) Goodman, T. T.; Olive, P. L.; Pun, S. H. Increased Nanoparticle Penetration in Collagenase-Treated Multicellular Spheroids. *Int. J. Nanomedicine* **2007**, *2*, 265–274.

(61) Magzoub, M.; Jin, S.; Verkman, A. S. Enhanced Macromolecule Diffusion Deep in Tumors after Enzymatic Digestion of Extracellular Matrix Collagen and Its Associated Proteoglycan Decorin. *FASEB J.* **2007**, *22*, 276–284.

(62) FESSLER, J. H. Water and Mucopolysaccharide as Structural Components of Connective Tissue. *Nature* **1957**, *179*, 426–427.

(63) Comper, W. D.; Laurent, T. C. Physiological Function of Connective Tissue Polysaccharides. *Physiol. Rev.* **1978**, *58*, 255–315.

(64) Ramanujan, S.; Pluen, A.; McKee, T. D.; Brown, E. B.; Boucher, Y.; Jain, R. K. Diffusion and Convection in Collagen Gels: Implications for Transport in the Tumor Interstitium. *Biophys. J.* **2002**, *83*, 1650–1660.

(65) Laurent, T. C.; Ogston, A. G. The Interaction between Polysaccharides and Other Macromolecules 4. THE OSMOTIC PRESSURE OF MIXTURES OF SERUM ALBUMIN AND HYALURONIC ACID*. *Biochem. J* **1963**, *89*.

(66) Ogston, A. G.; Shermant, T. F. With 2 Text-Ftgures EFFECTS OF HYALURONIC ACID UPON DIFFUSION OF SOLUTES AND FLOW OF SOLVENT. *J. Physiol* **1961**, *156*, 67–74.

(67) Tomasetti, L.; Liebl, R.; Wastl, D. S.; Breunig, M. Influence of PEGylation on Nanoparticle Mobility in Different Models of the Extracellular Matrix. **2016**.

(68) Lu, P.; Takai, K.; Weaver, V. M.; Werb, Z. Extracellular Matrix Degradation and Remodeling in Development and Disease. *Cold Spring Harb. Perspect. Biol.* **2011**, *3*.

(69) L. Berg, E.; Hsu, Y.-C.; Lee, J. A. Consideration of the Cellular Microenvironment: Physiologically Relevant Co-Culture Systems in Drug Discovery. *Adv. Drug Deliv. Rev.* **2014**, *69*, 190–204.

(70) Cook, N. Predictive in Vivo Animal Models and Translation to Clinical Trials. *Drug Discov. Today* **2012**, *17*, 253–260.

(71) Vinci, M.; Gowan, S.; Boxall, F.; Patterson, L.; Zimmermann, M.; Court, W.; Lomas, C.; Mendiola, M.; Hardisson, D.; Eccles, S. A. Advances in Establishment and Analysis of Three-Dimensional Tumor Spheroid-Based Functional Assays for Target Validation and Drug Evaluation. *BMC Biol.* **2012**, *10*, 29.

(72) Breslin, S.; O'Driscoll, L. Three-Dimensional Cell Culture: The Missing Link in Drug Discovery. *Drug Discov. Today* **2013**, *18*, 240–249.

(73) Mikhail, A. S.; Eetezadi, S.; Ekdawi, S. N.; Stewart, J.; Allen, C. Image-Based Analysis of the Size- and Time-Dependent Penetration of Polymeric Micelles in Multicellular Tumor Spheroids and Tumor Xenografts. *Int. J. Pharm.* **2014**, *464*, 168–177.

(74) Lovitt, C. J.; Shelper, T. B.; Avery, V. M. Advanced Cell Culture Techniques for Cancer Drug Discovery. *Biology (Basel).* **2014**, *3*, 345–367.

(75) Astashkina, A.; Mann, B.; Grainger, D. W. A Critical Evaluation of in Vitro Cell Culture Models for High-Throughput Drug Screening and Toxicity. *Pharmacol. Ther.* **2012**, *134*, 82–106.

(76) Unger, C.; Kramer, N.; Walzl, A.; Scherzer, M.; Hengstschläger, M.; Dolznig, H. Modeling Human Carcinomas : Physiologically Relevant 3D Models to Improve Anti-Cancer Drug Development ☆. *Adv. Drug Deliv. Rev.* **2014**, *79–80*, 50–67.

(77) Leong, D. T.; Ng, K. W. Probing the Relevance of 3D Cancer Models in Nanomedicine Research. *Adv. Drug Deliv. Rev.* **2014**, *79–80*, 95–106.

(78) Ivascu, A.; Kubbies, M. Rapid Generation of Single-Tumor Spheroids for High-Throughput Cell Function and Toxicity Analysis. *J. Biomol. Screen.* **2006**, *11*, 922–932.

(79) Thoma, C. R.; Zimmermann, M.; Agarkova, I.; Kelm, J. M.; Krek, W. 3D Cell Culture Systems Modeling Tumor Growth Determinants in Cancer Target Discovery. *Adv. Drug Deliv. Rev.* **2014**, *69–70C*, 29–41.

(80) Lee, J.-H.; Na, K.; Song, S.-C.; Lee, J.; Kuh, H.-J. The Distribution and Retention of Paclitaxel and Doxorubicin in Multicellular Layer Cultures. *Oncol. Rep.* **2012**, *27*, 995–1002.

(81) Kim, J. Bin. Three-Dimensional Tissue Culture Models in Cancer Biology. *Semin. Cancer Biol.* **2005**, *15*, 365–377.

(82) Matsusaki, M.; Case, C. P.; Akashi, M. Three-Dimensional Cell Culture Technique and Pathophysiology. *Adv. Drug Deliv. Rev.* **2014**, *74*, 95–103.

(83) Longati, P.; Jia, X.; Eimer, J.; Wagman, A.; Witt, M.-R.; Rehnmark, S.; Verbeke, C.; Toftgård, R.; Löhr, M.; Heuchel, R. L. 3D Pancreatic Carcinoma Spheroids Induce a Matrix-Rich, Chemoresistant Phenotype Offering a Better Model for Drug Testing. *BMC Cancer* **2013**, *13*, 95.

(84) Hirschhaeuser, F.; Menne, H.; Dittfeld, C.; West, J.; Mueller-Klieser, W.; Kunz-Schughart, L. a. Multicellular Tumor Spheroids: An Underestimated Tool Is Catching up Again. *J. Biotechnol.* **2010**, *148*, 3–

15.

(85) Weaver, V. M.; Lelièvre, S.; Lakins, J. N.; Chrenek, M. a; Jones, J. C. R.; Giancotti, F.; Werb, Z.; Bissell, M. J. Beta4 Integrin-Dependent Formation of Polarized Three-Dimensional Architecture Confers Resistance To Apoptosis in Normal and Malignant Mammary Epithelium. *Cancer cell*, 2002, *2*, 205–216.

(86) Li, Q.; Chow, A. B.; Mattingly, R. R. Three-Dimensional Overlay Culture Models of Human Breast Cancer Reveal a Critical Sensitivity to Mitogen-Activated Protein Kinase Kinase Inhibitors. *The Journal of pharmacology and experimental therapeutics*, 2010, *332*, 821–828.

(87) Thurber, G. M.; Wittrup, K. D. Quantitative Spatiotemporal Analysis of Antibody Fragment Diffusion and Endocytic Consumption in Tumor Spheroids. *Cancer research*, 2008, *68*, 3334–3341.

(88) Gao, Y.; Majumdar, D.; Jovanovic, B.; Shaifer, C.; Lin, P. C.; Zijlstra, A.; Webb, D. J.; Li, D. A Versatile Valve-Enabled Microfluidic Cell Co-Culture Platform and Demonstration of Its Applications to Neurobiology and Cancer Biology. *Biomedical microdevices*, 2011, *13*, 539–548.

(89) Ivascu, A.; Kubbies, M. Diversity of Cell-Mediated Adhesions in Breast Cancer Spheroids. *Int. J. Oncol.* **2007**, *31*, 1403–1413.

(90) Bissell, M. J.; Rizki, A.; Mian, I. S. Tissue Architecture: The Ultimate Regulator of Breast Epithelial Function. *Curr. Opin. Cell Biol.* **2003**, *15*, 753–762.

(91) Pickl, M.; Ries, C. H. Comparison of 3D and 2D Tumor Models Reveals

Enhanced HER2 Activation in 3D Associated with an Increased Response to Trastuzumab. *Oncogene* **2009**, *28*, 461–468.

(92) Shaw, K. R. M.; Wrobel, C. N.; Brugge, J. S. Use of Three-Dimensional Basement Membrane Cultures to Model Oncogene-Induced Changes in Mammary Epithelial Morphogenesis. *J. Mammary Gland Biol. Neoplasia* **2004**, *9*, 297–310.

(93) Lee, G. Y.; Kenny, P. A.; Lee, E. H.; Bissell, M. J. Three-Dimensional Culture Models of Normal and Malignant Breast Epithelial Cells. *Nat. Methods* **2007**, *4*, 359–365.

(94) Meng, W.; Kallinteri, P.; Walker, D. a; Parker, T. L.; Garnett, M. C. Evaluation of Poly (Glycerol-Adipate) Nanoparticle Uptake in an in Vitro 3-D Brain Tumor Co-Culture Model. *Exp. Biol. Med. (Maywood).* **2007**, *232*, 1100–1108.

(95) Tung, Y.-C.; Hsiao, A. Y.; Allen, S. G.; Torisawa, Y.; Ho, M.; Takayama, S. High-Throughput 3D Spheroid Culture and Drug Testing Using a 384 Hanging Drop Array. *Analyst* **2011**, *136*, 473–478.

(96) Mouw, J. K.; Ou, G.; Weaver, V. M. I E r Extracellular Matrix Assembly : A Multiscale Deconstruction. *Nat. Publ. Gr.* **2014**, *15*, 771–785.

(97) Meng, W.; Garnett, M. C.; Walker, D. A.; Parker, T. L. Penetration and Intracellular Uptake of Poly(Glycerol-Adipate) Nanoparticles into Three-Dimensional Brain Tumour Cell Culture Models. *Exp. Biol. Med. (Maywood).* **2015**, 1535370215610441.

(98) Hovinga, K. E.; Shimizu, F.; Wang, R.; Panagiotakos, G.; Van Der Heijden, M.; Moayedpardazi, H.; Correia, A. S.; Soulet, D.; Major, T.; Menon, J.; *et al.* Inhibition of Notch Signaling in Glioblastoma Targets Cancer Stem Cells via an Endothelial Cell Intermediate. *Stem Cells* **2010**, *28*, 1019–1029.

(99) Mazzoleni, G.; Di Lorenzo, D.; Steimberg, N. Modelling Tissues in 3D: The next Future of Pharmaco-Toxicology and Food Research? *Genes Nutr.* **2009**, *4*, 13–22.

(100) Albanese, A.; Lam, A. K.; Sykes, E. A.; Rocheleau, J. V.; Chan, W. C. W. Tumour-on-a-Chip Provides an Optical Window into Nanoparticle Tissue Transport. *Nat. Commun.* **2013**, *4*, 2718.

(101) Kwapiszewska, K.; Michalczuk, A.; Rybka, M.; Kwapiszewski, R.; Brzózka, Z. A Microfluidic-Based Platform for Tumour Spheroid Culture, Monitoring and Drug Screening. *Lab Chip* **2014**, *14*, 2096–2104.

(102) Alessandri, K.; Sarangi, B. R.; Gurchenkov, V. V.; Sinha, B.; Kießling, T. R.; Fetler, L.; Rico, F.; Scheuring, S.; Lamaze, C.; Simon, A.; *et al.* Cellular Capsules as a Tool for Multicellular Spheroid Production and for Investigating the Mechanics of Tumor Progression in Vitro. *Proc. Natl. Acad. Sci. U. S. A.* **2013**, *110*, 14843–14848.

(103) Nath, S.; Devi, G. R. Three-Dimensional Culture Systems in Cancer Research: Focus on Tumor Spheroid Model. *Pharmacol. Ther.* **2016**, *163*, 94–108.

(104) Nyga, A.; Loizidou, M.; Emberton, M.; Cheema, U. A Novel Tissue Engineered Three-Dimensional in Vitro Colorectal Cancer Model. *Acta Biomater.* **2013**, *9*, 7917–7926.

(105) Ricketts, K. P. M.; Cheema, U.; Nyga, A.; Castoldi, A.; Guazzoni, C.; Magdeldin, T.; Emberton, M.; Gibson, A. P.; Royle, G. J.; Loizidou, M. A 3D In Vitro Cancer Model as a Platform for Nanoparticle Uptake and Imaging Investigations. *Small* **2014**, *10*, 3954–3961.

(106) Kunz-Schughart, L. A.; Kreutz, M.; Knuechel, R. Multicellular Spheroids: A Three-Dimensional in Vitro Culture System to Study Tumour Biology. *Int. J. Exp. Pathol.* **1998**, *79*, 1–23.

(107) Mueller-Klieser, W. Three-Dimensional Cell Cultures: From Molecular Mechanisms to Clinical Applications. *Am. J. Physiol.* **1997**, *273*, C1109-23.

(108) Ivanov, D. P.; Parker, T. L.; Walker, D. a.; Alexander, C.; Ashford, M. B.; Gellert, P. R.; Garnett, M. C. Multiplexing Spheroid Volume, Resazurin and Acid Phosphatase Viability Assays for High-Throughput Screening of Tumour Spheroids and Stem Cell Neurospheres. *PLoS One* **2014**, *9*, 1–14.

(109) Weiswald, L.; Bellet, D.; Dangles-marie, V. Spherical Cancer Models in Tumor. *Neo* **2015**, *17*, 1–15.

(110) Ivanov, D. P.; Parker, T. L.; Walker, D. a; Alexander, C.; Ashford, M. B.; Gellert, P. R.; Garnett, M. C. In Vitro Co-Culture Model of Medulloblastoma and Human Neural Stem Cells for Drug Delivery

Assessment. *J. Biotechnol.* **2015**, 1–11.

(111) Mehta, G.; Hsiao, A. Y.; Ingram, M.; Luker, G. D.; Takayama, S. Opportunities and Challenges for Use of Tumor Spheroids as Models to Test Drug Delivery and Efficacy. *J. Control. Release* **2012**, *164*, 192–204.

(112) Ivanov, D. P. Assessment of Drug-Loaded Nanoparticles in a 3D in Vitro Brain Tumour Model, Nottingham University, 2014.

(113) Ma, H. L.; Jiang, Q.; Han, S.; Wu, Y.; Tomshine, J. C.; Wang, D.; Gan, Y.; Zou, G.; Liang, X. J. Multicellular Tumor Spheroids as an in Vivo-like Tumor Model for Three-Dimensional Imaging of Chemotherapeutic and Nano Material Cellular Penetration. *Mol. Imaging* **2012**, *11*, 487–498.

(114) Deckert, E. Immunohistochemical Mapping of Hypoxia in Ischemic Mouse Hindlimb Skeletal Muscle. *Microciruculation Tissue Repair Lab* **2010**.

(115) dos Santos, T.; Varela, J.; Lynch, I.; Salvati, A.; Dawson, K. a. Effects of Transport Inhibitors on the Cellular Uptake of Carboxylated Polystyrene Nanoparticles in Different Cell Lines. *PLoS One* **2011**, *6*, e24438.

(116) Fessi, H.; Puisieux, F.; Devissaguet, J. P.; Ammoury, N.; Benita, S. Nanocapsule Formation by Interfacial Polymer Deposition Following Solvent Displacement. *Int. J. Pharm.* **1989**, *55*, R1–R4.

(117) Meng, W.; Parker, T. L.; Kallinteri, P.; Walker, D. A.; Higgins, S.;

Hutcheon, G. A.; Garnett, M. C. Uptake and Metabolism of Novel Biodegradable Poly (Glycerol-Adipate) Nanoparticles in DAOY Monolayer. *J. Control. Release* **2006**, *116*, 314–321.

(118) Ren, S.; Li, C.; Dai, Y.; Li, N.; Wang, X.; Tian, F.; Zhou, S.; Qiu, Z.; Lu, Y.; Zhao, D.; *et al.* Comparison of Pharmacokinetics, Tissue Distribution and Pharmacodynamics of Liposomal and Free Doxorubicin in Tumour-Bearing Mice Following Intratumoral Injection. *J. Pharm. Pharmacol.* **2014**, *66*, 1231–1239.

(119) Paddock, S. W. Principles and Practices of Laser Scanning Confocal Microscopy. *Mol. Biotechnol.* **2000**, *16*, 127–150.

(120) Paddock, S. W. Confocal Laser Scanning Microscopy. *BioTechniques*, 1999.

(121) Laser Scanning Confocal Microscopy 127 MOLECULAR BIOTECHNOLOGY. **2000**.

(122) Cristina, F.; Vieira, L.; Badra Bentley, M. V. L. Confocal Laser Scanning Microscopy as a Tool for the Investigation of Skin Drug Delivery Systems and Diagnosis of Skin Disorders. In *Confocal Laser Microscopy - Principles and Applications in Medicine, Biology, and the Food Sciences*; InTech, 2013.

(123) Brown, M.; Wittwer, C. Flow Cytometry: Principles and Clinical Applications in Hematology. *Clin. Chem.* **2000**, *46*, 1221–1229.

(124) Ormerod, M. G. Flow Cytometry - A Basic Introduction http://flowbook.denovosoftware.com/ (accessed Aug 30, 2017).

(125) Todaro, M.; Alea, M. P.; Di Stefano, A. B.; Cammareri, P.; Vermeulen, L.; Iovino, F.; Tripodo, C.; Russo, A.; Gulotta, G.; Medema, J. P.; *et al.* Colon Cancer Stem Cells Dictate Tumor Growth and Resist Cell Death by Production of Interleukin-4. *Cell Stem Cell* **2007**, *1*, 389–402.

(126) Kondo, J.; Endo, H.; Okuyama, H.; Ishikawa, O.; Iishi, H.; Tsujii, M.; Ohue, M.; Inoue, M. Retaining Cell-Cell Contact Enables Preparation and Culture of Spheroids Composed of Pure Primary Cancer Cells from Colorectal Cancer. *Proc. Natl. Acad. Sci. U. S. A.* **2011**, *108*, 6235–6240.

(127) Mueller-Klieser, W. Tumor Biology and Experimental Therapeutics. *Crit. Rev. Oncol. Hematol.* **2000**, *36*, 123–139.

(128) Trédan, O.; Galmarini, C. M.; Patel, K.; Tannock, I. F. Drug Resistance and the Solid Tumor Microenvironment. *J. Natl. Cancer Inst.* **2007**, *99*, 1441–1454.

(129) Saggar, J. K.; Yu, M.; Tan, Q.; Tannock, I. F. The Tumor Microenvironment and Strategies to Improve Drug Distribution. *Front. Oncol.* **2013**, *3*.

(130) McKee, T. D.; Grandi, P.; Mok, W.; Alexandrakis, G.; Insin, N.; Zimmer, J. P.; Bawendi, M. G.; Boucher, Y.; Breakefield, X. O.; Jain, R. K. Degradation of Fibrillar Collagen in a Human Melanoma Xenograft Improves the Efficacy of an Oncolytic Herpes Simplex Virus Vector. *Cancer Res.* **2006**, *66*, 2509–2513.

(131) Stylianopoulos, T.; Diop-Frimpong, B.; Munn, L. L.; Jain, R. K.

Diffusion Anisotropy in Collagen Gels and Tumors: The Effect of Fiber Network Orientation. *Biophys. J.* **2010**, *99*, 3119–3128.

(132) Eikenes, L.; Bruland, Ø. S.; Brekken, C.; Xenografts, O. Collagenase Increases the Transcapillary Pressure Gradient and Improves the Uptake and Distribution of Monoclonal Antibodies in Human Osteosarcoma Xenografts Collagenase Increases the Transcapillary Pressure Gradient and Improves the Uptake and Distributi. **2004**, 4768–4773.

(133) Kunz-Schughart, L. a; Freyer, J. P.; Hofstaedter, F.; Ebner, R. The Use of 3-D Cultures for High-Throughput Screening: The Multicellular Spheroid Model. *J. Biomol. Screen.* **2004**, *9*, 273–285.

(134) Stylianopoulos, T.; Poh, M.-Z.; Insin, N.; Bawendi, M. G.; Fukumura, D.; Munn, L. L.; Jain, R. K. Diffusion of Particles in the Extracellular Matrix: The Effect of Repulsive Electrostatic Interactions. *Biophys. J.* **2010**, *99*, 1342–1349.

(135) Mok, W.; Boucher, Y.; Jain, R. K. Matrix Metalloproteinases-1 and -8 Improve the Distribution and Efficacy of an Oncolytic Virus. *Cancer Res.* **2007**, *67*, 10664–10668.

(136) Lieleg, O.; Baumgärtel, R. M.; Bausch, A. R. Selective Filtering of Particles by the Extracellular Matrix: An Electrostatic Bandpass. *Biophys. J.* **2009**, *97*, 1569–1577.

(137) Tannock, I. F.; Lee, C. M.; Tunggal, J. K.; Cowan, D. S. M.; Egorin, M. J. Limited Penetration of Anticancer Drugs through Tumor Tissue : A Potential Cause of Resistance of Solid Tumors to Chemotherapy

Limited Penetration of Anticancer Drugs through Tumor Tissue : A Potential Cause of Resistance of Solid Tumors to Chemotherapy 1. *Clin. Cancer Res.* **2002**, *8*, 878–884.

(138) Grantab, R. H.; Tannock, I. F. Penetration of Anticancer Drugs through Tumour Tissue as a Function of Cellular Packing Density and Interstitial Fluid Pressure and Its Modification by Bortezomib. *BMC Cancer* **2012**, *12*, 214.

(139) Trotter, M. J.; Olive, P. L.; Chaplin, D. J. Effect of Vascular Marker Hoechst 33342 on Tumour Perfusion and Cardiovascular Function in the Mouse. *Br. J. Cancer* **1990**, *62*, 903–908.

(140) Smith ', K. A.; Hill ', S. A.; Begg2, A. C.; Denekamp1, J. Validation of the Fluorescent Dye Hoechst 33342 as a Vascular Space Marker in Tumours. *Br. J. Cancer* **1988**, *57*, 247–253.

(141) Walker-Samuel, S.; Boult, J. K. R.; McPhail, L. D.; Box, G.; Eccles, S. A.; Robinson, S. P. Non-Invasive in Vivo Imaging of Vessel Calibre in Orthotopic Prostate Tumour Xenografts. *Int. J. Cancer* **2012**, *130*, 1284–1293.

(142) Ralphe E.Durand. Use of Hoechst 33342 for Cell Selection from Muticell Systems. *J. Histochem. Cytochem.* **1982**, *30*, 117–122.

(143) Nugent, L. J.; Jain, R. K. Extravascular Diffusion in Normal and Neoplastic Tissues. *Cancer Res.* **1984**, *44*, 238–244.

(144) Huxham, L. A.; Kyle, A. H.; Baker, J. H. E.; Nykilchuk, L. K.; Minchinton, A. I. Microregional Effects of Gemcitabine in HCT-116

Xenografts. *CANCER Res.* **2004**, *64*, 6537–6541.

(145) Wijffels, K. I. E. M.; Kaanders, J. H. A. M.; Rijken, P. F. J. W.; Bussink, J.; van den Hoogen, F. J. A.; Marres, H. A. M.; de Wilde, P. C. M.; Raleigh, J. A.; van der Kogel, A. J. Vascular Architecture and Hypoxic Profiles in Human Head and Neck Squamous Cell Carcinomas. *Br. J. Cancer* **2000**, *83*, 674–683.

(146) Zhao, Y.; Alakhova, D. Y.; Kim, J. O.; Bronich, T. K.; Kabanov, A. V. A Simple Way to Enhance Doxil® Therapy: Drug Release from Liposomes at the Tumor Site by Amphiphilic Block Copolymer. *J. Control. Release* **2013**, *168*, 61–69.

(147) Bao, A.; Phillips, W. T.; Goins, B.; Zheng, X.; Sabour, S.; Natarajan, M.; Woolley, F. R.; Zavaleta, C.; Otto, R. A. Potential Use of Drug Carried-Liposomes for Cancer Therapy via Direct Intratumoral Injection. *Int. J. Pharm.* **2006**, *316*, 162–169.

(148) Charrois, G. J. R.; Allen, T. M. Drug Release Rate Influences the Pharmacokinetics, Biodistribution, Therapeutic Activity, and Toxicity of Pegylated Liposomal Doxorubicin Formulations in Murine Breast Cancer. *Biochim. Biophys. Acta 1663* **2004**, *1663*, 167–177.

(149) Jang, S. H.; Guillaume Wientjes, M.; L-S Au, J. Determinants of Paclitaxel Uptake, Accumulation and Retention in Solid Tumors. *Invest. New Drugs* **2001**, *19*, 113–123.

(150) Patel, K. J.; Tannock, I. F. The Influence of P-Glycoprotein Expression and Its Inhibitors on the Distribution of Doxorubicin in Breast Tumors.

(151) Lee, C.; Tannock, I. Inhibition of Endosomal Sequestration of Basic Anticancer Drugs: Influence on Cytotoxicity and Tissue Penetration. *Br. J. Cancer* **2006**, *94*, 863–869.

(152) Zucker, R. M.; Massaro, E. J.; Sanders, K. M.; Degn, L. L.; Boyes, W. K. Detection of TiO2 Nanoparticles in Cells by Flow Cytometry. *Cytom. Part A* **2010**, *77A*, 677–685.

(153) Sims, L. B.; Curtis, L. T.; Frieboes, H. B.; Steinbach-Rankins, J. M. Enhanced Uptake and Transport of PLGA-Modified Nanoparticles in Cervical Cancer. *J. Nanobiotechnology* **2016**, *14*, 33.

(154) Heldin, C.-H.; Rubin, K.; Pietras, K.; Ostman, A. High Interstitial Fluid Pressure - an Obstacle in Cancer Therapy. *Nat. Rev. Cancer* **2004**, *4*, 806–813.

(155) Cheng, Y.; Meyers, J. D.; Broome, A.-M.; Kenney, M. E.; Basilion, J. P.; Burda, C. Deep Penetration of a PDT Drug into Tumors by Noncovalent Drug-Gold Nanoparticle Conjugates. *J. Am. Chem. Soc.* **2011**, *133*, 2583–2591.

(156) Loos, C.; Syrovets, T.; Musyanovych, A.; Mailänder, V.; Landfester, K.; Nienhaus, G. U.; Simmet, T. Functionalized Polystyrene Nanoparticles as a Platform for Studying Bio-Nano Interactions. *Beilstein J. Nanotechnol.* **2014**, *5*, 2403–2412.

(157) Bannunah, A. M.; Vllasaliu, D.; Lord, J.; Stolnik, S. Mechanisms of Nanoparticle Internalization and Transport across an Intestinal Epithelial Cell Model: Effect of Size and Surface Charge. *Mol. Pharm.* **2014**, *11*,

4363–4373.

(158) Lunov, O.; Syrovets, T.; Loos, C.; Beil, J.; Delacher, M.; Tron, K.; Nienhaus, G. U.; Musyanovych, A.; Mailänder, V.; Landfester, K.; *et al.* Differential Uptake of Functionalized Polystyrene Nanoparticles by Human Macrophages and a Monocytic Cell Line. *ACS Nano* **2011**, *5*, 1657–1669.

(159) Bugno, J.; Hsu, H.-J.; Pearson, R. M.; Noh, H.; Hong, S. Size and Surface Charge of Engineered Poly(Amidoamine) Dendrimers Modulate Tumor Accumulation and Penetration: A Model Study Using Multicellular Tumor Spheroids. *Mol. Pharm.* **2016**.

(160) Huang, K.; Ma, H.; Liu, J.; Huo, S.; Kumar, A.; Wei, T.; Zhang, X.; Jin, S.; Gan, Y.; Wang, P. C.; *et al.* Size-Dependent Localization and Penetration of Ultrasmall Gold Nanoparticles in Cancer Cells, Multicellular Spheroids, and Tumors in Vivo. *ACS Nano* **2012**, *6*, 4483–4493.

(161) Juweid, M.; Neumann, R.; Paik, C.; Perez-Bacete, M. J.; Sato, J.; Van Osdol, W.; Weinstein1, J. N. Micropharmacology of Monoclonal Antibodies in Solid Tumors: Direct Experimental Evidence for a Binding Site Barrier. *CANCER Res.* **1992**, *52*, 5144–5153.

(162) Lee, H.; Fonge, H.; Hoang, B.; Reilly, R. M.; Allen, C. Articles The Effects of Particle Size and Molecular Targeting on the Intratumoral and Subcellular Distribution of Polymeric Nanoparticles. **2010**, *7*, 1195–1208.

(163) Goodman, T. T.; Chen, J.; Matveev, K.; Pun, S. H. Spatio-Temporal Modeling of Nanoparticle Delivery to Multicellular Tumor Spheroids. *Biotechnol. Bioeng.* **2008**, *101*, 388–399.

(164) Taresco, V.; Suksiriworapong, J.; Creasey, R.; Burley, J. C.; Mantovani, G.; Alexander, C.; Treacher, K.; Booth, J.; Garnett, M. C. Properties of Acyl Modified Poly(Glycerol-Adipate) Comb-like Polymers and Their Self-Assembly into Nanoparticles. *J. Polym. Sci. Part A Polym. Chem.* **2016**, *54*, 3267–3278.

(165) Weiss, V. M.; Naolou, T.; Hause, G.; Kuntsche, J.; Kressler, J.; Mäder, K. Poly(Glycerol Adipate)-Fatty Acid Esters as Versatile Nanocarriers: From Nanocubes over Ellipsoids to Nanospheres. *J. Control. Release* **2012**, *158*, 156–164.

(166) Kallinteri, P.; Higgins, S.; Hutcheon, G. A.; St Pourç ain, C. B.; Garnett, M. C. Novel Functionalized Biodegradable Polymers for Nanoparticle Drug Delivery Systems. *Biomacromolecules* **2005**, *6*, 1885–1894.

(167) Yang, Z.; Zhang, X.; Luo, X.; Jiang, Q.; Liu, J.; Jiang, Z. Enzymatic Synthesis of Poly(Butylene-Co-Sebacate-Co-Glycolate) Copolyesters and Evaluation of the Copolymer Nanoparticles as Biodegradable Carriers for Doxorubicin Delivery. *ACS Macromol.* **2013**, *46*, 1743−1753.

(168) Mackenzie, R.; Booth, J.; Alexander, C.; Garnett, M. C.; Laughton, C. A. Multiscale Modeling of Drug−Polymer Nanoparticle Assembly Identifies Parameters Influencing Drug Encapsulation Efficiency. *J.*

*Chem. Theory Comput.* **2015**, *11*, 2705–2713.

(169) Pluen, A.; Netti, P. A.; Jain, R. K.; Berk, D. A. Diffusion of Macromolecules in Agarose Gels: Comparison of Linear and Globular Configurations. *Biophys. J.* **1999**, *77*, 542–552.

(170) Nugentand, L. J.; Jain2, R. Extravascular Diffusion in Normal and Neoplastic Tissues1. *CANCER Res.* **1984**, *44*, 238–244.

(171) Suk, J. S.; Xu, Q.; Kim, N.; Hanes, J.; Ensign, L. M. PEGylation as a Strategy for Improving Nanoparticle-Based Drug and Gene Delivery ☆. **2016**.

(172) Pirollo, K. F.; Chang, E. H. Does a Targeting Ligand Influence Nanoparticle Tumor Localization or Uptake? *Trends Biotechnol.* **2008**, *26*, 552–558.

(173) Mun, E. A.; Hannell, C.; Rogers, S. E.; Hole, P.; Williams, A. C.; Khutoryanskiy, V. V. On the Role of Specific Interactions in the Diffusion of Nanoparticles in Aqueous Polymer Solutions. *Langmuir* **2014**, *30*, 308–317.

(174) Nance, E. A.; Woodworth, G. F.; Sailor, K. A.; Shih, T.-Y.; Xu, Q.; Swaminathan, G.; Xiang, D.; Eberhart, C.; Hanes, J. A Dense Poly(Ethylene Glycol) Coating Improves Penetration of Large Polymeric Nanoparticles Within Brain Tissue. *Sci. Transl. Med.* **2012**, *4*.

(175) Minchinton, A. I.; Tannock, I. F. Interstitial Fluid Pressure Extracellular Matrix Clonogenic Cell Drug Penetration in Solid Tumours. *TUMOUR*

*Microenviron. Drug* **2006**, *6*, 583–592.

(176) He, C.; Hu, Y.; Yin, L.; Tang, C.; Yin, C. Effects of Particle Size and Surface Charge on Cellular Uptake and Biodistribution of Polymeric Nanoparticles. *Biomaterials* **2010**, *31*, 3657–3666.

(177) Yameen, B.; Choi, W. Il; Vilos, C.; Swami, A.; Shi, J.; Farokhzad, O. C. Insight into Nanoparticle Cellular Uptake and Intracellular Targeting. *J. Control. Release* **2014**.

(178) Oh, N.; Park, J.-H. Endocytosis and Exocytosis of Nanoparticles in Mammalian Cells. *Int. J. Nanomedicine* **2014**, *9 Suppl 1*, 51–63.

(179) Sriraman, S. K.; Aryasomayajula, B.; Torchilin, V. P. Barriers to Drug Delivery in Solid Tumors. *Tissue Barriers* **2014**, *2*, e29528.

(180) Ekkapongpisit, M.; Giovia, A.; Follo, C.; Caputo, G.; Isidoro, C. Biocompatibility, Endocytosis, and Intracellular Trafficking of Mesoporous Silica and Polystyrene Nanoparticles in Ovarian Cancer Cells: Effects of Size and Surface Charge Groups. *Int. J. Nanomedicine* **2012**, *7*, 4147–4158.

(181) Shenoy, V.; Rosenblatt, J. Diffusion of Macromolecules in Collagen and Hyaluronic Acid, Rigid-Rod-Flexible Polymer, Composite Matrices. *Macromolecules* **1995**, *28*, 8751–8758.

(182) Christiansen, R.; Dische, J. A.; Doty, Z.; Edsall, P.; Edsall, J. T.; Neurath, J. T.; Bailey, H.; New, K.; Evans, C. L. G. OSMOTIC PRESSURE OF ALBUMIN AND HYALURONIC ACID 253. *J. biol. Chem. Adv. Protein Chem. part B Makromol. Chem. Biochim. biophy8.*

*Acta Biochim. biophy8. Acta Arch. Biochem. Biophy8* **1960**, *8912855*, 549–717.

(183) Lin, W.; Garnett, M. C.; Schacht, E.; Davis, S. S.; Illum, L. Preparation and in Vitro Characterization of HSA-MPEG Nanoparticles. *Int. J. Pharm.* **1999**, *189*, 161–170.

(184) Hatakeyama, H.; Akita, H.; Kogure, K.; Oishi, M.; Nagasaki, Y.; Kihira, Y.; Ueno, M.; Kobayashi, H.; Kikuchi, H.; Harashima, H. Development of a Novel Systemic Gene Delivery System for Cancer Therapy with a Tumor-Specific Cleavable PEG-Lipid. *Gene Ther.* **2007**, *14*, 68–77.

(185) Eikenes, L.; Tufto, I.; Schnell, E. a.; Bjørkøy, A.; Davies, C. D. L. Effect of Collagenase and Hyaluronidase on Free and Anomalous Diffusion in Multicellular Spheroids and Xenografts. *Anticancer Res.* **2010**, *30*, 359–368.

(186) Cun, X.; Ruan, S.; Chen, J.; Zhang, L.; Li, J.; He, Q.; Gao, H. A Dual Strategy to Improve the Penetration and Treatment of Breast Cancer by Combining Shrinking Nanoparticles with Collagen Depletion by Losartan. *Acta Biomater.* **2016**, *31*, 186–196.

(187) Xu, X.; Farach-Carson, M. C.; Jia, X. Three-Dimensional in Vitro Tumor Models for Cancer Research and Drug Evaluation. *Biotechnol. Adv.* **2014**, *32*, 1256–1268.

# APENDIX I

Size distribution graphs of PGA NPS in DI water.

PGA

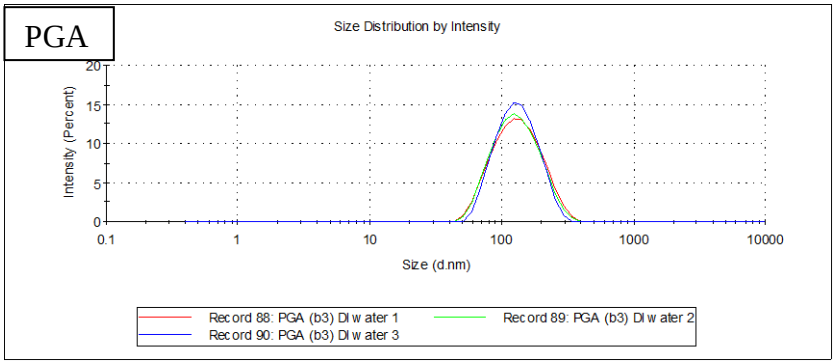


PGA-PEG

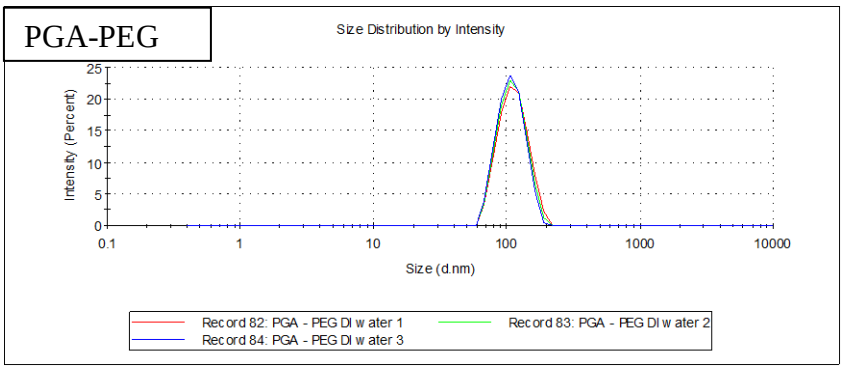


PGA-C18

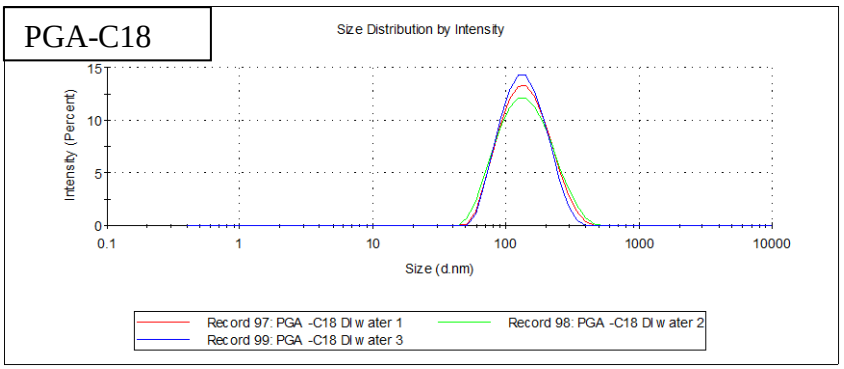


PGA-C18-PEG

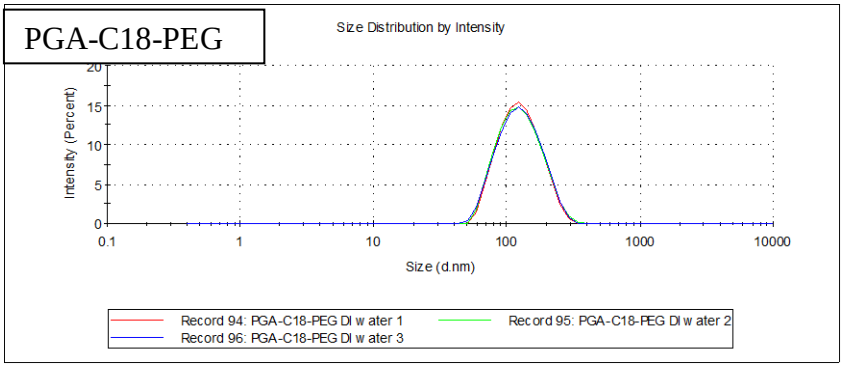

Size distribution graphs of PGA NPS in RPMI 1640 with FBS.

PGA

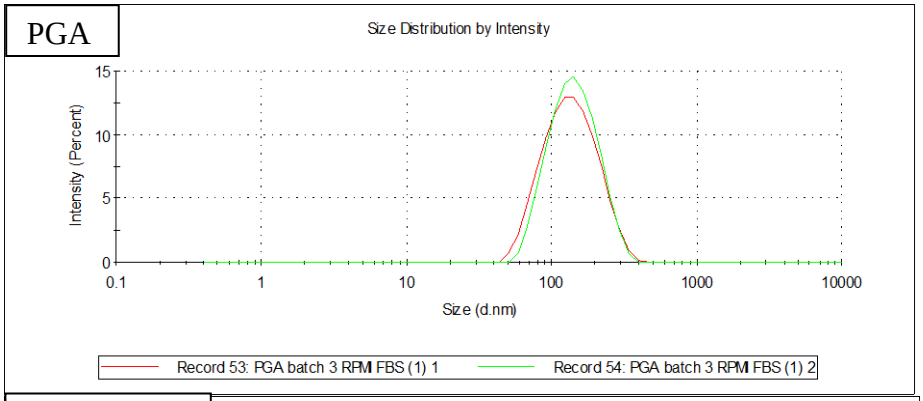


PGA-PEG

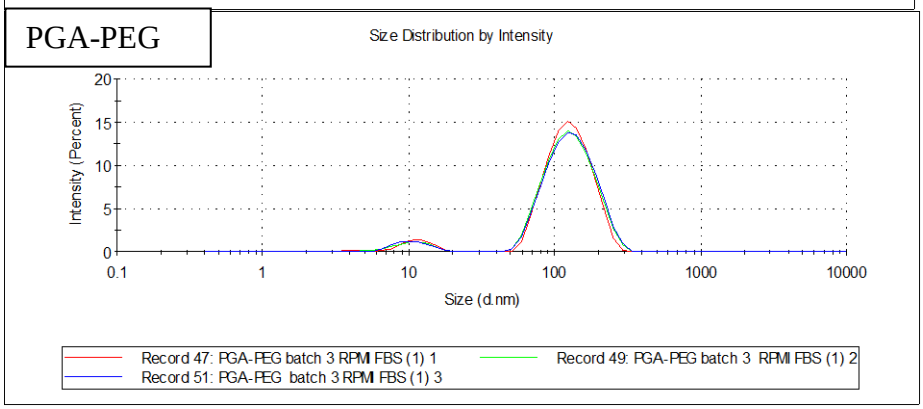


PGA-C18

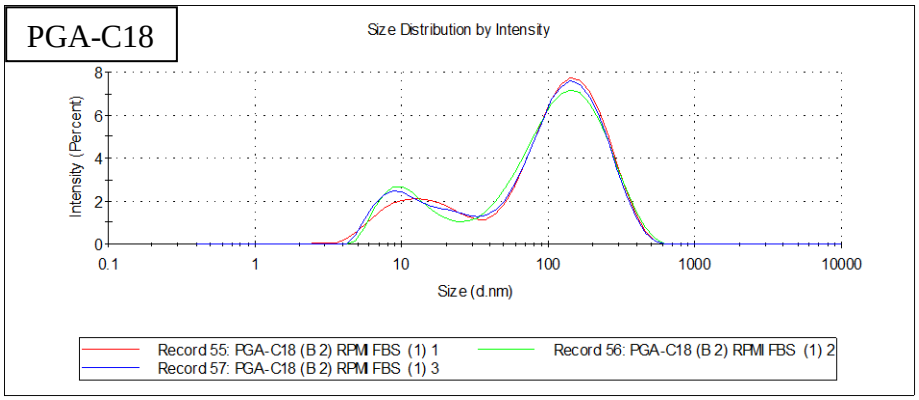


PGA-C18-PEG